Universitat Politècnica de Catalunya

Electrical Engineering Department

PhD Thesis

Power converter optimal control for wind energy conversion systems

Author: **Lluís Trilla Romero**

Advisors: **Oriol Gomis Bellmunt**
Fernando D. Bianchi

Barcelona, September 2013

Catalonia Institute for Energy Research (IREC)
Electrical Engineering Research Area
Jardins de les Dones de Negre 1 2nd floor,
08930 Sant Adrià de Besòs, Barcelona, Spain

Printed in Barcelona by CPET, S.L.
First Print, September 2013

UNIVERSITAT POLITÈCNICA DE CATALUNYA
BARCELONATECH
Escola de Doctorat

Acta de qualificació de tesi doctoral

Curs acadèmic:

Nom i cognoms

Programa de doctorat

Unitat estructural responsable del programa

Resolució del Tribunal

Reunit el Tribunal designat a l'efecte, el doctorand / la doctoranda exposa el tema de la seva tesi doctoral titulada _____ _____.

Acabada la lectura i després de donar resposta a les qüestions formulades pels membres titulars del tribunal, aquest atorga la qualificació:

☐ NO APTE ☐ APROVAT ☐ NOTABLE ☐ EXCEL·LENT

(Nom, cognoms i signatura)	(Nom, cognoms i signatura)	
President/a	Secretari/ària	
(Nom, cognoms i signatura)	(Nom, cognoms i signatura)	(Nom, cognoms i signatura)
Vocal	Vocal	Vocal

_____, _____ d'/de _____ de _____

El resultat de l'escrutini dels vots emesos pels membres titulars del tribunal, efectuat per l'Escola de Doctorat, a instància de la Comissió de Doctorat de la UPC, atorga la MENCIÓ CUM LAUDE:

☐ SÍ ☐ NO

(Nom, cognoms i signatura)	(Nom, cognoms i signatura)
Presidenta de la Comissió de Doctorat	Secretària de la Comissió de Doctorat

Barcelona, _____ d'/de _____ de _____

Abstract

Wind energy has increased its presence in many countries and it is expected to have even a higher weight in the electrical generation share with the implantation of offshore wind farms. In this context, the development of accurate models of Wind Energy Conversion Systems (WECSs) is important for grid operators in order to evaluate their behavior. Grid codes offer a set of rules to validate models with data gathered from field tests. In the first part of this thesis, a WECS model based on a Doubly-Fed Induction Generator (DFIG) is validated according to the German and Spanish grid codes. Nowadays many wind farms use DFIGs, consequently, the field data available was based on this technology. For the offshore wind power industry, a promising technological advance are WECSs that incorporate Permanent Magnet Synchronous Generators (PMSG). For this reason, the second part of this thesis is focused on PMSG-based wind turbines with fully-rated back-to-back converters. This converter can be divided in two sides: the Grid-Side Converter (GSC) that interacts with the network and the Machine-Side Converter (MSC) that controls the generator.

In general, the converter control system relies on traditional PI controllers and, in some cases, it includes decoupling terms that aim to reduce the crossed influence among variables. This controller is easily tuned and implemented since it has a simple structure, however, its response is not ideal since it does not exploit all the degrees of freedom available in the system. It is important to develop reliable controllers that can offer a predictable system response and provide stability and robustness. Specially for areas where the wind power presence is high and wind farms connected to weak

grids.

In this work, a control system for the power converter based on $\mathcal{H}_\infty$ control theory and Linear Parameter-Varying (LPV) controllers is proposed. Optimal control theory provides a framework where more options can be taken in consideration during the controller design stage. In particular, $\mathcal{H}_\infty$ control theory permits the development of multi-variable controllers in order to obtain an optimal response of the system, to provide some robustness and to ensure stability. Using this technique during the controller synthesis process the worst disturbance signals case is contemplated, in this way, the resulting controller robustifies the operation of the system. This controller is proposed for the GSC with special emphasis in developing a low-complexity controller that maintains the benefits of applying the optimal control theory and facilitates its implementation in industrial computers.

For the MSC a different strategy based on LPV control is proposed since the operating point of the generator changes constantly. The LPV-based control system is capable of adapting dynamically the controller to the operating point of the system, in this way, the response defined during the design process is always obtained. Using this technique, the system stability over the entire range of operation is guaranteed and, also, a predictable and uniform response is obtained. The controller is designed to keep a simple structure, as a result, a controller that is not computationally demanding is obtained and a solution that can be used with industrial equipment is provided.

A test bench including a PMSG and a fully-rated back-to-back converter is developed in order to validate experimentally the control strategy designed in this work. The implementation-oriented nature of the proposed controllers facilitates their use with the Digital Signal Processor (DSP) embedded in the control board of the test bench. The experiments performed verify in a realistic environment the theoretical benefits and the simulation results obtained previously. These tests helped also to assess the correct performance of the controllers in a discrete system and their tolerance to noisy signals and measurements.

Resum

L'energia eòlica ha incrementat la seva presència a molts països i s'espera que tingui encara un pes més gran en la generació elèctrica amb la implantació de la tecnologia eòlica marina. En aquest context el desenvolupament de models dels Sistemes de Generació per Turbina de Vent (SGTV) precisos és important pels operadors de xarxa per tal d'avaluar-ne el comportament. Els codis de xarxa ofereixen un seguit de normes per validar models amb dades obtingudes de proves de camp. A la primera part d'aquesta tesi un model de SGTV amb màquina d'inducció doblement alimentada (DFIG) és validat d'acord amb les normatives espanyola i alemanya. Avui dia molts parc eòlics utilitzen DFIG i, en conseqüència, les dades de camp disponibles son per aquesta tecnologia. Per a la indústria eòlica marina un avanç prometedor son els SGTV amb generadors síncrons d'imants permanents (PMSG). Per aquesta raó la segona part d'aquesta tesi es centra en SGTV basats en PMSG amb convertidor *back-to-back* de plena potència. Aquest convertidor es pot dividir en dues parts: el costat de xarxa (GSC) que interactua amb la xarxa elèctrica i el costat de màquina (MSC) que controla el generador.

En general, el sistema de control del convertidor recau en els tradicionals controladors PI i, en ocasions, incorpora desacoblaments per reduir les influencies creuades entre les variables. Aquest controlador pot ser sintonitzat i implementat fàcilment donat que la seva estructura és simple, però, no presenta una resposta idònia donat que no aprofita tots els graus de llibertat disponibles en el sistema. És important desenvolupar controladors fiables que puguin oferir una resposta previsible del sistema i proveir robustesa i estabilitat. En especial per zones on la presència eòlica és gran i per parcs

eòlics connectats a xarxes dèbils.

En aquest treball es proposa un sistema de control pel convertidor basat en teoria de control $\mathcal{H}_\infty$ i en controladors Lineals amb Paràmetres Variants (LPV). La teoria de control òptim proveeix un marc de treball on més opcions es poden tenir en consideració a l'hora de dissenyar el controlador. En concret la teoria de control $\mathcal{H}_\infty$ permet crear controladors multivariables per tal d'obtenir una òptima resposta del sistema, proveir certa robustesa i assegurar l'estabilitat. Amb aquesta tècnica, durant la síntesi del controlador el pitjor cas de senyals de pertorbació és contemplat, d'aquesta manera el controlador resultant robustifica l'operació del sistema. Es proposa aquest control pel GSC posant especial èmfasi en obtenir un control de baixa complexitat que mantingui els beneficis d'aplicar la teoria de control òptim i en faciliti la implementació en computadors industrials.

Pel MSC es proposa una estratègia diferent basada en control LPV donat que el punt d'operació del generador canvia constantment. El sistema de control basat en LPV és capaç d'adaptar-se dinàmicament al punt d'operació del sistema, així s'obté en tot moment la resposta definida durant el procés de disseny. Amb aquesta tècnica l'estabilitat del sistema sobre tot el rang d'operació queda garantida i, a més, s'obté una resposta predictible i uniforme. El controlador està dissenyat per tenir una estructura simple, com a resultat s'obté un control que no és computacionalment exigent i es proveeix una solució que pot ser utilitzada amb equips industrials.

S'utilitza una bancada de proves que inclou el PMSG i el convertidor *back-to-back* per tal d'avaluar experimentalment l'estratègia de control dissenyada al llarg d'aquest treball. L'enfoc orientat a la implementació dels controls proposats facilita el seu ús amb el processador de senyals digitals inclòs a la placa de control de la bancada. Els experiments realitzats verifiquen en un ambient realista els beneficis teòrics i els resultats de simulació obtinguts prèviament. Aquestes proves han ajudat a valorar el funcionament dels controls en un sistema discret i la seva tolerància al soroll de senyals i mesures.

Acknowledgements

This thesis has been supported by the Catalonia Institute for Energy Research (IREC) through the grant 08/09 Wind Energy. I would also thank the support received by CITCEA-UPC and the collaboration of Alstom Wind during the first stage of this research. It is also appreciated the effort done by the advisors along the development of this thesis. And, finally, the collaboration of professor Torbjörn Thiringer during the stage as a visitor researcher in Chalmers University.

Contents

List of Tables

List of Figures

Acronyms

B2B	Back-to-Back
DFIG	Doubly-Fed Induction Generator
DSP	Digital Signal Processor
ESC	Emulation-Side Converter
GSC	Grid-Side Converter
HVDC	High Voltage DC
IGBT	Insulated-Gate Bipolar Transistor
IMC	Internal Model Control
LFRT	Line-Fault Ride-Through
LFT	Linear Fractional Transformation
LPV	Linear Parameter-Varying
LTI	Linear Time-Invariant
MSC	Machine-Side Converter
PI	Proportional-Integral
PLL	Phase-Locked Loop
PMSG	Permanent Magnet Synchronous Generator
PMSM	Permanent Magnet Synchronous Motor
SISO	Single-Input Single-Output
STATCOM	STATic COMpensator
SVPWM	Space-Vector Pulse Width Modulation

VSC	Voltage Source Converter
WECS	Wind Energy Conversion System

1 Introduction

Wind Energy Conversion Systems (WECS) have increased its penetration in the electrical grid of most countries during the last years. Integration of wind power in power systems [4, 5] is becoming a challenge specially in terms of power quality and fault ride-through capability. Detailed models of wind turbines are required, by grid operators, power companies, wind farm developers and also in the research field, for grid integration studies both for analysis of the wind turbine under grid faults and for power system stability studies.

Doubly-Fed Induction Generators (DFIG) are a well-known technology widely used for wind power purposes. Many authors have studied the modeling of DFIG-based wind turbines for different purposes, in [6] the influence of the model simplifications and the parameters are analyzed, the model developed in [7] focuses on the effect of sub-synchronous resonance in the grid. Other authors have studied the model of DFIG in fault conditions [8], in [9] the experimental verification of the model is done and in [10] field data is used for model validation.

On the other hand, Permanent Magnet Synchronous Generators (PMSG) do not require electrical excitation, are more efficient and show a better weight/power ratio, compared to other generator technologies [11]. These facts make the PMSG an interesting option and, consequently, many authors have considered its use for different applications such as gas turbines [12], hydro power [13], diesel generators [14], flywheels [15, 16] and wind power systems [17] among others. Its use is specially interesting for WECS since

their presence is increasing worldwide and it is expected that the installed capacity will keep growing in the next years [18]. Wind turbines equipped with PMSG and full scale power converter seem to be the trend of the industry for offshore wind farm topology, the motivation of this choice is given by the new scale of size (diameter of more than 120 m) and power (more than 5 MW) of the next wind turbines generation [19].

In any case, it is crucial to develop reliable WECS simulation models in order to test their operation, control system and their response in front of unexpected situations. In general, these models are not used to design the controllers, since most of the control design techniques use linear models based on simplifications and assumptions, but are useful to evaluate the controllers performance in a realistic environment. The idea is to check how accurate are the predictions obtained by means of simulation, for this reason the grid codes [20, 1, 3, 21] provide a set of rules to measure the accuracy of the model.

Other important aspect of the development and growth of this type of renewable energy is the use of power electronics devices. Modern wind turbine based energy sources use power converters to enhance their performance and range of operation. In consequence, the presence of power converters in the power grid have increased rapidly in the recent years [22]. Their flexibility for energy flow control makes possible the interconnection of different kind of power sources [23, 24] or energy storage devices and the AC grid [25]. Over this decade, higher voltage levels in the semiconductors have been achieved and costs have been reduced [26]. This evolution has led to a massive implantation of power electronic devices, specially as a solution for renewable energy sources integration in the AC grid [27, 28] and for the development of smart and micro grids [29]. Other interesting applications of power converters are HVDC transmission lines [30], where the interaction between AC and DC lines is managed by the converters, and STATCOM devices, that provide reactive power and facilitate the compliance with the grid codes improving the grid integration of power sources [31]. In this work, the control of Voltage Source Converters (VSCs) will be analyzed, the use of VSC is motivated by the fact that they are widely used for distributed energy resources integration into the power grid.

It is usual to use back-to-back (B2B) converters in WECS applications. This type of converter has two sides, one interacts with the power grid, known as Grid-Side Converter (GSC), and the other with the machine,

known as Machine-Side Converter (MSC). The control system of power converters is becoming a topic of interest since several types of distributed energy resources are being incorporated into the power grid, in this sense many control options have been analyzed [32]. Regarding the GSC, some authors have proposed different types of controllers, traditionally linear controllers were considered, such as PI controllers [33], state feedback controllers [34] and constant switching frequency predictive controllers [35]. In recent investigations, robust control techniques [36, 37] have been studied and the application of $\mathcal{H}_\infty$ control theory to design the control system of power electronics devices [38, 39, 40] has been considered as well.

Optimal controllers based on $\mathcal{H}_\infty$ control theory offer some advantages respect to traditional controllers in power converters applications. Commonly, the control of VSC relies on simple PI structures with decoupling terms. Model simplifications are used in order to compute the PI parameters by using design techniques such as Internal Model Control (IMC) [41]. Although these schemes provide satisfactory responses, they do not fully exploit the control possibilities of multi-variable tools, an improvement in performance and stability of multi-variable controllers is reported in [42]. It is also analyzed via simulation the use of $\mathcal{H}_\infty$ control theory based controllers in [43] showing a better handling of grid disturbances than regular PI controllers.

In the case of the MSC, power electronic devices have an important role because they control the generator and link it to the electrical subsystem. Many of the proposed control strategies are focused on the high-level (speed) control system that computes the reference signals [44, 45, 46] for the low-level (converter) control. Generally, the low-level control system is based on vector control theory where the control actions are the voltages and the currents are the variables to be controlled. Similarly to the GSC case, the control strategies are usually based on PI structures [47, 48, 49] and some of them include decoupling terms [50, 51]. These additional terms help to adapt the controller response to different operating conditions, thus, improving the performance of the system. In variable speed wind turbines, the controller has to deal with wide operating conditions covering from the cut-in speed to the maximum limit, where the pitch control starts to act; within this range, the rotational speed can double its value.

For systems with dynamic responses changing with the operating conditions, gain scheduling techniques have proved to be effective at extending

linear control ideas to non-linear or time varying systems. Notice that the PI controllers with decoupling terms commonly used in PMSG applications as in [50, 51] are basically gain scheduled controllers adapting themselves to different rotational velocities. In particular, Linear Parameter-Varying (LPV) system theory has been proposed to formalise systematic design procedures for gain-scheduled controllers [52, 53]. These techniques have been successfully applied in other generator technologies; in particular, they can be found in the control of doubly-fed induction generators (DFIG) in [54, 55, 56]. In [57, 58], $\mathcal{H}_\infty$ gain-scheduled controllers are proposed for induction motors based on output feedback schemes, leading in both cases to complex control implementations. In [58] the authors conclude that one drawback of the proposed approach is especially for DSP implementation due to the increasing degree of the controller. An alternative using a parameterization of the LPV stabilizing controller is used in [59] to regulate the angular speed. Applications for Permanent Magnet Synchronous Motors (PMSM) are discussed in [60, 61] where the LPV approach is used to develop a robust controller. In [61] and [62] the LPV approach is proposed for PMSM using an output feedback scheme and including first order weighting functions that yield high-order controllers. In most of these applications, the controllers are evaluated via simulation but not experimentally.

Despite the quantity of research done in this field, control systems based on $\mathcal{H}_\infty$ control theory and the LPV approach are, in some sense, considered to be too complicated and demanding for industrial equipment. It is in this context where one of the objectives of this project is to develop controllers using these control design techniques and evaluate their potential benefits and computational cost in a wind power framework.

1.1 Thesis objectives

- In a first place, the development and validation of a WECS electrical subsystem model had to be performed. In this sense, obtaining a reliable simulation model was important to predict the response of the system to different control strategies.

- The design of control systems for both sides of the back-to-back converter using $\mathcal{H}_\infty$ control theory and specially an LPV controller to manage the generator side.

- Develop a test bench in the laboratory and test the proposed con-

trollers using standard DSP processing units.

- Evaluation of the improvements and drawbacks of using optimal controllers for industrial applications.

1.2 Main contribution of this thesis

The control system of the electrical variables in a WECS is, generally, based on Single-Input Single-Output PI controllers. It is the aim of this work to design and test an alternative strategy for the control system using a different approach. A LPV controller is selected to manage the MSC while an optimal controller based on $\mathcal{H}_\infty$ control theory is chosen for the GSC. In many applications, these type of controllers may improve the resultant performance but the increase of complexity that brings with them does not justify its use. The control strategy proposed in this project offers "light" controllers that maintain the positive characteristics of using these techniques, such as stability, robustness or adaptability, while the drawbacks are reduced in terms of computing time or memory occupation. In a first stage, a complete model of a WECS is developed and validated providing confidence about the results obtained via simulation when testing the different controllers. It is also offered a guideline to follow the official grid codes regarding the model validation process. In a second step the proposed $\mathcal{H}_\infty$-based control system is designed and tested in a grid-connected VSC acting as an interface between some sort of power source (in DC) and the AC grid, as many kind of distributed energy resources are. In the last stage the LPV control system of the generator is developed and tested in combination with the controller designed in the previous step for the grid side. A small-scale test bench is implemented in the laboratory in order to test and confirm the results observed via simulation during the previous stages and, also, to evaluate the viability of its use for industrial applications.

1.3 Outline of the thesis

- **Chapter 2** provides an overview of the modeling, control and validation process of a wind energy conversion system
- **Chapter 3** details the equipment used to set up a test bench
- **Chapter 4** describes the model validation process of an operational wind turbine

- In **Chapter 5**, the design, application and test of the grid-side converter control based on $\mathcal{H}_\infty$ control theory is detailed
- In **Chapter 6**, the machine-side converter control using LPV control is developed, tested and compared to standard PI
- **Chapter 7** summarizes the contributions and some conclusions are provided besides the future research lines.

2 Background material

In this chapter, a brief description of the WECS and the validation process is provided. An overview of the control system, in general terms, is also offered.

2.1 Description of a WECS

A WECS captures the kinetic energy contained in the wind and delivers electrical energy. This process is done in two stages which are performed by different subsystems. The first stage is done by the mechanical subsystem that transmits the energy contained in the wind to a rotational mass, then, in the second stage, the electrical subsystem evacuates it in the form of electrical energy. In this work, the focus is on the electrical subsystem of a horizontal axis WECS since this concept of wind turbine is widely used, although other structures are currently available. Also, the scope of this work is on large wind generators and no in micro wind turbines which represent a different challenge.

2.1.1 Mechanical subsystem

In general, the mechanical subsystem is formed by the rotor (that includes the blades, the pitch actuator and the low-speed axis), the gearbox and the high-speed axis. The energy contained in the wind is captured by the blades according to

$$P_w = C_P\left(\lambda, \theta_{pitch}\right) \frac{1}{2} \rho A v_w^3 \tag{2.1}$$

where ρ is the air density, A is the swept area and v_w is the wind speed. The power coefficient C_P, as a function of the wind speed and the turbine speed, can be approximated by the analytic expression [63]

$$C_P\left(\lambda, \theta_{pitch}\right) = c_1 \left(c_2 \frac{1}{\Lambda} - c_3 \theta_{pitch} - c_4 \theta_{pitch}^{c_5} - c_6 \right) e^{-c_7 \frac{1}{\Lambda}} \tag{2.2}$$

where $[c_1 \dots c_9]$ are aerodynamic parameters that are defined by the blade shape, θ_{pitch} is the blade pitch angle and Λ is defined as

$$\frac{1}{\Lambda} = \frac{1}{\lambda + c_8 \theta_{pitch}} - \frac{c_9}{1 + \theta_{pitch}^3}, \qquad \lambda = \frac{\omega_t R}{v_w} \tag{2.3}$$

where λ is called the tip speed ratio, R is the turbine radius and ω_t is the rotational speed of the rotor. An example of C_P curve is shown in Fig. 2.1 and corresponds to the particular case for a pitch angle of 0° of the expression (2.2).

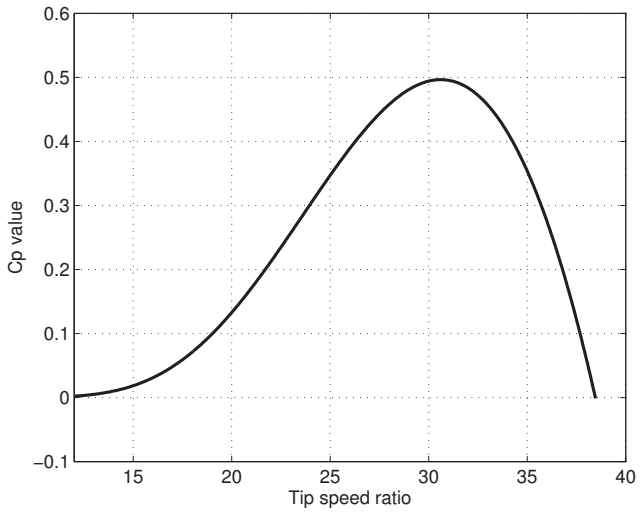

Figure 2.1: Cp curve for a pitch angle of 0°

When λ and θ_{pitch} are at their optimal values, the energy captured is maximized, however, the amount of energy that can be extracted from the wind is limited by the Betz factor. The blade pitch angle can be changed in order to reduce the amount of energy absorbed and avoid to overpass the limits of the system. Using this mechanism, the range of operability can be enhanced yielding a more flexible energy source. A WECS actuates from the cut-in speed to the cut-out speed, as shown in Fig. 2.2. The energy capture is maximized in the variable speed region until the operational limit is reached, then, the curved is flattened by the action of the blade pitch actuator and the system is operating in constant speed.

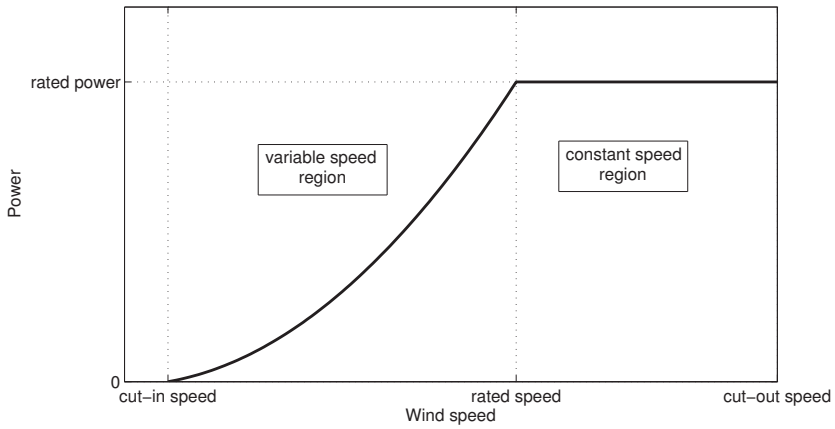

Figure 2.2: Generic power output for a variable speed wind turbine

The rotational speed of the rotor is usually low and a gearbox becomes necessary to adapt the speed for the generator. A conventional generator usually requires higher speed to operate in its optimal way. If the gearbox is considered ideal and a one-mass model is used to describe the drive train (although multi-mass model are used for detailed modeling of the mechanical oscillations) the gear ratio (η) can be applied in the form

$$\omega_g = \eta\omega_t, \qquad \Gamma_t = \eta\Gamma_{load}, \tag{2.4}$$

where Γ_t is the turbine torque, Γ_{load} is the load torque of the generator and ω_g is the rotational speed of the high-speed axis which is connected to the rotor of the generator. A general view of the mechanical system is depicted

in Fig. 2.3

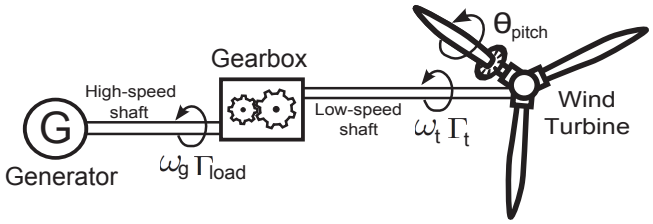

Figure 2.3: Generic mechanical subsystem of horizontal axis wind turbine

2.1.2 Electrical subsystem

In general terms, the electrical subsystem comprises the generator, the power converter, the filters and line inductances and the transformer. In the generator the mechanical energy is transformed into electrical energy. The load torque applied by the high-speed axis is counterbalanced by the electrical torque applied by the generator reaching an equilibrium. In order to enhance its performance, the generator is connected to a power converter that regulates the electromechanical torque and, in the variable speed region, the rotational speed of the rotor. There are many types of generators proposed for wind power applications, among them this section focuses in the Doubly-Fed Induction Generator (DFIG) and the Permanent Magnet Synchronous Generator (PMSG).

Doubly-Fed Induction Generator

The DFIG has its rotor connected to the power converter and the stator connected to the power grid as shown in Fig. 2.4.

A positive characteristic of this type of WECS is that it requires a partially rated power converter (around a 30% of the generator rated power). On the other hand, this configuration is severely affected by disturbances in the AC grid, since the stator is connected to the grid the electrical behavior of the system is very sensitive to grid faults. This configuration is present in many onshore wind farms worldwide, specially for its reduced power converter size. A detailed model of this type of generator can be found in **Chapter 4**. Data from DFIG-based wind turbines has been gathered during the field tests, in consequence, the validation process will be referred to this type of machine.

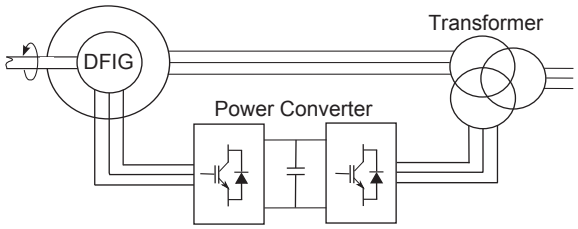

Figure 2.4: Doubly-Fed Induction Generator connection scheme

Permanent Magnet Synchronous Generator

The PMSG has its stator connected to the fully rated power converter, this converter acts as an interface between the generator and the grid as shown in Fig. 2.5. The magnets included in the generator provide a constant magnetic field avoiding the need of independent electrical excitation. This type of generator presents a good power/weight ratio that makes it an interesting option for the new generation of wind turbines for offshore applications. For this reason, the development of the control system detailed in this work is referred to this type of machine. The complete model of the generator can be found in **Chapter 6**.

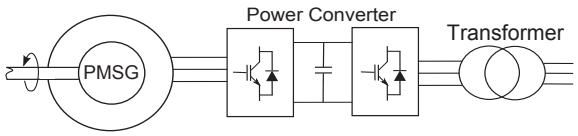

Figure 2.5: Permanent Magnet Synchronous Generator connection scheme

Back-to-back converter

Usually, a back-to-back converter is used for these applications, this topology consists of two AC/DC converters connected through their DC sides. A two-level converter is composed by three branches of high-frequency switches in each AC side, each branch is connected to one phase of the three-phase electrical system. There exist other topologies such as multilevel converters, but, although they represent promising structures, they are out of the scope of this thesis. There are also several types of semiconductors but, among

them, IGBT are the most widely used currently because of their high commutation frequency and ampacity. Between the two AC sides there is located a capacitor bank, this element acts as a DC-link and decouples the electrical frequency from both AC sides. A schematic view of this type of converter is shown in Fig. 2.6.

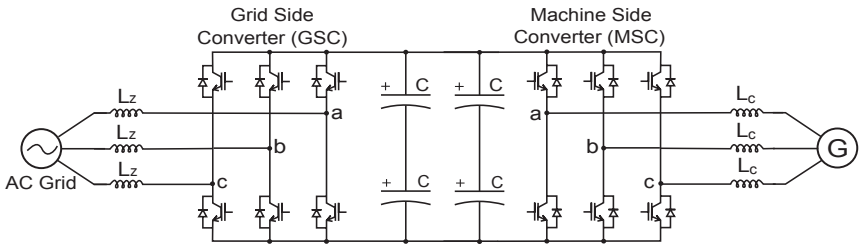

Figure 2.6: Back-to-back converter scheme

For detailed simulations the IGBT bridge and the switching system is modeled [64]. For control design purposes the converter can be described using an average model as in [65] where it is assumed that the high-frequency components derived from the switching actions are totally filtered and also the switching energy losses are neglected.

Filters

In order to reduce the amount of high frequency harmonics derived from the IGBTs switching action there are filters connected at the output terminals of the converter. In general, inductances are used for this purpose although other types of filters (such as LCL) are also used in some applications. The filter based on inductances acts as a low-pass filter and its reactance (X) can be expressed as

$$jX = j\omega L \tag{2.5}$$

where ω is the electrical frequency and L is the inductance. If the non-linearities of the inductor are not considered, this element can be modeled as an RL branch and its impedance (Z) is expressed as

$$Z = R + jX \tag{2.6}$$

where R is the resistance.

2.2 Control system overview

The control system of a generic WECS can be split in three blocks: speed control, machine-side converter control, and grid-side converter control. A block diagram of the generic control strategy is depicted in Fig. 2.7

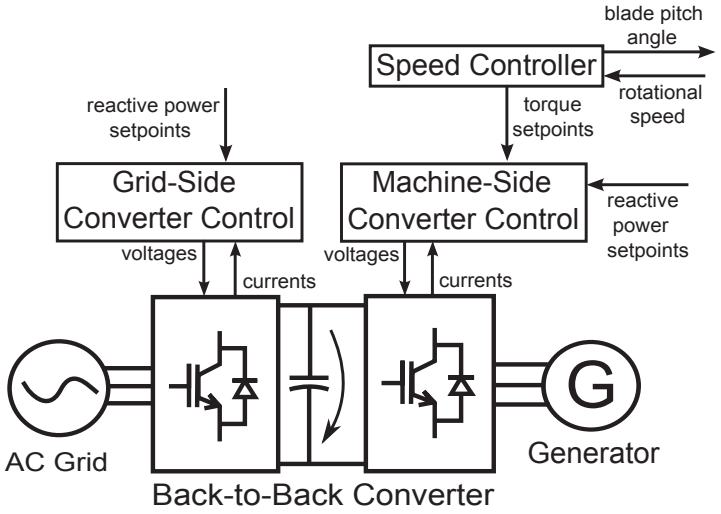

Figure 2.7: Block diagram of the generic control strategy

The speed controller regulates the blade pitch angle and computes the torque setpoints. In general, this controller has two different objectives depending on the region where the WECS is operating. In the variable speed region (see Fig. 2.2) the speed controller computes the torque setpoints with the aim of maximizing the power output, in this region the blade pitch angle is usually constant. The power extracted from the wind is maximized by keeping the C_P coefficient close to its optimal value as shown in Fig. 2.1. In the constant speed region the torque setpoints are constant and the objective of the speed controller is to maintain the wind turbine within its operational limits. This task is done by regulating the blade pitch angle in order to reduce the C_P value and, in consequence, the power captured. In the literature there are many speed control proposals that aim to fulfill different goals such as maximizing energy production or the reduction of the mechanical stress. The study of the speed controller has not been included in this work since it requires specific software to analyze the mechanical subsystem and the aerodynamic effects and, also, access to existing turbines

to run tests. The other two control blocks correspond to each of the AC sides of the back-to-back converter, a detailed description of them can be found in **Chapter 5** for the Grid-Side Converter (GSC) and in the **Chapter 6** for the Machine-Side Converter (MSC). It is worth to state that, as will be explained in the following chapters, the control system used in this work handles the DC voltage level from the grid side while the active power output is imposed by the MSC. This is a commonly used and well-known control structure and many examples can be found in the literature, although other control schemes have been proposed showing interesting results their analysis is not included in this thesis.

2.2.1 Power converter pulse sequence control

Two Voltage Source Converters (VSC) compose the back-to-back (B2B) converter. This converter regulates its voltage by switching the IGBT bridge located between the AC and the DC sides of each VSC. The switching sequence can be computed using many techniques that result in different quality waveforms and computational requirements. In a two-level converter, a well-known strategy is the Space-Vector Pulse Width Modulation (SVPWM), its principle is based on the eight switching states that are available for this configuration. As shown in the diagram in Fig. 2.8 six of the switching states produce different output vectors and the other two (0 and 7) result in a zero vector.

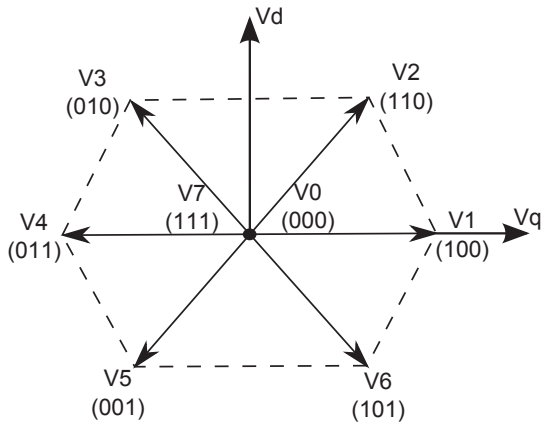

Figure 2.8: Space Vector sectors

The desired vector is obtained with a combination of the two adjacent switching vectors and the zero vectors. Then, switching in two levels, it is possible to reach, in average, the desired voltage vector. Using a carrier-based PWM can be computed the state of the IGBT switches (ON or OFF) for a switching period. An example of the resulting commutation states is shown in Fig. 2.9

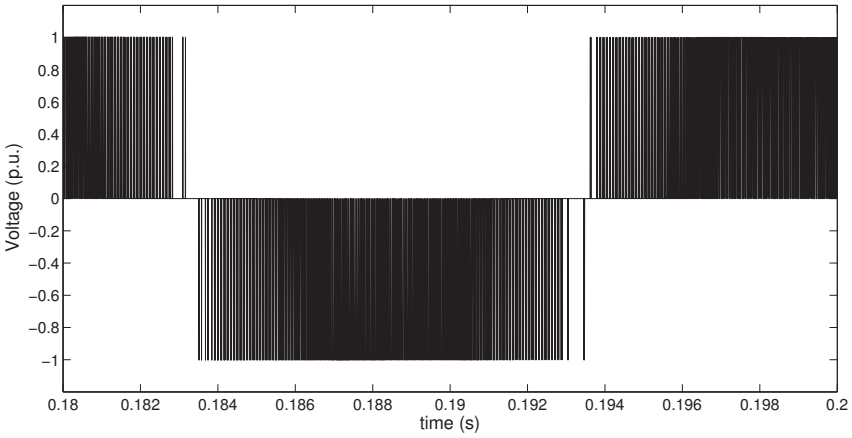

Figure 2.9: SVPWM line voltage commutation example

The modulation index (ratio between the amplitude of the modulating signal and the carrier) [64] is selected in accordance to the desired voltage rate and the current flow will vary in consequence. The faster the switching frequency is the higher the switching losses will be, on the other hand less ripple will appear in the electrical variables. This trade-off has to be considered before the commutation frequency is chosen and it may vary depending on the application.

3 Experimental setup

In this chapter an overview of the hardware used for testing the proposed controllers is provided. The experimental setup aims to reproduce the electrical subsystem of a PMSG-based WECS with a fully-rated back-to-back converter. A simplified version of the mechanical subsystem is also implemented but only to apply a load torque to the generator and is not intended to reproduce the behavior of the wind turbine rotor. Given the time constant difference between electrical and mechanical transients (especially for large wind turbines) this configuration provides a good framework to test the electrical control system. The laboratory equipment described in this chapter has been used to test the controllers and obtain the results included in **Chapters 5 and 6**.

3.1 Hardware overview

The setup emulates a wind energy conversion system where the rotor and gearbox are substituted by an induction motor as depicted in the schematic view in Fig. 3.1. The motor develops the load torque that is applied to the generator through a high-speed shaft. The motor is an ABB M2QA132S4A and its parameters are shown in Table. 3.1. The motor speed is controlled by the commercial motor drive Unidrive SP1406 from Emerson Industrial Automation (Fig. 3.2) with a rated power of 5.5 kW. The motor drive software can work in speed control or in torque control and is controlled remotely. In both control modes it is possible to select steps or ramps for the setpoints transition. Notice that the high-level speed controller was not implemented

due to the fact that the available equipment is not capable of reproducing the aerodynamic behavior of the wind turbine.

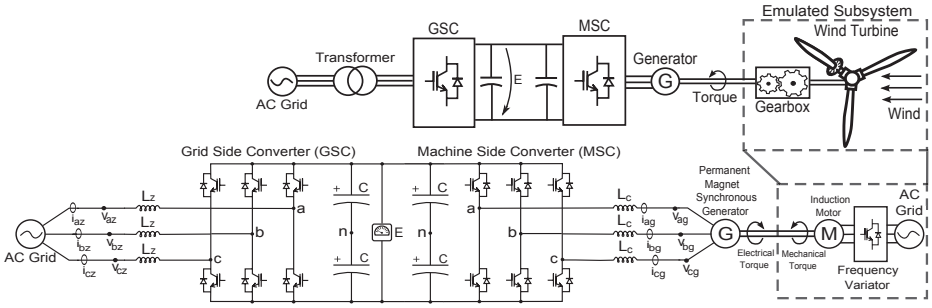

Figure 3.1: Schematic view of the experimental setup emulating a wind turbine based on PMSG.

Table 3.1: Parameters of the induction motor

Power	5.5 kW
Rated speed	1440 rpm
Voltage	400/690 V
Rated current	11.3 A
Pole pairs	2

The joint that links the motor with the generator has incorporated additional inertial discs that increase the mass and reduce the time constant of the mechanical subsystem. In this way the behavior of the system is closer to the one expected from wind turbines with multi-MW rated power. The total mass of the five discs is 80 kg and they can be attached together or individually reducing the final mass proportionally. As a result of adding the discs, the total inertia of the system is 1.598 $kg \cdot m^2$ providing an inertia constant of 3.5 seconds. The permanent magnet synchronous generator is a Unimotor fm (model: 142U2E300BACAA165240) from Emerson Industrial Automation, its parameters are shown in Table. 3.2.

The maximum torque that can be developed by the generator is 23.4 Nm, for short periods of time the torque can be increased beyond the rated torque but a temperature sensor will trip the device if this situation lasts too long.

Figure 3.2: Commercial motor drive

Table 3.2: Parameters of the permanent magnet synchronous generator

Power	5.65 kW
Rated speed	3000 rpm
Voltage	400 V
Rated torque	18 Nm
Pole pairs	3
Magnet flux	0.2591 Wb
Resistance	0.22 Ω
Inductance	2.9 mH

The generator includes an incremental encoder with a resolution of 4096 ppr (pulses per revolution) that provides speed feedback to the power converter. The fully-rated back-to-back converter is provided by Cinergia [66], it includes the capacitor bank, the IGBT bridges, the line inductances and the voltages and currents sensors. The characteristics of this device can be found in Table. 3.3 and in Fig. 3.3 a picture of the power converter where the main elements are labeled is shown.

Pictures of the main components of the complete experimental setup are shown in Fig. 3.4 including labels for each of them.

Table 3.3: Parameters of the back-to-back converter

Power	5.75 kW
Rated current	15 A
Capacitance	1020 μF
Resistance	0.3 Ω
Inductance	4.6 mH

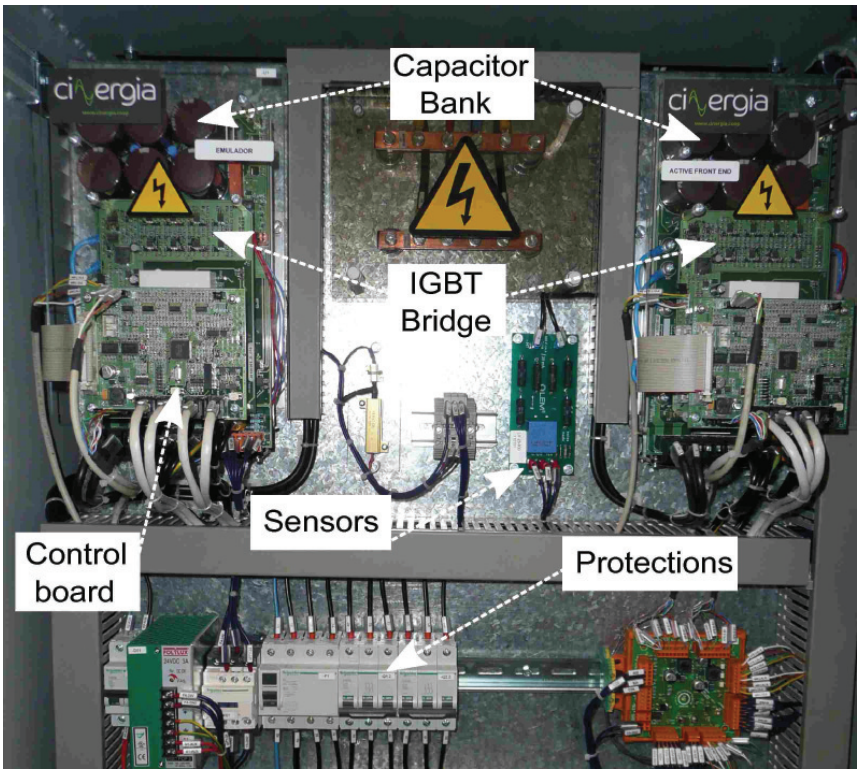

Figure 3.3: Back-to-back converter

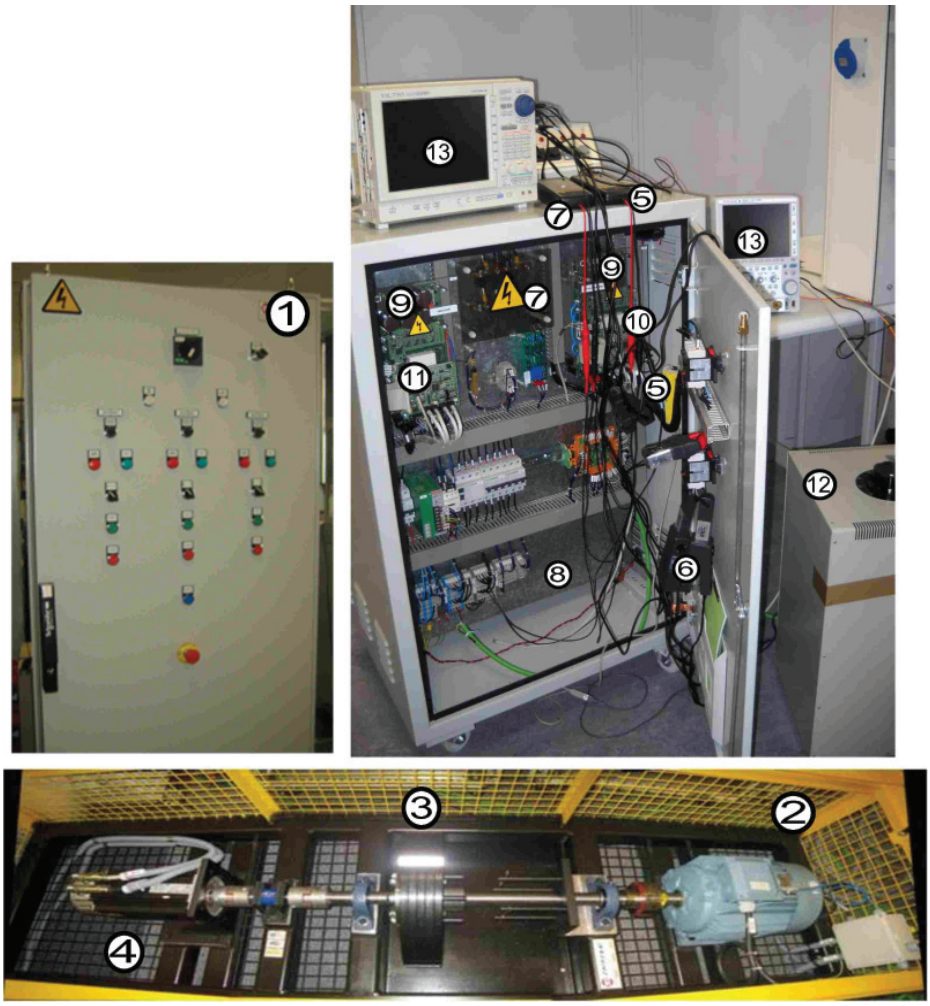

Figure 3.4: Experimental test bench: (1) motor drive, (2) induction motor, (3) axis with inertial discs, (4) permanent magnet synchronous generator, (5) AC voltage measurements, (6) AC current measurements, (7) DC voltage measurement, (8) line inductances (located behind), (9) capacitor bank, (10) machine-side converter, (11) grid-side converter, (12) transformer, (13) data acquisition system.

3.2 Loop configuration

In the previous section, the standard configuration of a WECS with a fully rated converter has been presented (Fig. 3.1). In order to test the controllers for the GSC a different approach, a loop configuration, was used. From the GSC point of view there can be different kind of power sources connected to the DC-link, the MSC can be considered a current source. In this configuration, sketched in Fig. 3.5, the current is recirculated from the GSC back to the MSC.

In this case the MSC can be called Emulation Side Converter (ESC) since it can emulate the behavior of different power sources. The loop configuration can result useful to test the performance of controllers for several (emulated) applications. During the experiments there were no observed interactions or disturbances between the AC sides of both converters.

3.3 Control Unit

In each VSC there is a control board that permits to control independently each side of the B2B converter. The control board has embedded a TMS320F2808 Digital Signal Processor (DSP) with 18 kB of Single-Access RAM memory and 100 MHz CPU speed that processes the sensors data, handles the CAN communication system and commands the IGBT bridge. The Code Composer software platform is used for debugging and compiling tasks and the interface between the software and the processor is done through a JtagJET C2000 from Signum Systems. This device can provide real-time communications with the processor while the algorithms are running facilitating the analysis of internal variables during the debugging process.

The DSP performs several tasks, in the first place the start-up and shut down sequence is implemented. In the start-up process the DC-link is connected to the AC grid through a diode bridge in order to increase the DC voltage. Once the DC voltage is stable the IGBT bridge is activated and the DC voltage setpoint is then reached through a ramp that limits the transient overshoot. When the converter is shutting down the IGBT bridge is disconnected from the DC-link and the energy accumulated in the capacitors is dissipated in a discharge resistor.

During normal operation the processor has to manage several subtasks in a limited amount of time. First of all a supervisory main process is constantly monitoring several signals (such as currents and voltages) in order to stop

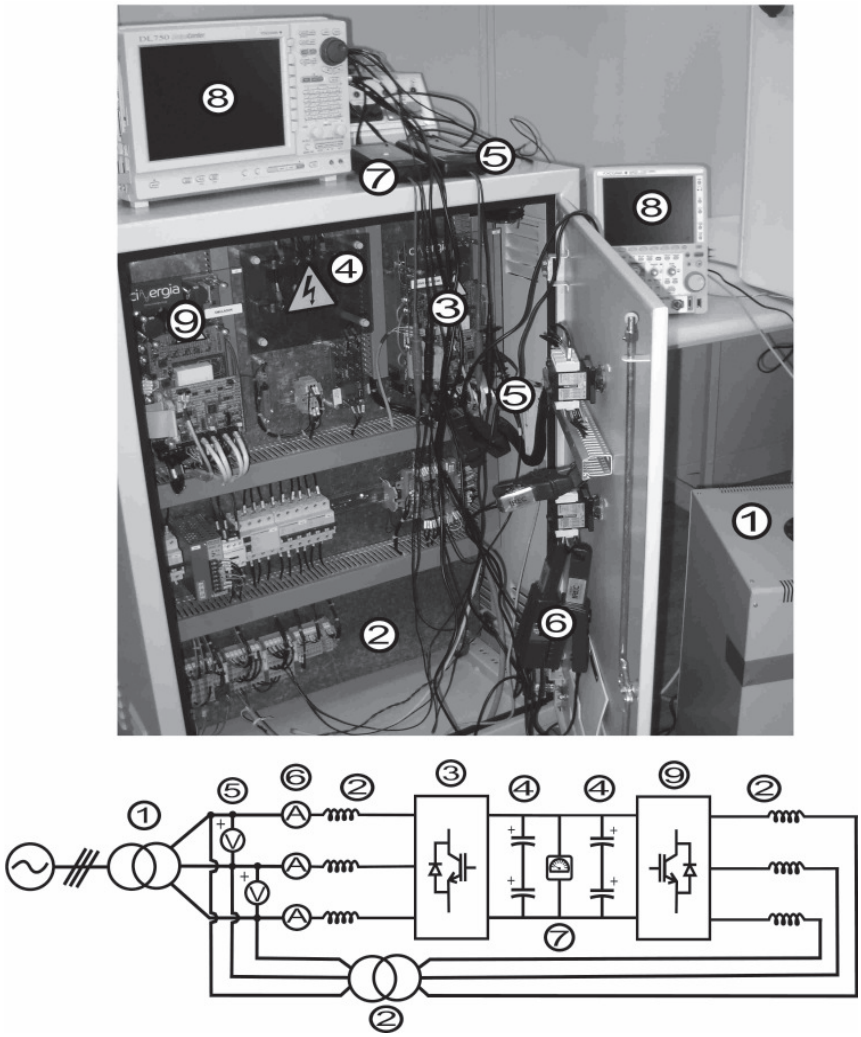

Figure 3.5: Schematic view of the experimental test bench: (1) Autotransformer, (2) Line inductances and isolation transformer (located behind), (3) Grid Side Converter, (4) Capacitor Bank, (5) AC Voltage measurement, (6) AC Current measurement, (7) DC Voltage measurement, (8) Data acquisition system, (9) Emulation Side Converter (ESC).

the process execution if any of them presents abnormal behavior, in this way the triggering of physical protections is avoided. Another task consists in sampling all the measured signals using the Analog-to-Digital submodule and store the data for the control system and the supervisory process. In this task there is a Digital-to-Analog submodule as well that adapts the internal signals from the DSP to be captured by external measurement equipment. There is also a submodule that can handle CAN communications between both DSP and external devices but this feature has not been used during the development of this thesis. The last of the actions that the DSP has to manage is the generation of the pulse sequence that commands the switching of the IGBT bridge which has, as a limit, the switching frequency of the semiconductors.

After executing the tasks described above the control system performs its calculations. The amount of computing time and memory required by the control system may be an important issue if enters in conflict with other tasks. In order to avoid this situation the controllers tend to be kept as simple and reduced as possible. In this sense the algorithms proposed in this work follow the same philosophy and aim to keep the computational requirements in the minimal expression while enhancing the controllers performance as much as possible.

4 Modeling and validation of a WECS with field test data

In this chapter, a model of a Wind Energy Conversion System (WECS) is detailed including the turbine aerodynamic and mechanical model [67] and the electrical system. The results of the simulations done with this model are compared with data measured in field tests performed with an operational WECS. Voltage sags have been provoked in a 3 MW DFIG-based wind turbine in order to obtain information of the ride-through performance. Different types of line faults have been tested considering symmetrical and asymmetrical voltages. A detailed comparison between simulated and measured data is presented. A study of the validation process described in the Spanish and German grid codes has been conducted to assess the matching level between the model and the real system.

4.1 Modeling

4.1.1 Wind turbine modeling

The power generated by the wind turbine comes from the kinetic energy of the wind and depends on the power coefficient (C_P). The power extracted by the wind turbine can be expressed as

$$P_{ww} = C_P P_{wind} = C_P \frac{1}{2} \rho A v_w^3 \tag{4.1}$$

where P_{wind} is the kinetic power of the air stream, ρ is the air density

assumed to be constant, A is the surface covered by the wind wheel and v_w is the wind speed. The power coefficient C_P as a function of the speed of wind speed and the turbine speed can be approximated by the analytic expression [63]

$$C_P\left(\lambda, \theta_{pitch}\right) = c_1 \left(c_2 \frac{1}{\Lambda} - c_3 \theta_{pitch} - c_4 \theta_{pitch}^{c_5} - c_6 \right) e^{-c_7 \frac{1}{\Lambda}} \tag{4.2}$$

where $[c_1 \dots c_9]$ are characteristic constants for each wind turbine, θ_{pitch} is the blade pitch angle and Λ is defined as

$$\frac{1}{\Lambda} = \frac{1}{\lambda + c_8 \theta_{pitch}} - \frac{c_9}{1 + \theta_{pitch}^3} \tag{4.3}$$

where λ is the so-called tip speed ratio and it is defined as

$$\lambda = \frac{\omega_t R}{v_w} \tag{4.4}$$

where ω_t is the turbine speed and R is the turbine radius. The mechanical torque applied to the shaft can be easily computed as $\Gamma_t = P_{ww}/\omega_t$

4.1.2 Blade pitch actuator

The mechanism governing the blade angle is usually a hydraulic actuator or a servomotor that can be modeled as a first order system with a time constant τ_{pitch} [68] as

$$\theta_{pitch} = \frac{1}{\tau_{pitch} s + 1} \theta_{pitch}^* \tag{4.5}$$

where θ_{pitch}^* is the pitch angle reference.

4.1.3 Drive train modeling

The drive-train of a WECS comprises the wind wheel, the turbine shaft, the gearbox, and the generator rotor shaft. A model with two masses is used treating the wind wheel as one inertia J_t and the gearbox and the generator rotor as another inertia J_m connected through the elastic turbine shaft with a k angular stiffness coefficient and a c angular damping coefficient. The dynamics resulting are described as [69, 70]

$$\begin{Bmatrix} \dot{\omega}_m \\ \dot{\omega}_t \\ \omega_m \\ \omega_t \end{Bmatrix} = \begin{pmatrix} \frac{-\eta^2 c}{J_m} & \frac{\eta c}{J_m} & -\frac{\eta^2 k}{J_m} & \frac{\eta k}{J_m} \\ \frac{\eta c}{J_t} & -\frac{c}{J_t} & \frac{\eta k}{J_t} & -\frac{k}{J_t} \\ 1 & 0 & 0 & 0 \\ 0 & 1 & 0 & 0 \end{pmatrix} \begin{Bmatrix} \omega_m \\ \omega_t \\ \theta_m \\ \theta_t \end{Bmatrix} + \begin{pmatrix} \frac{1}{J_m} & 0 \\ 0 & \frac{1}{J_t} \\ 0 & 0 \\ 0 & 0 \end{pmatrix} \begin{Bmatrix} \Gamma_m \\ \Gamma_t \end{Bmatrix} \quad (4.6)$$

where θ_t and θ_m are the angles of the low-speed axis and the generator shaft, ω_t and ω_m are the angular speed of the low-speed axis and the generator, τ_t is the torque applied to the turbine axis by the wind rotor, τ_m is the generator torque and η is the gear ratio.

4.1.4 Generator modeling

Two different types of generator technologies are considered in this thesis: a Doubly-Fed Induction Generator (DFIG) and a Permanent Magnet Synchronous Generator (PMSG). The DFIG is used for model validation purposes in this chapter since the data available is related to this type of machine. On the other hand, in the following chapters, the PMSG technology will be used for control system design. Nevertehless the PMSG is also described in this section to concentrate the WECS modelling information in one chapter.

Doubly-Fed Induction Generator

The generator of a DFIG is a wounded rotor asynchronous machine. The machine voltage equations can be written on the synchronous reference qd-frame [71] representation as [72]

$$\begin{Bmatrix} v_{sq} \\ v_{sd} \\ v_{rq} \\ v_{rd} \end{Bmatrix} = \begin{bmatrix} L_s & 0 & M & 0 \\ 0 & L_s & 0 & M \\ M & 0 & L_r & 0 \\ 0 & M & 0 & L_r \end{bmatrix} \frac{d}{dt} \begin{Bmatrix} i_{sq} \\ i_{sd} \\ i_{rq} \\ i_{rd} \end{Bmatrix} + \begin{bmatrix} r_s & L_s\omega_s & 0 & M\omega_s \\ -L_s\omega_s & r_s & -M\omega_s & 0 \\ 0 & sM\omega_s & r_r & sL_r\omega_s \\ -sM\omega_s & 0 & -sL_r\omega_s & r_r \end{bmatrix} \begin{Bmatrix} i_{sq} \\ i_{sd} \\ i_{rq} \\ i_{rd} \end{Bmatrix} \quad (4.7)$$

where L_s and L_r are the stator and rotor windings self-inductance coefficient, M is the coupling coefficient between stator and rotor windings, r_s and r_r

are the stator and rotor resistance, ω_s is the electrical angular speed at the stator of the machine and s is the slip $s = (\omega_s - \omega_r)/\omega_s$, with $\omega_r = p \cdot \omega_m$, where ω_r is the electrical angular speed of the rotor and p is the number of pole pairs. Torque and stator reactive power are the variables to be controlled by the rotor-side converter. Their expressions yield

$$\Gamma_m = \frac{3}{2} pM \left(i_{sq} i_{rd} - i_{sd} i_{rq} \right) \tag{4.8}$$

$$Q_s = \frac{3}{2} \left(v_{sq} i_{sd} - v_{sd} i_{sq} \right) \tag{4.9}$$

Permanent Magnet Synchronous Generator

In the PMSG, permanent magnets generate the magnetic flux of the rotor. In the surface-mounted PMSG, these magnets are placed on the rotor surface, with this configuration the magnetizing inductances are equal ($L = L_q = L_d$) in the synchronous reference frame. The model of the generator can be then expressed as

$$\begin{aligned} v_q &= r_s i_q + \omega_r L i_d + w_r \Psi - L \frac{di_q}{dt} \\ v_d &= r_s i_d - \omega_r L i_q - L \frac{di_d}{dt} \end{aligned} \tag{4.10}$$

where Ψ is the permanent magnet flux linkage of the generator. The torque applied by the generator and the reactive power are given by

$$\Gamma = \frac{3}{2} p \Psi i_{gq}, \tag{4.11}$$

$$Q_g = \frac{3}{2} v_{gq} i_{gd}, \tag{4.12}$$

4.1.5 Converter modeling

An IGBT voltage-source back-to-back converter connected to the rotor and fed by a DC bus acts as an active rectifier [73] connected to a three phase grid. For the purpose of control design, a VSC can be modelled as three AC voltage sources and a DC current source with a capacitor branch (see Fig. 4.1). The current provided by this source is a function of the power flow between the AC and the DC sides.

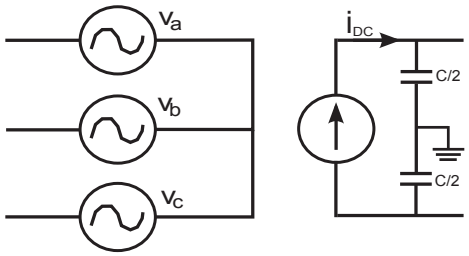

Figure 4.1: Simplified model of the VSC converter

A schematic plot of the converter (including the DC chopper) connected to the rotor of the generator can be seen in Fig. 4.2.

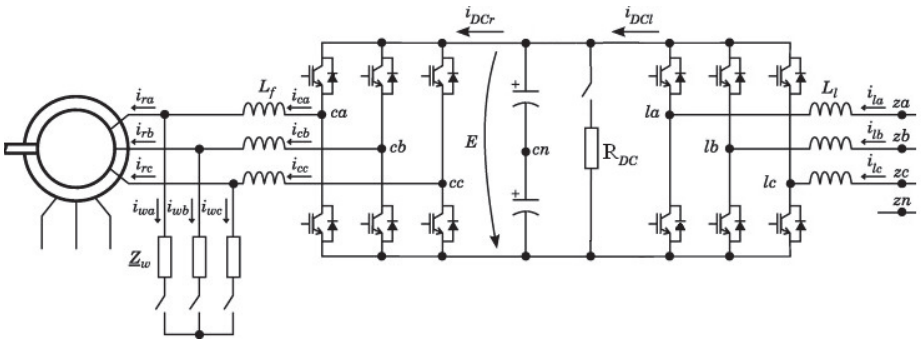

Figure 4.2: Back-to-back converter connection scheme

For wind turbine and grid integration studies, it can be assumed that the switching frequency is high (usually over 1 kHz) and the high-frequency components of the voltage signals generated by the inverters are filtered by the low pass nature of the machine and the grid side circuit. The dynamics of the grid-side electrical circuit are described as

$$v_z^{abc} - v_l^{abc} - (v_{cn} - v_{zn}) \begin{Bmatrix} 1 \\ 1 \\ 1 \end{Bmatrix} = R_l i_l^{abc} + L_l \frac{d}{dt} i_l^{abc} \tag{4.13}$$

$$v_{cn} - v_{zn} = \frac{1}{3} \left(v_{za} + v_{zb} + v_{zc} - v_{la} - v_{lb} - v_{lc} \right) \tag{4.14}$$

where v_z^{abc} and v_l^{abc} are the *abc* voltages of the grid and the AC side of the converter (Fig. 4.3), i_l^{abc} are the currents at the AC side of the converter, v_{cn}

and v_{zn} are the neutral voltages, R_l is the resistance of the filter inductors and L_l is the inductance of the filter. The voltage of the DC bus is described as [65]

$$\frac{d}{dt}E = \frac{1}{C}\left(i_{DCl} - i_{DCr}\right) \tag{4.15}$$

where E is the voltage of the DC bus, i_{DCl} is the current through the DC side of the grid-side inverter, i_{DCr} is the current through the DC side of the rotor-side inverter and C is the capacitance of the DC-link.

The DC-chopper consists on a resistor and a switch connected to the DC bus, in parallel with the DC-link capacitor, which is controlled by an IGBT when a DC over-voltage is detected. Its mission is to dissipate the excess of energy that cannot be evacuated to the grid during a fault. When the DC-chopper is activated the DC voltage expression becomes

$$\frac{d}{dt}E = \frac{1}{C}\left(i_{DCl} - i_{DCr} - \frac{E}{R_{DC}}\right) \tag{4.16}$$

where R_{DC} is the equivalent resistance of the DC-chopper. The crowbar is located between the rotor of the machine and the rotor-side converter (Fig. 4.2). Its mission is to short-circuit the rotor windings preventing damages due to over-voltages.

The currents on the AC side of the rotor-side converter when crowbar protection is activated [69, 70] can be expressed as

$$i_c^{abc} = i_r^{abc} + i_w^{abc} \tag{4.17}$$

where i_c^{abc} and i_w^{abc} are the rotor-side converter and the crowbar abc current vectors.

4.1.6 Impedances modeling

The model of the impedances includes the conductors that connect the power transformer to the grid-side converter and to the stator of the generator. A simplified model scheme (Fig. 4.3) has been used.

The transformer has been described as a three-phase transformer with three windings, in Fig. 4.4 the considered transformer scheme is shown. The complete model of the transformer can be found in [74].

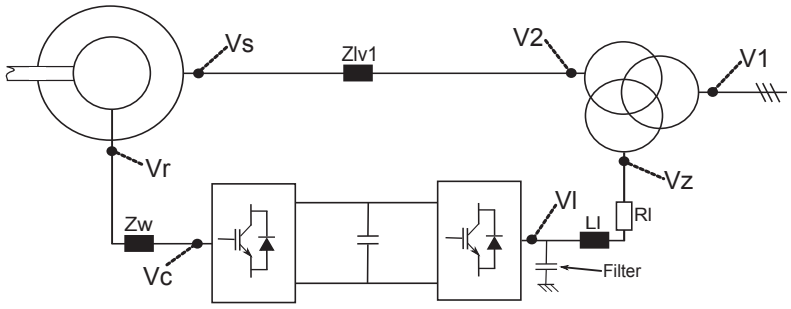

Figure 4.3: Impedances model

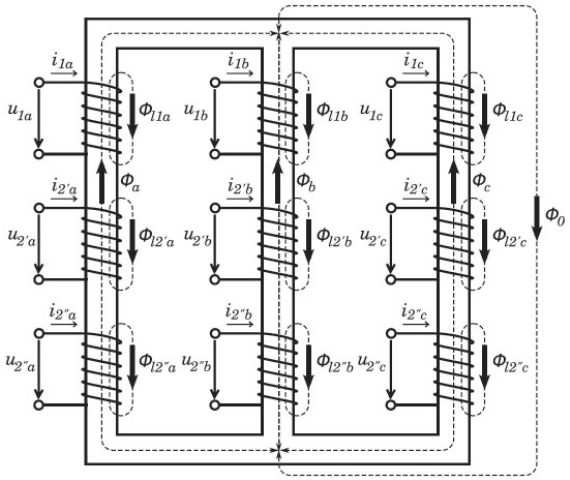

Figure 4.4: Transformer Scheme

4.2 Control system

There are two levels of control in a WECS. The high-level control or speed control actuates on the blade pitch angle and gives torque reference signals to the converter. The low-level control or converter control drives the converter IGBTs to properly follow the reactive power, torque and DC voltage reference signals. Vector control, including positive and negative sequence was used in order to work with unbalanced disturbances. The control system is described in detail in [74].

4.3 Simulation and field test results

In this section a comparison between simulation results and measurements obtained from field tests performed with a real DIFG-based WECS is shown.

4.3.1 Field tests

In order to validate a model field data have to be gathered first. The data is obtained in a controlled environment where the grid fault is provoked and several sensors measure and sample the information from the main points of interest. Once the data is available the electrical model can be evaluated using the diagram of Fig. 4.5 which is equivalent to the system during the field test.

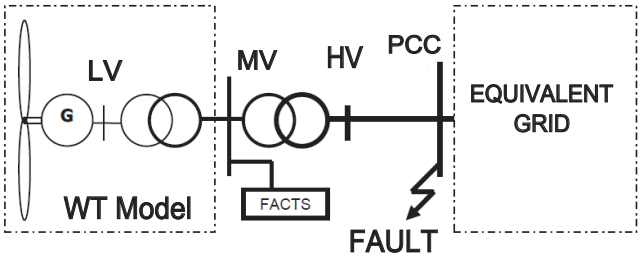

Figure 4.5: One-line diagram of the electrical system for grid fault tests [1]

The following tests have been performed on a wind turbine model ECO-100 from Alstom-Wind (Fig. 4.6). ECO-100 is a three-bladed horizontal axis wind turbine, its wind wheel diameter measures 100 m, offers a swept area of 7980 m^2 and it is suitable for use in low, medium and high wind speeds. The turbine starts rotating at a cut-in wind speed of 3 m/s, gradually ceases its operation at 25 m/s and totally stops when the wind speed reaches 34 m/s. The rated power of ECO-100 is 3 MW and its rated voltage at the stator of the generator is 1000 V. It incorporates a gearbox transmitting the mechanical torque from the low-speed shaft in the wind wheel to the high-speed shaft in the rotor of the generator [2].

Several tests have been done to evaluate the fault ride-through capabilities of the machine by provoking balanced and unbalanced faults under different operational regimes. During the tests, voltages and currents at the stator, rotor-side converter and grid-side converter and also voltage and current on the primary winding of the transformer have been measured. By means of a data acquisition system the main variables have been captured from the con-

Figure 4.6: ECO-100 wind turbine of Alstom-Wind [2]

verter such as reference signals, torque, generator speed, active and reactive power, DC-bus voltage level and DC-chopper activation. The measurement points during field tests are depicted in Fig. 4.7.

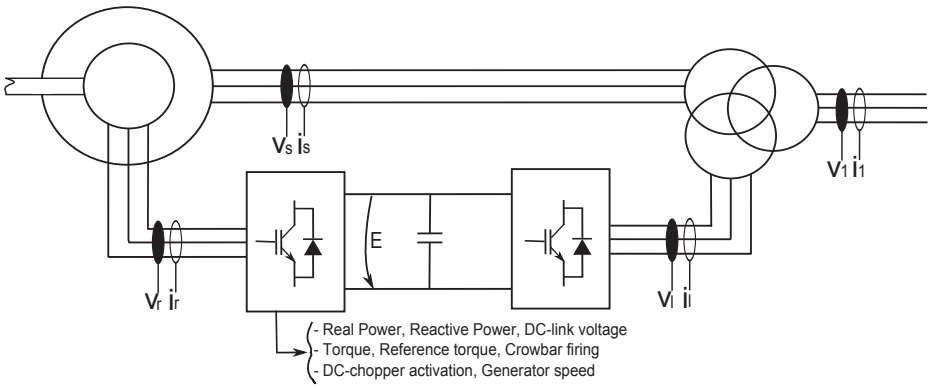

Figure 4.7: Field test measurements location

4.3.2 Simulation

The software platform where the simulations have been performed is Matlab-Simulink® using Bogacki-Shampine solver. Electrical parameters of the model have been provided by the manufacturer as well as rules for protections triggering. In this model, only electrical and control parts have been implemented. The input data needed to run a simulation is the generator speed, voltage of the wind farm grid (medium voltage) and references for torque, reactive power and DC-bus voltage. The rest of the data will be obtained as an output result or as internal variables of the system. A schematic view of the simulation model can be seen in Fig. 4.8 where input and output variables are indicated.

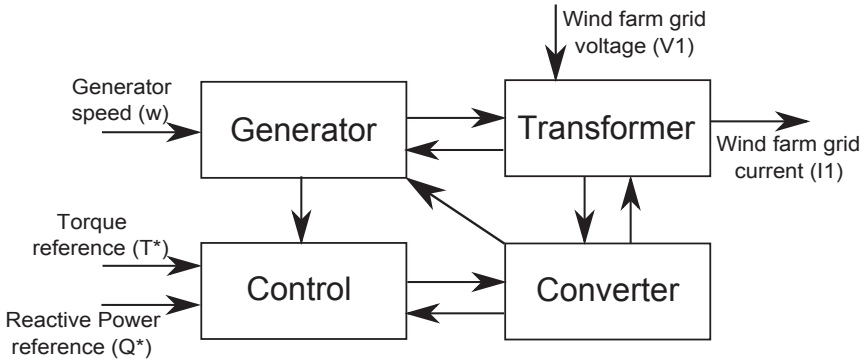

Figure 4.8: Simulation model input/output scheme

4.3.3 Results

Two voltage sags have been chosen to test the behavior of the model facing different situations. One of the field tests presents a symmetrical (3-phase) voltage sag (T1) while the other test is an asymmetrical (2-phase) one (T2). These selected faults have different voltage drops and durations and the main variables performance is shown for each case. The turbines were also working at different operating points (partial or full-load region) in each case in order to show the characteristics of the ride-through performance under various conditions. Voltage sag starts at second 19.5 in all cases.

Test 1

This test consisted on a 3-phase 0% voltage sag during 250 ms while the WECS is operating in the full-load region. In Fig.4.9 the measurements of voltage and current of the wind farm grid (primary of the transformer) are plotted. In Fig.4.10 the 3-phase current obtained from the simulation is shown (note that the voltage is an input for the model). A comparison between one phase of the simulated and measured current can be seen in Fig.4.11.

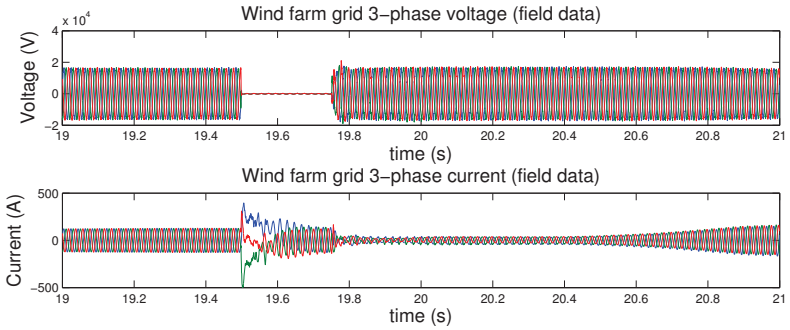

Figure 4.9: Wind farm grid measured voltage and current. V=0 pu, t=0.25s, 3-phase voltage drop

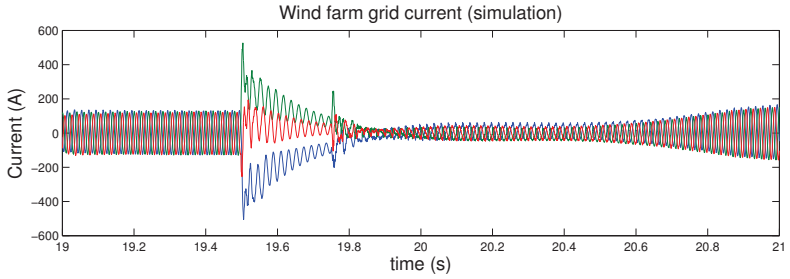

Figure 4.10: Wind farm grid simulated current. V=0 pu, t=0.25s, 3-phase voltage drop

Real power drop and recovery is shown in Fig.4.12, power generation reduction becomes important during outages since the capacity to evacuate energy drops drastically. In Fig.4.13 reactive power generation can be observed, the injection of reactive current into the grid during voltage dips is

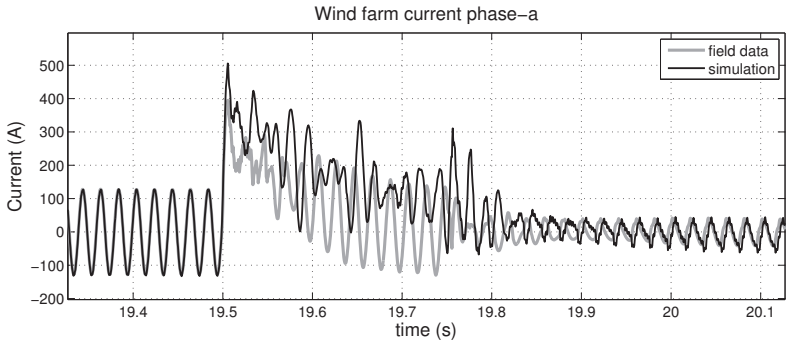

Figure 4.11: Wind farm grid current. V=0 pu, t=0.25s, 3-phase voltage drop

an ancillary service required by several grid codes.

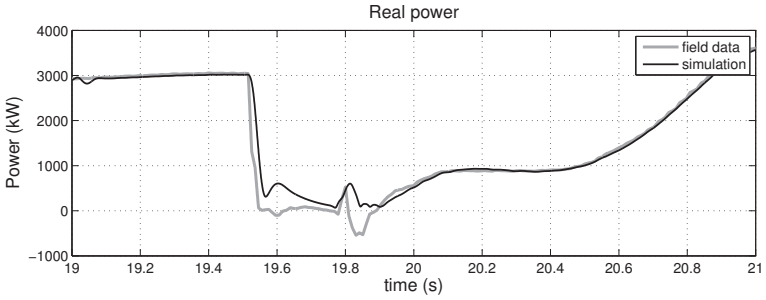

Figure 4.12: Active power. V=0 pu, t=0.25s, 3-phase voltage drop

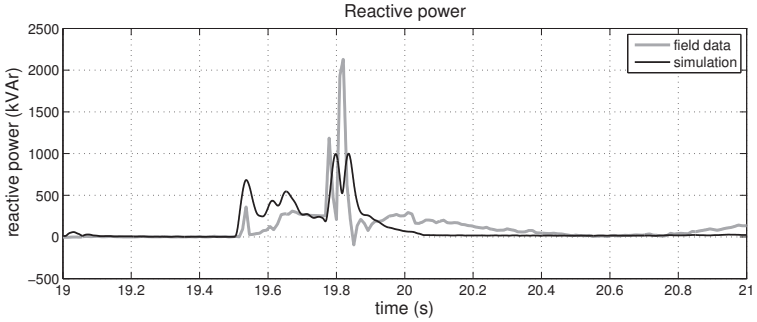

Figure 4.13: Reactive power. V=0 pu, t=0.25s, 3-phase voltage drop

Test 2

This test consisted on a 2-phase 50% voltage drop during 500 ms while the WECS is operating in the partial-load region. In Fig.4.14 the measured voltage and currents at the transformer primary are shown. In Fig.4.15 the 3-phase currents obtained from simulation are plotted. A detail of one phase of the simulated and measured current can be seen in Fig.4.16.

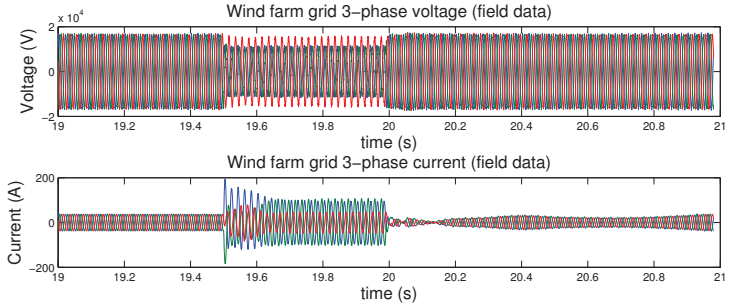

Figure 4.14: Wind farm grid measured voltage and current. V=0.5 pu, t=0.5s, 2-phase voltage drop

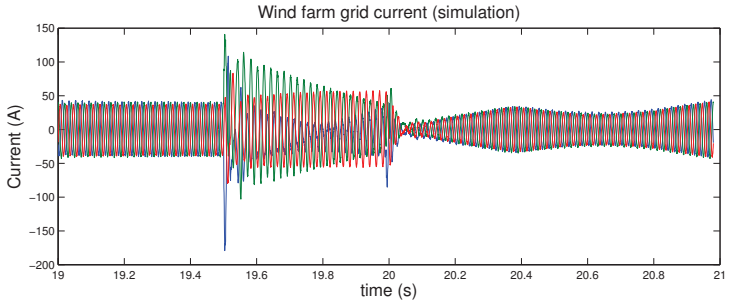

Figure 4.15: Wind farm grid simulated current. V=0.5 pu, t=0.5s, 2-phase voltage drop

Active power drop and recovery are shown in Fig.4.17, power generation reduction becomes important during outages since the capacity to evacuate energy drops drastically. In Fig.4.18 reactive power generation can be observed, the injection of reactive current into the grid during voltage dips is an ancillary service required by many of the grid codes.

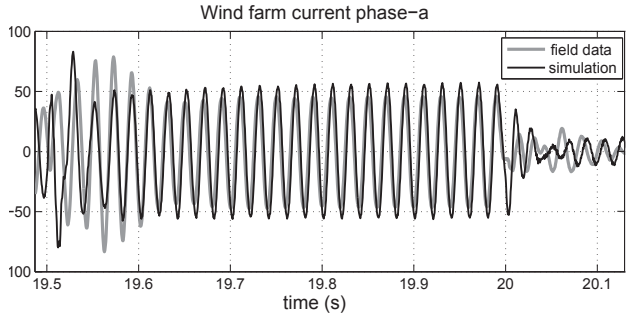

Figure 4.16: Wind farm grid current. V=0.5 pu, t=0.5s, 2-phase voltage drop

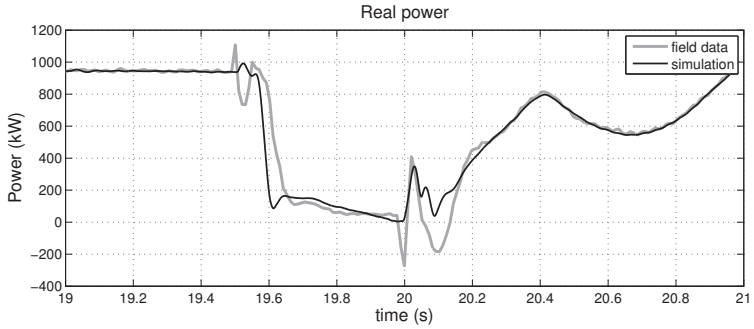

Figure 4.17: Active power. V=0.5 pu, t=0.5s, 2-phase voltage drop

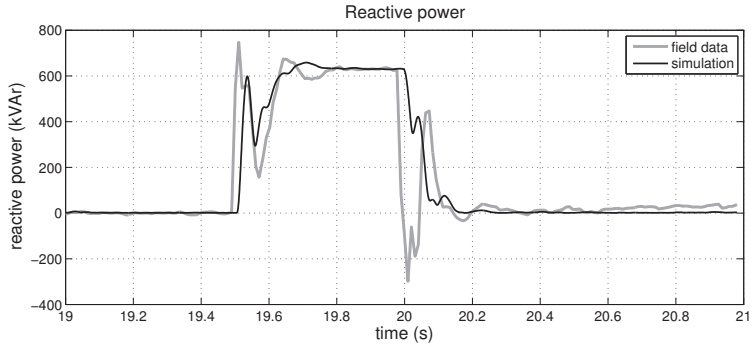

Figure 4.18: Reactive power. V=0.5 pu, t=0.5s, 2-phase voltage drop

The variables plotted in this section are the values demanded by the grid codes to validate the model according to the regulation. These are the main values of the wind turbine performance and the most important characteristics for the grid operator in order to ensure the system stability.

4.4 Validation

In order to evaluate the accuracy of the modeling the guidelines provided by the grid codes are followed. The grid codes are a set of rules determined by each country in order to regulate the electrical system. Regarding model validation they aim to evaluate, among others, the effects of transient actions. Two of the most advanced regulations at the time this work was done were the Spanish and the German grid codes. It is interesting to follow two different set of rules and compare the results of the validation process, furthermore, in this section, a model validation process according to Spanish and German grid codes is performed. These grid codes are still being developed so the last draft released is considered [20, 1, 3, 21]. Previous to the validation results the validation process is explained and the key concepts will be introduced.

4.4.1 Spanish grid code

The validation process of the Spanish grid code is based on [20] and the draft [1], these procedures have been designed for 500 ms long voltage drop to a 20% of grid's nominal voltage. As the grid code states, the voltage and current have to be measured at the primary windings of the transformer if it is included in the simulation model. The data acquisition process has to be done during 1 second starting 0.1 seconds before the voltage drop and the sampling frequency has to be at least 5 kHz.

The type of tests to be performed are also regulated in the grid codes, as an example the field tests requested by the Spanish grid code are summarized in Table 4.1.

Table 4.1: Types of tests requested by the Spanish grid code [1]

Fault	Residual voltage	Time (ms)	Operating point
3-phase	$\leq$23%	$\geq$300	$\geq$80% $P_{nominal}$ $\leq$40% $P_{nominal}$
2-phase	$\leq$70%	$\geq$300	$\geq$80% $P_{nominal}$ $\leq$40% $P_{nominal}$

Once the data is recorded the positive sequence will be extracted and the RMS value of its fundamental component will be used to compute active and reactive power according to (4.18) and (4.19).

$$P = 3U^{+}I^{+}cos\psi \tag{4.18}$$

$$Q = 3U^{+}I^{+}sin\psi \tag{4.19}$$

In the Spanish grid code, the accuracy is computed with respect to the nominal value as expressed in (4.20). Data with less than a 10% of deviation will be valid. This expression is not weighted and it is constant along the process and for the two variables of interest: active and reactive power. The accuracy is

$$\Delta x(\%) = \left| \frac{x_{measured} - x_{simulated}}{x_{nominal}} \right| \cdot 100 \leq 10\% \tag{4.20}$$

where x can be either active or reactive power. If more than an 85% of the samples are not exceeding this 10% of deviation allowed the model will be declared as validated. The validation results can be seen in Table 4.2 describing the voltage drop characteristics and the percentage of accuracy obtained in both variables.

Table 4.2: Spanish grid code validation results chart

Voltage drop	P(%)	Q(%)
T1 (3-ph, 0%, 250ms)	93.21%	87.33%
T2 (2-ph, 50%, 500ms)	98.63%	97.45%

4.4.2 German grid code

The model validation process of the German grid code is based on [3] and the data acquisition system is described in [21]. Since these drafts are not completed a process similar to [75] has been followed. According to this regulation, field test and simulation data have to be classified in three stages (before, during and after the transient) defining then the following three time ranges:

- A: time to voltage drop;
- B: time from voltage drop to fault rectification;

- C: time after fault rectification.

An example of these divisions can be seen in Fig 4.19 where the differences in the time ranges are illustrated. Transient and steady-state ranges will be differentiated for A, B and C. The variables are considered to be in steady-state when its value remains within a tolerance band of ±10% around a constant defined value. For evaluation A, B and C ranges are weighted as indicated in Table 4.3.

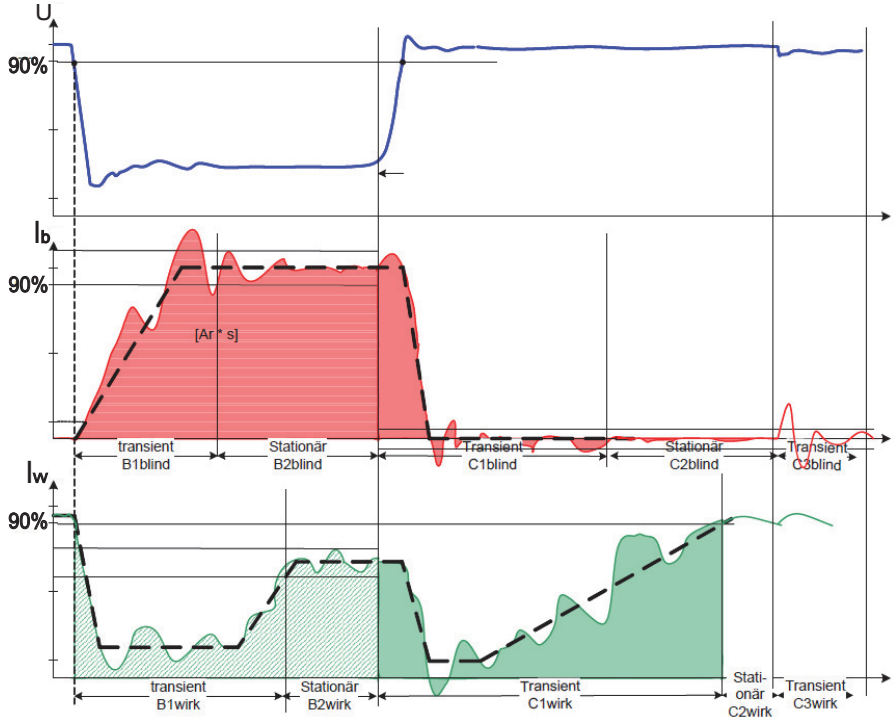

Figure 4.19: Example of division of active and reactive currents into transients and steady-state (or quasi steady-state) ranges in the German grid code [3]. (Note: blind=reactive, wirk=active, stationär=steady-state)

By weighting the results this regulation gives more importance to the behavior of the model during the grid fault than the Spanish grid code. In consequence, the results may be proved different for each regulation. There are also differences in the minimum requisites to pass the validation process,

Table 4.3: Weighted ranges according to the German grid code

Range	A	B	C
Percentage	10%	60%	30%

while the Spanish grid code demands an accuracy of at least 85% in all tests, the German grid code requires results between 80% and 93% accurate depending on the type of test (balanced or unbalanced) and the time range. Expression (4.21) gives the global error as a result of the validation process. For 0% voltage drops range B cannot be evaluated, furthermore, only A and C ranges will be considered.

$$e_g = \frac{0.1}{t_A}\sum_{iA} e_{iA}T_{iA} + \frac{0.6}{t_B}\sum_{iB} e_{iB}T_{iB} + \frac{0.3}{t_C}\sum_{iC} e_{iC}T_{iC} \tag{4.21}$$

where t_A is the duration of the range A, i_A is the number of states (transient + steady-state) during range A, e_{iA} is the error of each range in the range A and T_{iA} is the duration of each state during range A. If the deviation for each state (transient or steady) and the global error are below the values indicated in Table 4.4 the model is considered validated.

Table 4.4: Error allowed for each variable and period

Error allowed	F1	F2	F3	FG
Active power	0.10	0.20	0.15	0.15
Reactive power	0.07	0.20	0.10	0.15
Reactive current	0.10	0.20	0.15	0.15

In Table 4.4, F1 is the average error allowed in steady-state ranges, F2 the average error allowed in transient ranges and F3 the maximum error allowed of the positive sequence in steady-state ranges and FG the average allowed global weighted error. The results obtained using this evaluation process are presented in Table 4.5. The variables considered for the validation process are active power (P), reactive power (Q) and reactive current (Ir), for each one steady-state (s), transient (t) and positive sequence (pos) are evaluated, maximum error (Max) is indicated and also the global error allowed.

Positive sequence analysis will be done only for asymmetric voltage sags. During 0% voltage drops variables (P, Q and Ir) are not defined and range B (transient) will not be considered according to the German regulation, global error cannot be computed either. The validation process has been performed for both field tests (T) shown above.

Table 4.5: German grid code validation results

			A	B	C	Max	Global	Max
T1	P	s	0.0095	×	—	0.10	—	×
		t	—	×	0.0422	0.20		
		pos	×	×	×	0.15		
	Q	s	0.0587	×	0.0453	0.07	—	×
		t	—	×	0.0762	0.20		
		pos	×	×	×	0.10		
	Ir	s	0.0576	×	0.0449	0.10	—	×
		t	—	×	0.0723	0.20		
		pos	×	×	×	0.15		
T2	P	s	0.0113	—	—	0.10	0.0681	0.15
		t	—	0.01005	0.0220	0.20		
		pos	0.0115	—	—	0.15		
	Q	s	0.0073	0.0687	0.0102	0.07	0.0630	0.15
		t	—	0.1539	0.0424	0.20		
		pos	0.0214	0.0307	0.0393	0.10		
	Ir	s	0.007	0.0946	0.0097	0.10	0.0839	0.15
		t	—	0.1690	0.0391	0.20		
		pos	0.0095	0.0393	0.0108	0.15		

4.5 Conclusions

This chapter has presented a complete model for a wind turbine generation system based on a doubly fed induction generator. The analyzed wind turbine have been described, along with the field tests done and data acquisition process. Simulation results have been compared to experimental data extracted from field tests, showing a good matching between simulations and field tests. Their values have been analyzed according to the Spanish and German regulations, describing the validation process in both cases. The model described is positively validated according to the results shown. The selected tests represent some of the most complex situations that a wind turbine can face in its operational life, including a 0% three-phase voltage sag and an unbalanced fault. The model of the electrical subsystem developed during this work can be adapted to a PMSG-based WECS with a fully-rated power converter as will be shown in the following chapter.

5 Grid-Side Converter Control

In this chapter, an optimal control strategy with three levels is proposed. The control system consists of an inner current loop and an outer voltage loop together with an anti-windup compensation. The three controllers are designed using optimal control tools with the aim of achieving a trade-off between reference tracking errors and control efforts. The proposed control presents a similar complexity to typical structures used in these systems but exploits the interaction among variables and the information provided by the complete model of the system. The design process of the controllers aim to maintain a PI structure in the current loop since it is easy to implement and its low order and simplicity provide numerical stability. By using the proposed design procedure more parameters are available to shape the response of the control system instead of one single parameter such as the bandwidth in the IMC technique [41].

Special attention is paid to those aspects related to the implementation in low-performance industrial computers. To this end the implementation-oriented formulation of the control strategy and the controllers design is proposed. The resulting controllers are implemented in an experimental test bench that incorporates a DSP. This type of processors are commonly found in power converters control [76] and are also used for many other industrial purposes. However, some limitations in terms of memory capacity and computing speed are inherent to these processors. The test bench developed to run the experiments is made of two VSC connected in back-to-back configuration, one side is acting as a power source and the other side has implemented the proposed control strategy.

This chapter is organized as follows. In section 5.1 a general view of the control system of the GSC and the basic concepts of the control theory used to develope the proposed controller are given. In Section 5.2 the modeling of the power converter is given and the main aspects are highlighted. In Section 5.3 the design of the controllers is explained including implementation-oriented details. Section 5.4 describes the experimental setup including its characterization parameters and the control implementation. In Section 5.5 the experimental results are shown and compared with simulations, in this way the assumptions made in the control design process can be validated. In Section 5.6 the conclusions of this work are summarized.

5.1 Introduction

In normal operation, the GSC regulates the DC voltage and tracks the reactive power reference signal. In general, a control scheme with a two-loop structure is used where the outer loop regulates the voltage and the inner loop the current. An example of this control structure is shown in Fig. 5.1 where E^* is the DC voltage setpoint and i_q^* and i_d^* are the current setpoints.

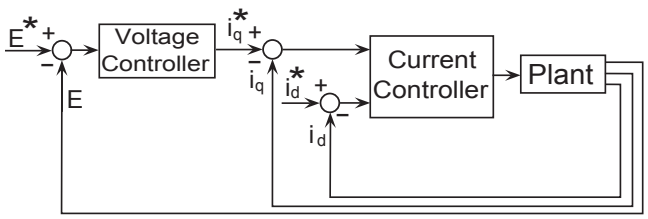

Figure 5.1: Generic block diagram of the control strategy

In general, linear PI controllers (sometimes with additional decoupling terms) are implemented in this control structure showing a reliable and acceptable performance. However, a different approach, using multi-variable optimal controllers, can provide flexibility in the control objectives introducing more specifications in the control design stage. Moreover, the complexity of the resulting controllers is not unnecessarily increased with respect to other simpler designs. $\mathcal{H}_\infty$ control theory can be employed to design the controllers of the currents and voltages. A general control problem formulation is obtained using the general configuration shown in Fig. 5.2, which can be defined as the lower LFT of G over K, $F_l(G, K)$, being G the plant

and K the controller. Using this approach the resulting control scheme can take the form of the two-loop structure shown in Fig. 5.1.

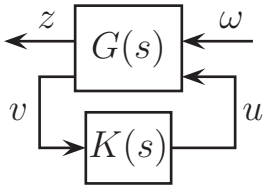

Figure 5.2: General control configuration

The control configuration is then described by

$$\begin{bmatrix} z \\ v \end{bmatrix} = G(s) \begin{bmatrix} \omega \\ u \end{bmatrix} = \begin{bmatrix} G_{11}(s) & G_{12}(s) \\ G_{21}(s) & G_{22}(s) \end{bmatrix} \begin{bmatrix} \omega \\ u \end{bmatrix}, \quad u = K(s)v \tag{5.1}$$

and the closed-loop transfer function from ω to z is given by the LFT

$$F_l(G, K) = G_{11}(s) + G_{12}(s)K(I - G_{22}(s)K)^{-1}G_{21}(s) \tag{5.2}$$

In the controller design stage, the performance specifications are included by adding weighting functions yielding an augmented plant. These functions shape the signals for different frequency ranges and their selection depends on the objectives of the controller. An example of their use is shown in the generic augmented plant depicted in Fig. 5.3 where $G(s)$ represents the system, $K(s)$ is the controller and W_i are the different weighting functions.

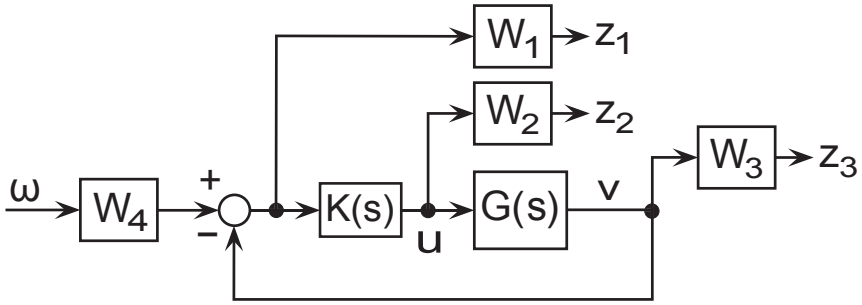

Figure 5.3: General setup for optimal controller design

Once the problem is formulated the solution can be found iteratively using specific software, the set of algebraic equations can be solved using the algorithm proposed in [77]. An interpretation of the $\mathcal{H}_\infty$ norm, in terms of performance, is that it minimizes the peak of the maximum singular value of $F_l(G(jw), K(jw))$, in this sense, it can be stated that $\mathcal{H}_\infty$ optimization is used to shape the singular values of specified transfer functions over frequency.

5.2 System description

The system considered in this study is an IGBT-based VSC. On the DC side of the converter there is a capacitor bank that links the power converter to other device. This other device connected to the DC-link could be a power generation unit, such as a wind energy generation system or a PV panel, or could be an energy storage system, such as a battery or a flywheel. In this work it is assumed that a power generation unit is connected, as a consequence the energy will always flow from the DC side (capacitor bank) to the AC side (power grid) but not in reverse. On the AC side of the power converter there is an inductance filter interconnecting the converter and the AC grid. The converter described here is usually known as Grid Side Converter (GSC) since its purpose is to interface a generation unit with the power grid.

It is common to use an average model of the converter, where high frequency effects are neglected for controller design purposes. In the average model the system is represented by three AC voltage sources and a DC current source linked by the power flow transfer balance. For modeling purposes, the grid is considered as an infinite bus connected to the converter through an RL branch. Voltage distortions, including high frequency harmonic voltages or unbalanced situations, are out of the scope of this work.

The currents of the system in qd reference frame [71] are given by

$$\dot{x} = Ax + Bv_l + Bv_z, \tag{5.3}$$

where

$$\begin{aligned} x &= \begin{bmatrix} i_q \\ i_d \end{bmatrix}, \quad v_l = \begin{bmatrix} v_{lq} \\ v_{ld} \end{bmatrix}, \quad v_z = \begin{bmatrix} v_{zq} \\ v_{zd} \end{bmatrix}, \\ A &= \begin{bmatrix} -R/L & \omega_e \\ -\omega_e & -R/L \end{bmatrix}, \quad B = \begin{bmatrix} -1/L & 0 \\ 0 & -1/L \end{bmatrix}, \end{aligned} \tag{5.4}$$

with i_q and i_d are the qd currents, v_{lq} and v_{ld} are the converter qd voltages, v_{zq} and v_{zd} are the grid qd voltages, R and L are the resistance and inductance of the filter and ω_e is the electrical angular velocity. This last variable will be assumed constant during the design stage. The grid voltages are projected into a voltage oriented synchronous reference frame which implies that v_{zd} can be assumed to be zero. The voltage v_l is the control signal and v_z is assumed to be constant.

If no DC power source is considered, the voltage in the DC bus is governed by

$$\frac{d\nu}{dt} = \frac{2}{C}\left(\frac{3}{2}v_{zq}i_q\right), \tag{5.5}$$

where $\nu = E_{DC}^2$. The variable ν is used to compute the DC voltage behavior instead of E_{DC} (actual voltage level) in order to linearize the system. As will be seen in Section 5.3, this choice produces the same control effect on the DC voltage regulation than the use of E_{DC} [70].

The generation unit connected to the DC side is considered to be a programmable current source, thus, the current flow can be arbitrarily selected. A schematic view of the system is sketched in Fig. 5.4. The inclusion of a current source does not affect particularly the control system design process, as is reflected in Section 5.3. In this scheme, the current source rules the amount of real power being delivered to the grid by the converter. Since the DC voltage has to be kept constant, all the current generated by the current source has to be evacuated. On the other hand, the reactive power generation can be arbitrarily chosen, within the current limitations of the converter.

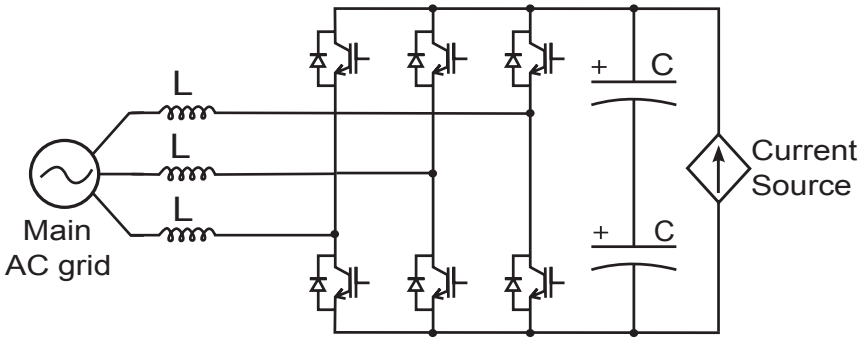

Figure 5.4: Schematic view of the grid side converter.

Being the Park transformation oriented to v_{zq} ($v_{zd} = 0$), the real and reactive power in the qd frame are given by

$$P = \frac{3}{2} v_{zq} i_q, \qquad Q = \frac{3}{2} v_{zq} i_d, \tag{5.6}$$

respectively. Since v_{zq} is usually constant in normal operation, the current i_q is associated to the real power and the current i_d is associated to the reactive power. Equations (5.3) and (5.5) describe the dynamics of the system, therefore it can be assumed to be a Linear Time-Invariant (LTI) system. The model presented here is used in Section 5.3 to design the controller, however, the equations defining real and reactive power are only used to compute the amount of power delivered by the converter.

Usually, the VSC shown in Fig. 5.4 is part of a back-to-back configuration, where two VSC are linked by their DC sides. Then, one VSC is connected to the AC grid and the other one to an energy source. As will be detailed in Section 5.4 the VSC interacting with the energy source will be referred to as Emulation Side Converter (ESC) in order to differentiate it from the GSC. A back-to-back converter is used for experimentation purposes but the control of the ESC is out of the scope of this work; its control depends on the particular energy source connected to it. Here, the ESC will emulate the current source that appears in Fig. 5.4. The goal of the GSC is to interact with the AC grid by injecting real and reactive power, the reactive power is chosen arbitrarily by the user while the voltage controller regulates the real power in order to maintain constant the DC voltage at the capacitor bank. The mission of the ESC (acting as a current source) is to inject current into the DC-link according to the reference signals selected by the user. In this configuration the energy always flows from the ESC to the GSC and, then, to the AC grid.

5.3 Control Design

In this section the main aspects to be considered in the design stage of the proposed controller are described. The mathematical solution to synthesize the controller is not described since commercial software is available for solving such problem, in this particular case the Robust Control Toolbox from Matlab has been used. $\mathcal{H}_\infty$ control theory is employed in this work to design the controllers of the currents and voltages. An optimal control avoids the need of additional decoupling terms in the control scheme, since interactions among variables are exploited during the design process. A multi-variable controller may be more effective than decentralized controllers

and may achieve a better performance [78]. In particular $\mathcal{H}_\infty$ optimal control is adopted here to be consistent with the implemented anti-windup scheme. The signals of the controller $K(s)$ are represented by the variables w and z and are used to state the performance specifications.

In $\mathcal{H}_\infty$ control theory, the controller is designed to minimize the ∞-norm of the closed loop transfer function from w to z ($\|T_{zw}\|_\infty$) or is forced to keep it below a given value $\gamma > 0$. This aim can be complemented with additional constraints on the closed-loop poles location [79]. This is particularly useful to make possible the implementation of the controller in discrete time. The optimization process is restricted to all the controllers that stabilize the plant and comply with the additional constraints. The performance specifications are included in the design stage by adding weighting functions. These functions filter the performance signals in different frequency ranges, limiting or enhancing the effort of the optimization process at those frequencies of interest. The weighting functions selection depends on the goals that the resulting controller aims to achieve.

The objectives of the GSC control are: regulate the DC voltage and make the converter deliver the amount of reactive current imposed by the user. To this end a control scheme with a two-loop structure is used, the inner loop corresponds to the current control and the outer one to the voltage regulation. The complete control scheme is shown in Fig. 5.5 where the voltage controller K_v, the current controller K_c and the anti-windup compensator K_{AW} are depicted. It can also be observed the feed-forward term v_{zqd}. The inclusion of the feed-forward component improves rejection of input voltages disturbances and improves the dynamic responses in the voltage control loop based on the fact that the loop gain becomes independent of the input voltage [80].

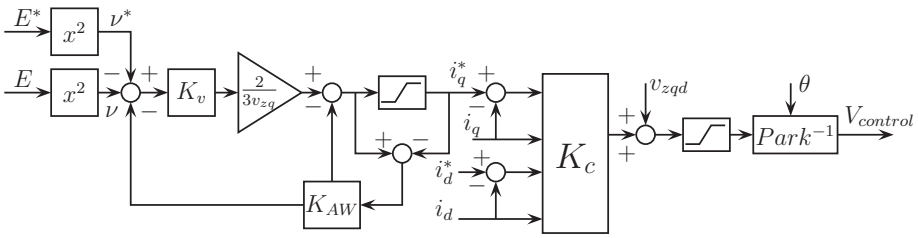

Figure 5.5: Block diagram of the control strategy.

The augmented plant considered to design the current controller is shown

in Fig. 5.6, where $G(s)$ represents the system given by (5.3) and is expressed as,

$$G(s) = C(sI_{2\times 2} - A)^{-1}B, \tag{5.7}$$

where $I_{2\times 2}$ is the identity matrix of 2×2 and $C = I_{2\times 2}$ because the output are the states of the system. The weighting functions are: W_{uc} that weights the control actions and W_{ec} that weights the integral of the current errors. The transfer function W_{uc} is chosen to avoid large control action values in high frequencies. The error signals are weighted with the function W_{ec} which is selected to provide zero steady-state performance error and to have a fast response tracking the current reference signals. It is desirable to include integral action in the control loop to ensure a zero steady-state error. However, this feature cannot be achieved by including an integrator (which has infinite gain at $s = 0$) in the weighting function W_{ec} because it would include an unstable and uncontrollable pole and the augmented plant would not be stabilizable. To circumvent this problem, the integral action is placed in the loop as shown in Fig. 5.6 [77]. In consequence the final controller will be the one given by the optimization algorithm but affected by the integral action, i.e.,

$$K_c(s) = \frac{1}{s}\tilde{K}_c(s) \tag{5.8}$$

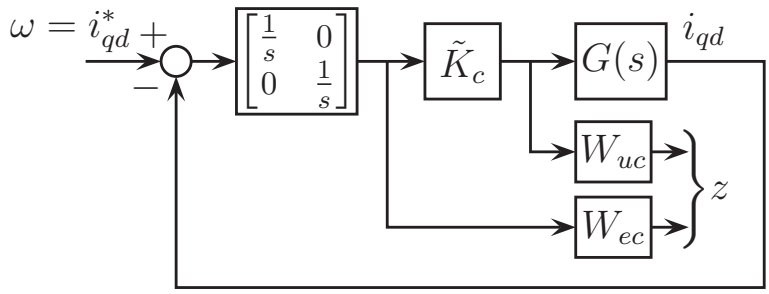

Figure 5.6: Setup for the current controller design.

The performance signals indicated as z in Fig. 5.6 correspond to the control actions and the integral of the current errors after the weighting functions. The selected weighting functions in the proposed design are constant matrices; the motivation of this choice is to obtain a low order controller.

The order of the controller is the order of the plant plus the order of the weighting functions. A controller with a low order provides numerical stability, less computational cost and an efficient implementation. Besides, with constant weights all the states of the augmented plant, the currents and the integrator states, are measurable. Thus, the controller design can be reduced to a state feedback problem and the optimal controller has a PI structure. That is, once the state feedback gain K_{sf} is obtained, the control law for the current loop is given by

$$v_{lqd} = K_{sf} \begin{bmatrix} \frac{1}{s}(i^*_{qd} - i_{qd}) \\ i_{qd} \end{bmatrix}, \tag{5.9}$$

where the subindex qd denotes the q and d components of the variable. Given the limitations that, in general, have the industrial equipments in terms of amount of memory and computing speed, the state feedback structure proposed in this work facilitates the implementation in a real system.

The outer loop that controls the DC voltage generates the reference signal of the q-component of the current i^*_q. The reference signal i^*_d is set by the reactive power demand and is not included in this control loop. Therefore, the voltage loop is reduced to a SISO design problem where the objective is to minimize the error of the square of the DC voltage (ν) with a reasonable control action. Now the plant to be controlled is the closed-loop transfer $T_{i^*_q i_q}$ where i^*_q (the reference after the saturation) and i_q. That is,

$$\begin{bmatrix} i_q \\ i_d \end{bmatrix} = GK_c(1 + GK_c)^{-1} \begin{bmatrix} i^*_q \\ i^*_d \end{bmatrix} = \begin{bmatrix} T_{i^*_q i_q} & T_{12} \\ T_{21} & T_{22} \end{bmatrix} \begin{bmatrix} i^*_q \\ i^*_d \end{bmatrix} \tag{5.10}$$

The saturation is included to avoid excessively high current references that may cause the triggering of the protections. The voltage controller is designed using a similar procedure to that used in the current controller design. However, in this case, the controller designed cannot be reduced to a state feedback problem.

In the final stage of the design process the anti-windup compensation is considered. This design is based on the scheme proposed in [81]. The aim of the anti-windup compensation is to minimize the effects of the current saturation by acting on the inputs and outputs of the voltage controller. The anti-windup scheme proposed is shown in Fig. 5.7, where K_v is the voltage controller designed in the previous step and K_{AW} is the anti-windup compensator. This compensator only acts during saturation and does not affect the normal operation. The design procedure is based in solving an $\mathcal{H}_\infty$ optimal problem in the way detailed in [81].

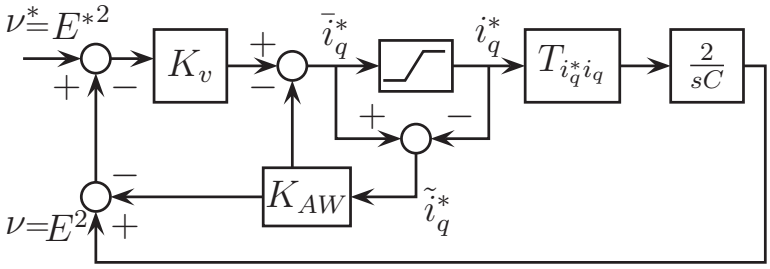

Figure 5.7: Simplified control scheme including voltage controller and anti-windup compensator.

5.4 Experimental Setup

The experimental setup is described in detail in **Chapter 3**. The aim of this test bench is to assess the performance of the $\mathcal{H}_\infty$ optimal control scheme for a VSC. The controller is developed with special emphasis on its implementation in a low performance industrial DSP aiming to reduce its computational requirements.Actually, the proposed system including the Phase-Locked Loop (PLL), Park transformations, signals sampling and Space-Vector Pulse-Width Modulation (SVPWM) computations require less than 40% of the available computing time between commutations considering the worst case execution time. Therefore, the control scheme discussed in the previous section is applied to the test bench shown in Fig. 5.8, where each element involved is labeled to facilitate their identification. The test bench consists of a back-to-back converter where one side of the converter corresponds to the system described in Section 6.2, i.e. the GSC. Notice that in the scheme sketched at the bottom of Fig. 5.8 the AC sides of both converters (GSC and ESC) are closing a loop and sharing the same AC grid, this configuration does not affect the results obtained as can be verified in Section 5.5.

The current source that appears in Fig. 5.4 is emulated in the test bench by the ESC. Since this converter behaves as a current source only the current controller is necessary. Given the symmetry of the back-to-back converter, the current controller designed for the GSC can be used to control the currents of the ESC. The control block depicted in Fig. 5.9 represents the control scheme sketched in Fig. 5.5, it contains an algorithm that samples the AC

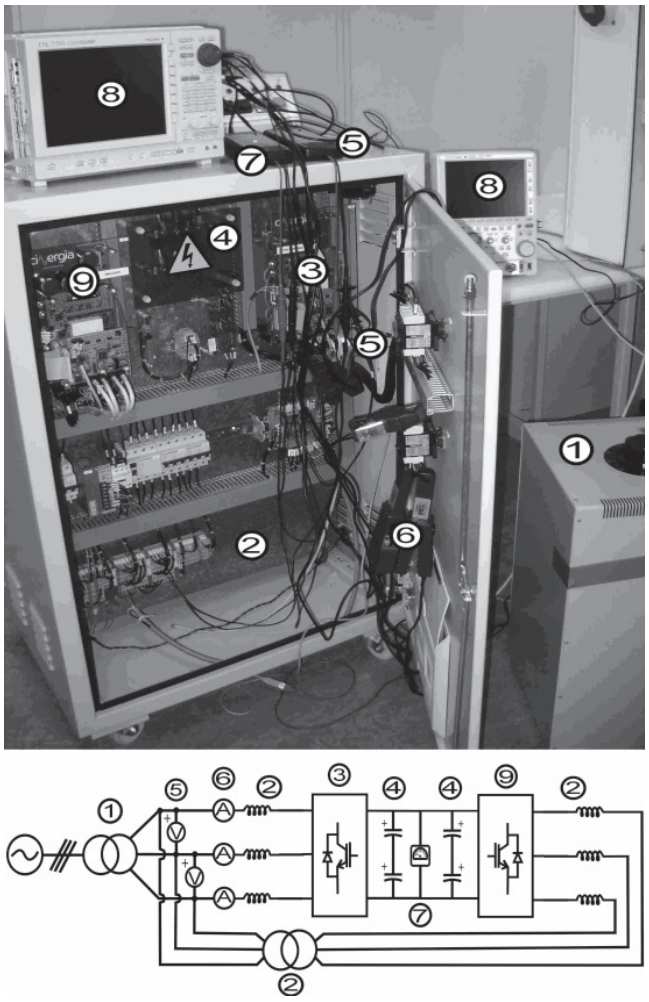

Figure 5.8: Schematic view of the experimental test bench: (1) Autotransformer, (2) Line inductances and isolation transformer (located behind), (3) Grid Side Converter, (4) Capacitor Bank, (5) AC Voltage measurement, (6) AC Current measurement, (7) DC Voltage measurement, (8) Data acquisition system, (9) Emulation Side Converter (ESC).

voltages V_{abc} and currents I_{abc} and the DC voltage E at the switching frequency. The implemented discrete PLL delivers the phase angle θ at each sample time in order to perform the Park transformation and compute the control actions in a $dq0$ frame. The PLL has been designed following the closed-loop synchronization based methodology given in [82].

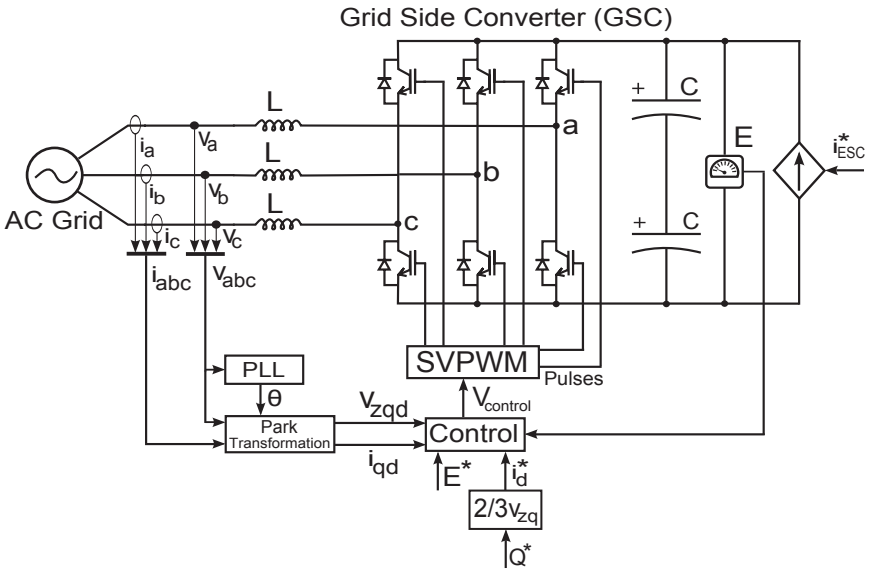

Figure 5.9: Schematic view of the control system implementation.

The outputs of the control block are the AC voltages $V_{control}$ used by the SVPWM module to generate the pulse sequence that drives the IGBT bridge. The control system maintains constant the DC voltage at its reference signal E^* while tracking the d-axis current reference signal i_d^* which is responsible for the generation of reactive power. On the ESC side the i_{ESC}^* current setpoints are used to manage the generation of real power.

To design the $\mathcal{H}_\infty$ controllers for this test bench the weights selected are $W_{ev} = 3$ and $W_{uv} = 1$ for the voltage controller and $W_{ec} = 250I_{2\times2}$ and $W_{uc} = 0.01I_{2\times2}$ for the current controller. A pole placement constraint was also included in the design process to ensure that the controller can be implemented with a sample frequency of 12 kHz. The pole placement region adopted was $\{s : |\mathrm{Im}(s)| < 1500 \text{ r/s } \& \ -1200 \text{ r/s} < \mathrm{Re}(s) < 0\}$. The discretization of the linear controllers is achieved by means of the Tustin transformation for a sample frequency of 12 kHz coincident with switching

frequency of the SVPWM algorithm. Under the conditions detailed above, the optimization process yields $\gamma = 0.2696$ for the current controller design and $\gamma = 1.6275$ for the voltage controller design. The fastest pole of the resulting voltage controller is -2240 r/s. This guarantees that the discretization has a small effect on the controller behavior. The resulting continuous time controllers are given in the Appendix.

Given that the closed-loop poles have been constraint to be ten times slower than the switching frequency, the inherent problems of physical implementation, such as computational time delay or aliasing effect, should not be affecting the performance of the system. The DSP provides a fixed-point architecture that works with IQ math for arithmetic operations. The comma selected (for a maximum of 32 bits) is IQ(19) which means that 19 bits are used to represent the decimal part of the values and 13 bit are used for the integer part. This choice provides enough resolution for representation of small variations while allowing the capture of a wide range of measurements.

5.5 Experimental Results

In this section, the results obtained experimentally in simulation are shown and compared. Since the design of the controller is based on the model of the system it is worth to compare both results, specially to validate the correctness of the assumptions made during the modeling and design process. For simulation purposes the ESC is modeled as a programmable DC current source connected to the DC link as depicted in Fig. 5.4. The dynamics of the converter are reduced to a first order system that provides the setpoints for the current source. This simplification is validated empirically by comparing the experimental results and the simulations resulting from the adoption of this assumption. The programmable DC current source that emulates the behavior of the ESC has been modeled with a time constant of 0.035 seconds. The model is developed under Matlab/Simulink© platform and the electrical subsystems have been implemented using the SimPowerSystems Toolbox.

Three different scenarios are presented in the next subsections in order to test the behavior of the system. In the first scenario only real power is being generated, this is done by setting the reactive power reference signal to zero of the GSC while commanding the current source to inject current into the DC-link. In this situation the GSC is forced to deliver real power in order to maintain the DC voltage stable, i.e. follow the reference signal E^*. In the second scenario the current source is not in use but a sequence

of reactive power reference signals (Q^*) is commanded to the GSC, in this case only reactive power will be delivered to the grid. In the third scenario, the former situations are mixed, i.e. real and reactive power are generated at the same time. In this last scenario the current source is injecting current into the DC-link while the GSC is commanded to deliver reactive power. The measurement points are indicated in Fig. 5.8 and the data plotted in this section have been passed through a low-pass filter of 1 kHz in order to eliminate the sensor noise.

5.5.1 Real Power Scenario

In this test the current source is providing current to the DC-link following the sequence of setpoints (i^*_{ESC}) plotted in Fig. 5.10b). In order to regulate the DC voltage, the GSC evacuates the excess of current into the AC grid, this current takes the form of real power since its phase is synchronized with the voltage phase. During the test no reactive current setpoint (i^*_d) is commanded, thus, no reactive power is generated. The total current generated is shown in Fig. 5.10 where it is plotted in the qd and abc reference frames and a comparison with simulation results is made. Due to the measurements noise, the i_q current of Fig. 5.10b) yields in a wide line, this signal has not been filtered in order to preserve the captured evolution of the signal. While the current reference signal i^*_{ESC} is composed of steps, the actual evolution of the current is imposed by the dynamics of the ESC. Since the poles of the current loop are very fast, the actual current i_{ESC} follows closely its reference signal i^*_{ESC}.

The DC-link voltage evolution is shown in Fig. 5.10c), where the effects of the current transients can be observed. The settling time of the DC voltage is related to the system dynamics and the performance of the K_v controller. Relaxed constraints for the voltage controller design where applied by means of selecting the proper W_{uv}, this fact leads to a smooth reaction when small variations in the DC voltage occur. Few volts of voltage error does not translate into an aggressive control action, i^*_q, as can be verified in the plot. It can be verified in this figure that the DC voltage ripple remains conveniently below 1% of the nominal voltage during all the test.

In Fig. 5.11a) a detailed view of the first current transient is shown in the abc reference frame. The waveforms depicted in Fig. 5.11b) correspond to one phase of voltages and currents, their synchronization clearly shows that only real power is being generated and no reactive power is provided by the converter during this test. The plot corresponds to the instant of maximum current generation, 3 A.

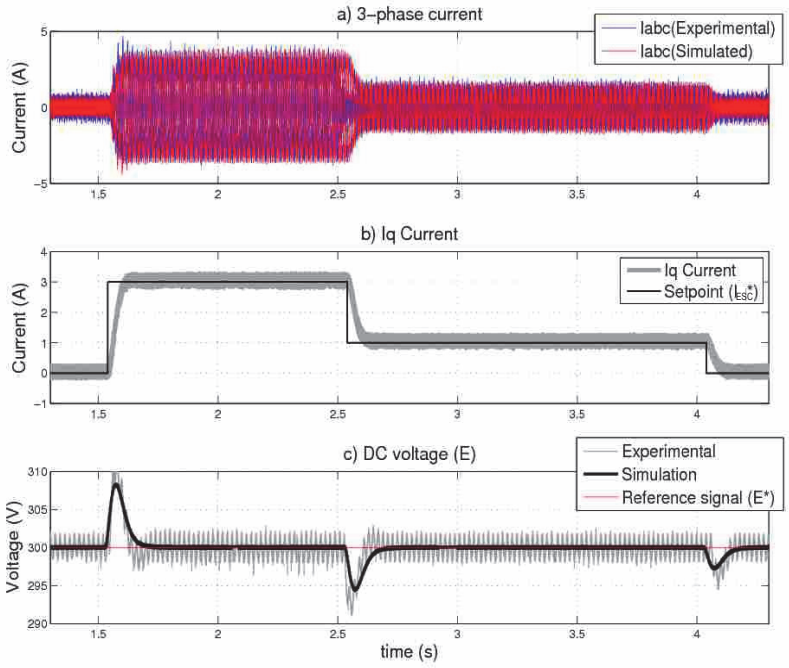

Figure 5.10: a) Three-phase current evacuated by the GSC. b) q-axis current (active current) in the gray line and DC current source setpoints (i^*_{ESC}) in black line. c) DC voltage at the capacitor bank. The black line corresponds to simulation results and the gray line to the experimental data, the red line indicates the reference signal.

5.5.2 Reactive Power Scenario

In this scenario, the current source is not operating and only reactive power is being delivered by the GSC. The reactive current setpoint sequence in the qd frame is plotted in Fig. 5.12b), the current evolution in the abc reference frame is shown as well in Fig. 5.12a). No delay in the response of the system can be observed in these plots since there is no current flowing through the DC-link and, thus, its dynamics are not affecting the results. During the test, only the current loop is acting, thus, the performance of the voltage

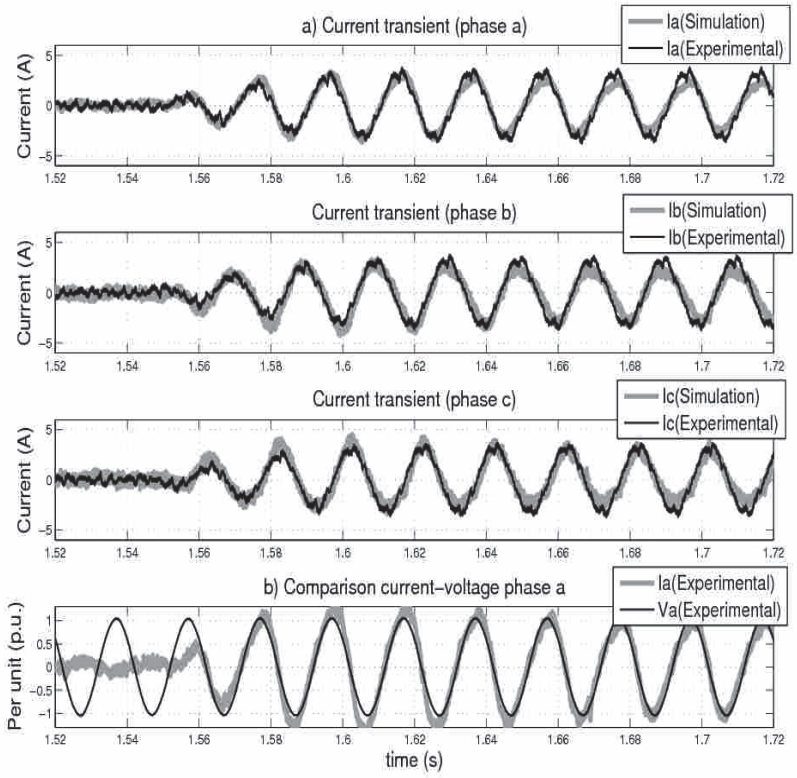

Figure 5.11: a) Detailed view of the current transient. b) A single phase of the grid voltage and current showing no phase lag corresponding to pure real power generation. The black line corresponds to the voltage and the gray line to the current.

controller is not reflected in the results, as a consequence the current has a fast response and follows its reference almost instantaneously. The DC-link voltage evolution is plotted in Fig. 5.12c) where small variations during current transients can be observed.

A detailed view of the current transient is provided in Fig. 5.13a). In order to generate reactive power the voltages and currents must have a 90° phase-lag between their phases, as can be seen in Fig. 5.13b). Until this

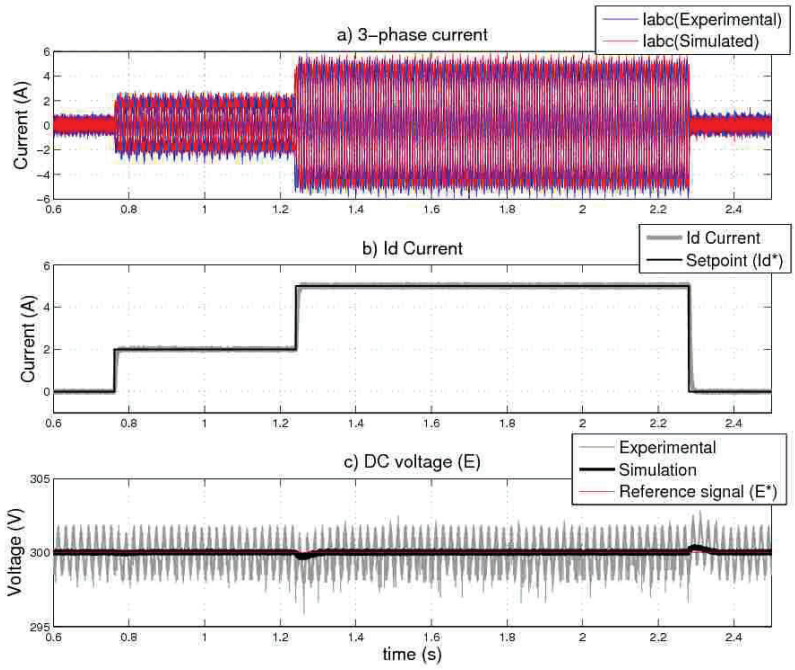

Figure 5.12: a) Three-phase current provided by the GSC. b) Reactive current in the *qd* reference frame, the black line corresponds to the GSC setpoint sequence and the gray line to the system response. c) DC-link voltages obtained from the experimental test and simulation. The black line corresponds to simulation results and the gray line to the experimental data, the red line indicates the reference signal imposed.

phase-lag is reached the current generated can affect partly the capacitor voltage, however, this influence is very small, less than 1 volt. The lack of slow dynamics provides a fast response of the system in this scenario.

5.5.3 Real and Reactive Power Scenario

In the last scenario the situations described in the previous subsections are happening at the same time, real and reactive power are generated simultaneously. The sequence of reactive current setpoints of the GSC (i_d^*) and

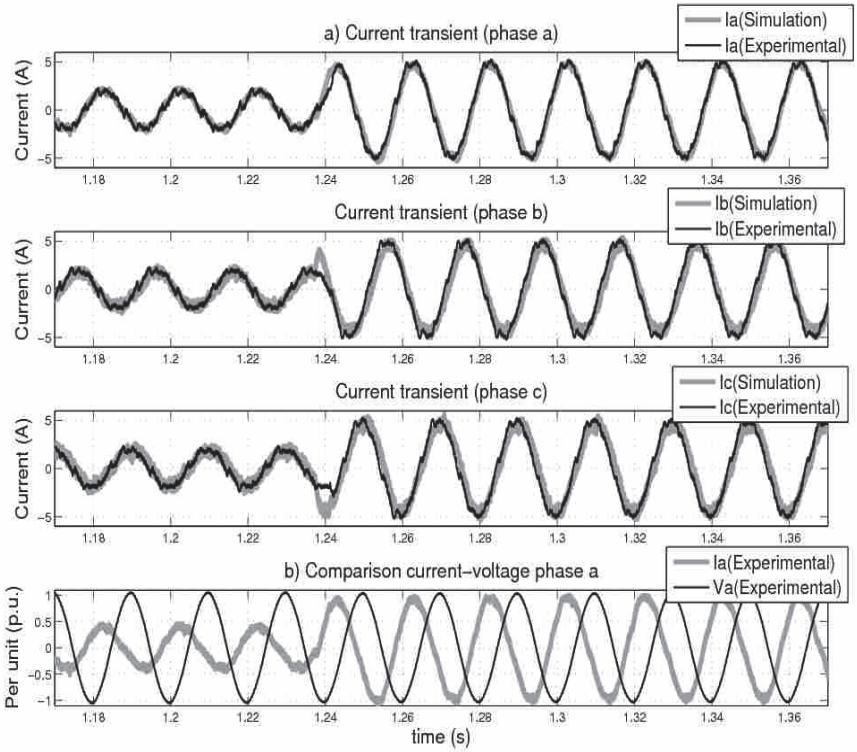

Figure 5.13: a) Detailed view of the current transient. b) Single phase of the grid voltage and current showing phase lag of 90° degrees corresponding to a pure reactive power generation. The black line corresponds to the voltage and the gray line to the current.

the sequence for the current source (i^*_{ESC}) are shown in Fig. 5.14b) and c) respectively. In this plot, it can be seen that the controls of the real (i_q) and reactive (i_d) currents are decoupled, thus, the transients of one of the currents does not cause a strong variation on the other one. The DC-link voltage evolution can be seen in Fig. 5.14d). The transients that can be noticed are due to the changes in real power generation while the transients corresponding to changes in reactive power generation are too small to be observed.

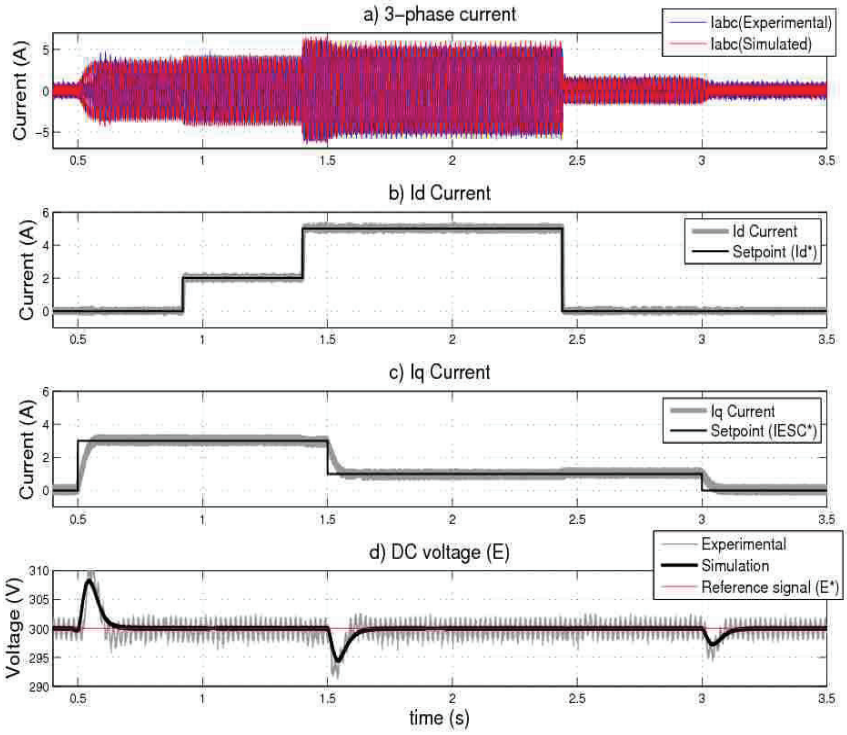

Figure 5.14: a) Three-phase current provided by the GSC. b) Reactive current measurement and setpoint in the *qd* reference frame. c) *q*-axis current (active current) in the gray line and DC current source setpoints (i^*_{ESC}) in black line. d) DC-link voltage. The black line corresponds to simulation results and the gray line to the experimental data, the red line indicates the reference signal.

A detailed view of the current transient is provided in Fig. 5.15a).The phase-lag between voltages and currents is plotted in Fig. 5.15b), these waveforms present a phase angle between 0° and 90° as corresponds to this scenario. This plot corresponds to reactive current generation of 5 A and real current generation of 1 A.

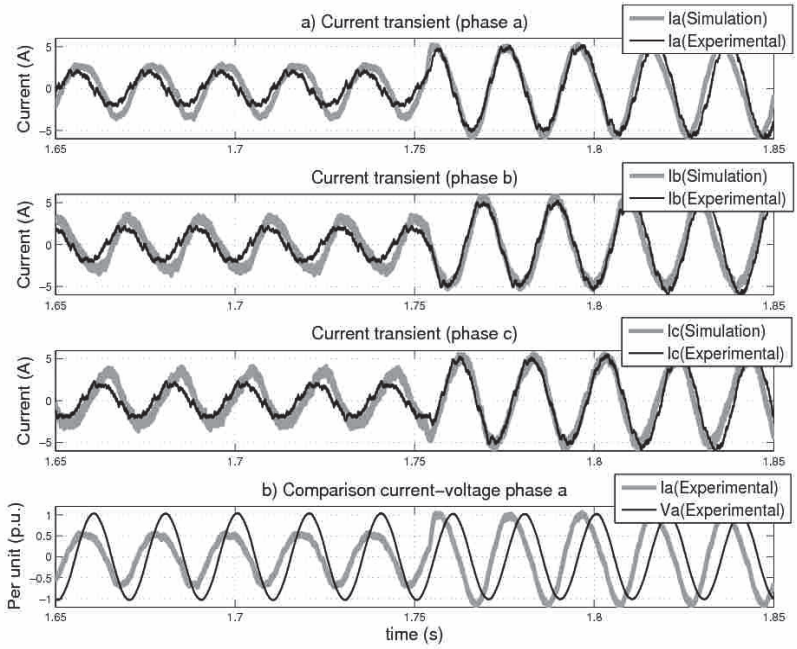

Figure 5.15: a) Detailed view of the current transient. b) Single phase of the grid voltage and current showing a phase lag between 0° and 90° degrees corresponding to a real and reactive power generation. The black line corresponds to the voltage and the gray line to the current.

5.6 Conclusion

A control strategy that includes optimal controllers and anti-windup compensation is proposed to manage the interchange of real and reactive power between a VSC and the AC grid. A special effort has been put on the implementation and test of these controllers in industrial equipment that has embedded a DSP as many commercially available converters have. The proposed control system can be implemented in processing units that have a lower performance than the DSP used in this work. It is also possible to implement the resultant controllers in a similar DSP together with more

complex algorithms to manage multi-level converters, reject negative sequence or compensate harmonic components without affecting the control system execution. The control scheme has been evaluated experimentally showing a satisfactory response and an accurate matching with the results predicted in simulation. The control system proposed in this work provides a good performance combined with low control efforts; nevertheless it does not increase excessively the order of the controllers. In consequence, an efficient implementation can be done which provides numerical stability to the control loops. The design stage of the control system and its implementation have been detailed and all the considerations taken into account have been explained providing a clear and easy to understand view of the entire process. The scenarios considered during the testing stage introduce a realistic background. These scenarios correspond to the actual situations that typically has to face a grid connected VSC in steady-state operation.

Controllers implemented

$$K_c(s) = \left[\begin{array}{cc|cccc} 0.000 & 0.000 & 128.000 & 0.000 & 0.000 & 0.000 \\ 0.000 & 0.000 & 0.000 & 128.000 & 0.000 & 0.000 \\ \hline -99.959 & -0.189 & 0.000 & 0.000 & 12.652 & -1.131 \\ 0.189 & -99.959 & 0.000 & 0.000 & 1.131 & 12.652 \end{array}\right]$$

$$K_v(s) = \left[\begin{array}{ccccc|c} -1487.7 & 102.7 & 1311.9 & 2214.0 & -2.7 & 0.000 \\ -507.4 & -1587.4 & -57.2 & 147.9 & 50.1 & 0.000 \\ 879.3 & 389.5 & -1682.0 & -2457.0 & -2.6 & 0.000 \\ 732.4 & 281.1 & -1280.4 & -1948.2 & -2.1 & 0.000 \\ 0.000 & 0.000 & 0.000 & 0.000 & 0.000 & 64.0 \\ \hline -7.5 & -49.6 & -3.5 & -0.6 & 1.5 & 0.000 \end{array}\right]$$

$$K_{AW}(s) = \left[\begin{array}{ccc|c} -1584.0 & -163.1 & 7.1 & -26.1 \\ 2390.9 & -4241.6 & 1.3 & 26.1 \\ -2.5 & 8.5 & -1399.8 & 0.000 \\ \hline 39.3 & 46.0 & -0.2 & 0.000 \\ -26.1 & -26.1 & 0.000 & 0.000 \end{array}\right],$$

6

Machine-Side Converter Control

In this chapter, an optimal control scheme is proposed for the back-to-back converter interfacing a PMSG in the context of wind turbines. The main objective of this control is to maximize the energy capture in low wind speeds, although is not limited only to this region since the control is also used to impose the rated torque in high wind speeds. The proposed design is intended to preserve the simplicity and numerical stability of classical approaches whereas takes advantage of formal systematic tools to produce a control system that ensures stability and performance in different operating condition. The result is a new gain-scheduled multi-variable PI controller based on LPV theory, which is able to adapt itself to the operating condition providing a uniform response under highly varying rotational speed and keeping the implementation as simple as classical controls commonly used in power converter applications [50, 51].

This chapter is organised as follows. In section 6.1 a general view of the control system of the Machine-Side Converter (MSC) and the basic concepts of the control theory used to develope the proposed controller are given. In Section 6.2 the system description is given. In Section 6.3 the control system design is discussed and in Section 6.4 simulation results are provided. In Section 6.5 the experimental setup is described and experimental results are shown. Section 6.6 shows a comparison between the performance of a traditional PI and the proposed control system and, in Section 6.7, the conclusions of this work are summarized.

6.1 Introduction

The control system of the MSC tracks the torque setpoints computed by the speed controller by regulating the currents that circulate through the stator of the generator. The conversion from torque setpoints to current setpoints is straightforward since these two signals are proportional. By using the Park transformation the currents can be expressed in the qd axis that are linked to the active and reactive power respectively. The active current is related to the electromagnetic torque, its setpoint is imposed by the speed controller, however, the reactive current can be freely selected by the user within the operational limits of the converter. Depending on the application and the type of generator some amount of reactive power may be necessary. The generic control system for this side of the converter consists only in the current loop as shown in Fig. 6.1.

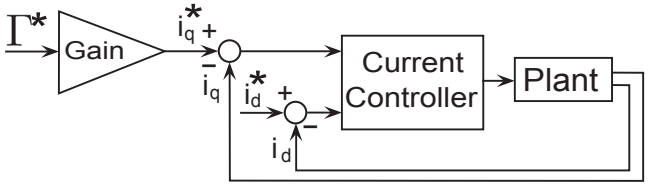

Figure 6.1: Generic block diagram of the control strategy

This control system interacts with a rotational machine which provides a variable frequency when the rotational speed changes. Traditionally, PI controllers have been used for this application. A PI is a well known control structure and the addition of decoupling terms provide some adaptation to the different operating points of the system. On the other hand, the approach proposed in this work aims to design a multi-variable LPV control that ensures stability and performance in the entire range of operation. A schematic view of the LPV system using $\theta(t)$ as a generic scheduling variable, is sketched in Fig. 6.2. In the formulation of this problem it is assumed that the parameter time variations have bounded magnitude and rate.

The parameter-dependent system matrices in a generic form are expressed as

$$\begin{aligned} \dot{x} &= A(\theta(t))x + B(\theta(t))u \\ y &= C(\theta(t))x \end{aligned} \tag{6.1}$$

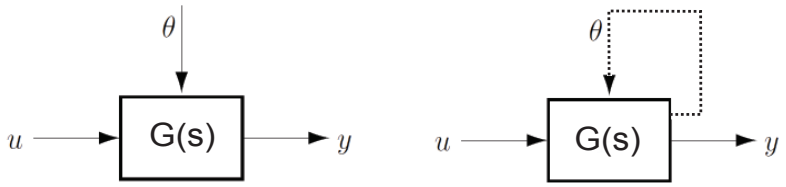

Figure 6.2: Schematic view of the LPV system with exogenous (left) and endogenous (right) scheduling variable.

with a state-space realization of the LPV augmented plant given by

$$\begin{bmatrix} \dot{x}(t) \\ z(t) \\ y(t) \end{bmatrix} = \begin{bmatrix} A(\theta(t)) & B_w(\theta(t)) & B_u \\ C_z(\theta(t)) & D_{zw}(\theta(t)) & D_{zu} \\ C_y & D_{yw} & 0 \end{bmatrix} \cdot \begin{bmatrix} x(t) \\ w(t) \\ u(t) \end{bmatrix} \tag{6.2}$$

and the resulting LPV controller is described as

$$\begin{bmatrix} \dot{x}_k(t) \\ u(t) \end{bmatrix} = \begin{bmatrix} A_k(\theta(t)) & B_k(\theta(t)) \\ C_k(\theta(t)) & D_k(\theta(t)) \end{bmatrix} \cdot \begin{bmatrix} x_k(t) \\ y(t) \end{bmatrix} \tag{6.3}$$

In the case of controlling a generator the rotational speed (ω_g) can be used as the scheduling variable $\theta(t)$. During the design of the LPV controller an augmented plant, including the output z and the weighting functions, is defined in a similar way to the $\mathcal{H}_\infty$ optimal control procedure explained previously (Fig. 5.3). Once the problem is formulated the controller can be synthesized by solving a convex optimization problem as described in [52]. The aim of this procedure is to find a sub-optimal solution by mapping from the disturbance signal to the output while respecting the constraints imposed.

6.2 System description

The power extracted by the wind turbine from the kinetic energy of the wind can be expressed as

$$P_w = \frac{\rho \pi R^2}{2} C_P(\omega_t R / v_w, \theta_{pitch}) v_w^3, \tag{6.4}$$

where C_P is the power coefficient, ρ is the air density, R is radius of the rotor, ω_t is the rotational speed, v_w is the wind speed and θ_{pitch} is the pitch angle. The mechanical torque developed by the turbine is then computed

as $\Gamma_t = P_w/\omega_t$. A simple one-mass model is used to describe the shaft. Between the turbine and the generator there is a gearbox, considered ideal (no power losses), which increases the rotational speed and decreases the torque as

$$\omega_g = \eta\omega_t, \quad \Gamma_t = \eta\Gamma_{load}, \tag{6.5}$$

where η is the gear ratio and ω_g and Γ_{load} are the rotational speed and mechanical torque of the generator respectively. The mechanical torque is counterbalanced by the electrical torque Γ_g applied by the generator, this interaction affects the rotational speed according to the dynamic equation

$$(\Gamma_{load} - \Gamma_g)\frac{1}{J} = \dot{\omega}_g, \tag{6.6}$$

where J is the inertia of the system including turbine, gearbox and generator.

The speed developed by the wind rotor is controlled by the pitch angle θ_{pitch} and the electrical torque Γ_g which are computed with the aim of regulating the rotational speed. Normally, in high wind speeds, the pitch controller maintains the rotational speed at the rated value while the torque reference signal is constant. In low wind speeds, the pitch controller is not active and the rotational speed is controlled by the electrical torque to maximise the energy capture. To this end, the torque setpoint,

$$\Gamma^* = k_t\omega_g^2, \tag{6.7}$$

where k_t is a constant gain [83], is sent to the converter. This ensures that the C_P remains close to the optimal value and thus maximising the energy capture. The mechanical speed ω_g is related to the electrical frequency ω_e according to $\omega_e = p \cdot \omega_g$, where p is the number of pole pairs.

The PMSG interacts with the AC grid through a fully-rated back-to-back converter. This converter can be directly connected to the grid or it can incorporate a power transformer to adapt the output voltages. In Fig. 6.3 a schematic view of the complete system is sketched.

The Machine Side Converter (MSC) is the side of the back-to-back converter connected to the generator. The MSC provides reactive current to the generator (if needed) and also regulates the active current that flows through the stator generating the electromagnetic torque. The dynamics of the MSC in the synchronous reference resulting from the Park transformation is governed by

$$\dot{x} = \begin{bmatrix} -R/L & \omega_e \\ -\omega_e & -R/L \end{bmatrix} x + \begin{bmatrix} -1/L & 0 \\ 0 & -1/L \end{bmatrix} (v_l + v_g), \tag{6.8}$$

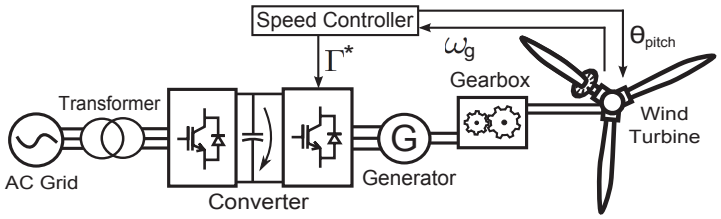

Figure 6.3: Schematic view of a wind power generation system.

where

$$x = \begin{bmatrix} i_{gq} \\ i_{gd} \end{bmatrix}, \quad v_l = \begin{bmatrix} v_{lq} \\ v_{ld} \end{bmatrix}, \quad v_g = \begin{bmatrix} v_{gq} \\ v_{gd} \end{bmatrix},$$

i_{gq} and i_{gd} are the generator qd currents, v_{lq} and v_{ld} are the converter qd voltages (control signals) and v_{gq} and v_{gd} are the generator qd voltages. The resistance R and the inductance L result from

$$R = R_c + R_g, \qquad L = L_c + L_g,$$

where the subscripts indicate c for converter and g for generator. The components R_c and L_c refer to the resistance and inductance of the filter between the converter and the generator. The torque applied by the generator is given by

$$\Gamma = \frac{3}{2} p \Psi i_{gq}, \tag{6.9}$$

where Ψ is the permanent magnet flux linkage of the generator. The reactive power, related to the current i_{gd}, is expressed as

$$Q_g = \frac{3}{2} v_{gq} i_{gd}, \tag{6.10}$$

which can be useful for field weakening applications [84]. The generator under consideration has surface-mounted magnets and is described assuming the same inductance in the d and q axis (i.e. $L = L_q = L_d$), such assumption provides a good approximation for control design purposes.

The Grid Side Converter (GSC) is the side of the back-to-back converter connected to the grid. The GSC has to evacuate the power generated in the form required by the grid code, it has also to maintain the voltage stable at the DC-link between both sides. The dynamics of the GSC is governed by

$$\dot{x} = \begin{bmatrix} -R_z/L_z & \omega_z \\ -\omega_z & -R_z/L_z \end{bmatrix} x + \begin{bmatrix} -1/L_z & 0 \\ 0 & -1/L_z \end{bmatrix} (v_l + v_z), \tag{6.11}$$

where

$$x = \begin{bmatrix} i_{zq} \\ i_{zd} \end{bmatrix}, \quad v_x = \begin{bmatrix} v_{xq} \\ v_{xd} \end{bmatrix}, \quad v_z = \begin{bmatrix} v_{zq} \\ v_{zd} \end{bmatrix},$$

where v_x are the converter voltages, v_z refers to the grid voltages, i_{zq} and i_{zd} are the grid currents and ω_z is the electrical frequency of the grid. The grid-side converter includes a filter which parameters are the resistance R_z and the inductance L_z. The DC-link connecting both sides of the back-to-back converter provides an additional differential equation associated to the capacitor bank, its voltage is governed by

$$\frac{d\nu}{dt} = \frac{2}{C}\left(\frac{3}{2}v_{gq}i_{gq} - \frac{3}{2}v_{zq}i_{zq}\right), \tag{6.12}$$

where ν is the square of the DC voltage ($\nu = E^2$) and C is the capacitance. The variable ν is used to compute the DC voltage behavior instead of E (actual voltage level) in order to linearise the system [78, 85]. Being the Park transformation oriented to v_{zq} ($v_{zd} = 0$), the real and reactive power delivered by the GSC in the qd frame are given by

$$P_z = \frac{3}{2}v_{zq}i_{zq}, \qquad Q_z = \frac{3}{2}v_{zq}i_{zd}.$$

6.3 Control strategy

The control of both converters can be designed independently although both systems are connected through the DC voltage. In the grid side the GSC evacuates the energy produced by regulating the DC voltage. In the machine side the torque setpoints are computed by the high-level controller (or speed controller) based on the rotational speed and then sent to the LPV low-level controller (or current controller). The control of the MSC aims to track the electrical torque reference signal Γ^* by controlling the generator voltages or equivalently the currents i_{gqd}. Once Γ^* is computed, the low-level control can easily calculate the q-axis current setpoint i^*_{gq} using (6.9). The d-axis setpoint i^*_{gd} can be set arbitrarily (within the generator operational limits) if field weakening actions are required [84]. The focus of the proposed strategy is on the electrical aspects of the control, details about the blade pitch angle control can be found in [86].

6.3.1 LPV Control for the MSC

It is clear from (6.8) that the dynamic behavior of the system depends on the particular generator angular velocity ω_g. In fact, the state space model (6.8)

depends affinely on the exogenous variable ω_g and can be expressed as a Linear Parameter-Varying (LPV) system of the form

$$G(\omega_g) : \begin{cases} \dot{x} = A(\omega_g)x + Bv_l + Bv_g, \\ y = x, \end{cases} \tag{6.13}$$

where

$$A(\omega_g) = \begin{bmatrix} -R/L & 0 \\ 0 & -R/L \end{bmatrix} + \omega_g \begin{bmatrix} 0 & p \\ -p & 0 \end{bmatrix},$$
$$B = \begin{bmatrix} -1/L & 0 \\ 0 & -1/L \end{bmatrix},$$

and ω_g is in the set $\Omega = \{\omega_g : \omega_{\min} \leq \omega_g \leq \omega_{\max}\}$ with $\omega_{\max}$ and $\omega_{\min}$ the maximum and minimum rotational speeds.

The controller must ensure stability and performance for all possible angular velocities in Ω. For this reason, when using traditional controllers, decoupling terms are commonly added to eliminate the dependency on ω_g. Although this simplifies the controller design, it may not be able to fully exploit all the degree-of-freedoms in the problem and the resulting controller is not robust against uncertainty in the model parameter. On the other hand, the synthesis procedure proposed by Apkarian, et al. [52] allows to design of robust multi-variable LPV gain scheduled control that is able to ensure stability and performance for all time-varying parameters ω_g in the set Ω. This control scheme, using the rotational speed ω_g as the exogenous scheduling variable, is sketched in Fig. 6.4.

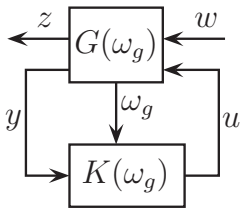

Figure 6.4: Schematic view of the LPV gain-scheduled control strategy.

LPV gain scheduling design resembles the $\mathcal{H}_\infty$ optimal control procedures. The objective is to find an LPV control $K(\omega_g)$ that minimises the induced norm of the operator mapping the disturbance w into the performance output z, that is

$$\min_{K(\omega_g), w \neq 0} \frac{\|z\|_2}{\|w\|_2} < \gamma, \quad \forall \omega_g \in \Omega \tag{6.14}$$

where $\|x\|_2 = \sqrt{\int_0^t x^T x \; dt}$ and $\gamma > 0$. The performance specifications are considered in the design procedure with an adequate selection of the performance output z and by adding weighting functions. These functions filter the performance signal penalising certain frequencies of interest. The gain-scheduled controller satisfying (6.14) is computed by solving a convex optimization procedure [52]. It is not the intention of this work to detail the mathematical solution for this problem since software capable of solving it efficiently is available.

Similarly to $\mathcal{H}_\infty$ optimal control, the design begins with the definition of augmented plant where the performance output z and the weighting functions are stated. In the case of MSC, the augmented plant is shown in Fig. 6.5, in which the objective is to track a current reference i^*_{gqd}. The weighting function W_{uc} penalises the high frequency components of the control action and W_{ec} weights the low frequencies of the current errors, with the aim of finding a trade-off between tracking error and an reasonable control input. The weight W_{uc} also limits the controller bandwidth improving the robustness of the system against modelling errors. It is desirable to include integral action to ensure a zero steady-state error. This cannot be achieved by including an integrator in the weighting function W_{ec} because it would include an unstable and uncontrollable pole and the augmented plant would not be stabilizable, instead, the integrator is placed as shown in Fig. 6.5.

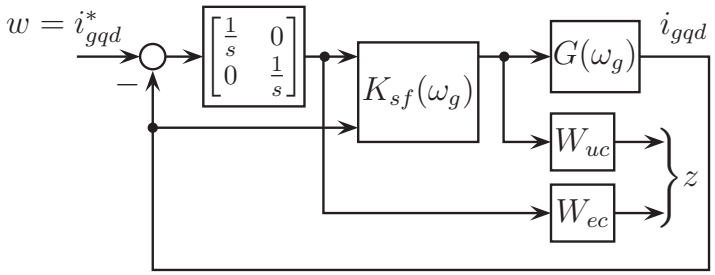

Figure 6.5: Setup for the controller design of the MSC.

Since the states of the system (6.8) and the integral action are available to be used by the controller, if the weighting functions are constant, the control design can be expressed as state feedback problem. As a consequence, the complete controller results in a multi-variable PI structure. That is, once the state feedback gain K_{sf} (a 2×4 matrix) is obtained, the control law for

the current loop is given by

$$v_{lqd} = K_{sfi}(\omega_g) \int_0^t (i^*_{gqd} - i_{gqd})dt + K_{sfp}(\omega_g) i_{gqd}, \tag{6.15}$$

where the subindex qd denotes the q and d components of the variable and K_{sfi} and K_{sfp} ($K_{sf} = [K_{sfi}\ K_{sfp}]$) correspond to the integral and proportional gains of the controller respectively. This is a common control structure used in power converter, but the approach in (6.15) do not need decoupling terms to design two independent PI controllers. In fact, the PI structure (6.15) exploits the coupling between variables besides considering the time-varying nature of the system with the aim of achieving better performance and robustness. This leads to a low order controller that provides numerical stability, less computational cost and an efficient implementation.

The constraint (6.14) can be complemented with additional restrictions on the closed-loop poles location [79]. This is particularly useful to make possible the implementation of the controller in discrete time. Given the limitations that, in general, have the industrial equipments in terms of amount of memory and computing speed, the state feedback structure proposed facilitates the controller application.

Owing to the affine dependency of the LPV system (6.13) on the generator angular velocity ω_g, the controller interpolation to construct the gain-scheduled controller reduces to a linear combination of two matrices, i.e., the controller parameter for the current angular velocity ω_g is given by

$$K_{sf}(\omega_g) = (1 - \alpha(\omega_g))K_{sf1} + \alpha(\omega_g)K_{sf2}, \tag{6.16}$$

where $0 \leq \alpha \leq 1$ and is obtained from

$$\alpha(\omega_g) = \frac{\omega_g - \omega_{\min}}{\omega_{\max} - \omega_{\min}}$$

The constant matrices K_{sf1} and K_{sf2} are produced by the optimisation procedure. A brief explanation about the optimisation procedure can be found in the Appendix of this chapter.

6.3.2 $\mathcal{H}_\infty$ Control for the GSC

The GSC regulates the DC voltage and delivers the amount of reactive current demanded by the grid operator. To this end, a control scheme with a two-loop structure is used, the inner loop corresponds to the current control and the outer loop to the voltage regulation. The control scheme is shown

in Fig. 6.6 where the voltage controller K_v, the current controller K_i and the anti-windup compensator K_{AW} are depicted. The inclusion of the feed-forward term v_{zqd} enhances rejection of input voltages disturbances and also improves the dynamic responses in the voltage control loop based on the fact that the loop gain becomes independent of the input voltage [80]. Unlike the MSC case, the dynamic of the system does not depend on the angular velocity and a time-invariant controller designed by $\mathcal{H}_\infty$ optimal control is sufficient to achieve an adequate performance. Further details on the design and implementation of this controller can be found in [85, 78] and in **Chapter 5**.

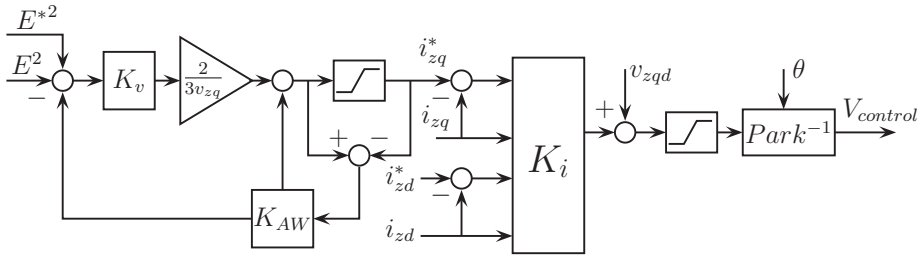

Figure 6.6: Control scheme for the GSC.

6.4 Simulation Results

The control strategy was first evaluated by simulation in the case of a 5 MW wind turbine based on PMSG technology. The wind turbine model is described in detail in [87] and the generator in [88], a list with the most relevant parameters of the system can be found in Table 6.4. Although the main focus of this work is on the power converter, this first simulation is intended to show the conditions in which the power converter controlling the PMSG should work.

Notice that this model combined a gearbox and a PMSG, this atypical configuration was based on the models developed in [88]. This configuration was selected because it provided a high-speed shaft and a low number of pole pairs in the generator, such characteristics can also be found in the experimental setup described in Section 6.5.

The torque reference for speed control was computed as (6.7) with $k_t = 3.6\ \mathrm{Nm(r/s)^{-2}}$. Average models were considered for the power converters

Table 6.1: Model parameters of the 5 MW wind turbine used in simulation

Radius (R)	61.5 m
Air density (ρ)	1.225 Kg/m^3
Gear ratio (η)	97
High-speed side Inertia (J)	4119.4 Kgm^2
Pole pairs (p)	25
Generator frequency	500 Hz
Magnet flux linkage (Ψ)	1.0998 Wb
Resistance (R)	0.3192 Ω
Inductance (L)	0.0012 H
DC-link Capacitance (C)	3000 μF

and the AC grid was modelled as an infinite bus. For the MSC control design, the weighting function selected were the constant gains

$$W_{uc} = 0.1 I_{2\times 2}, \qquad\qquad W_{ec} = 24 I_{2\times 2},$$

where $I_{2\times 2}$ is the identity matrix of 2×2. A pole placement constraint was also included in the design process, the region adopted was $\{s : |\mathrm{Im}(s)| < 2000$ r/s and -2000 r/s $< \mathrm{Re}(s) < 0\}$. The scheduling variable was assumed ranging from 400 to 1250 rpm.

The current controller of the GSC was designed using the same weights previously stated for the MSC. For the design of the outer DC voltage controller the weighting functions implemented were

$$W_{uc} = \frac{0.01592s + 0.1}{0.001592s + 1}, \qquad\qquad W_{ec} = 3,$$

and the same pole placement region was adopted.

Fig. 6.7 presents the singular values of the open loop and closed loop systems of the MSC at three different rotational speed. The plots correspond to the transfer function mapping the references i^*_{gqd} into the currents i_{gqd}. It can be observed that the open loop responses present changes in the frequency and damping of the eigenvalues. In the bottom plot, it can be seen the effect on the frequency response of the closed loop system with the proposed control. The LPV controller produced more uniform responses for the three values of angular velocity.

In order to provide a realistic application of the proposed control system, the wind speed profile depicted in Fig. 6.8a was used as input for the simulation. The wind speed ranges from 6 m/s to almost 11 m/s. The pitch

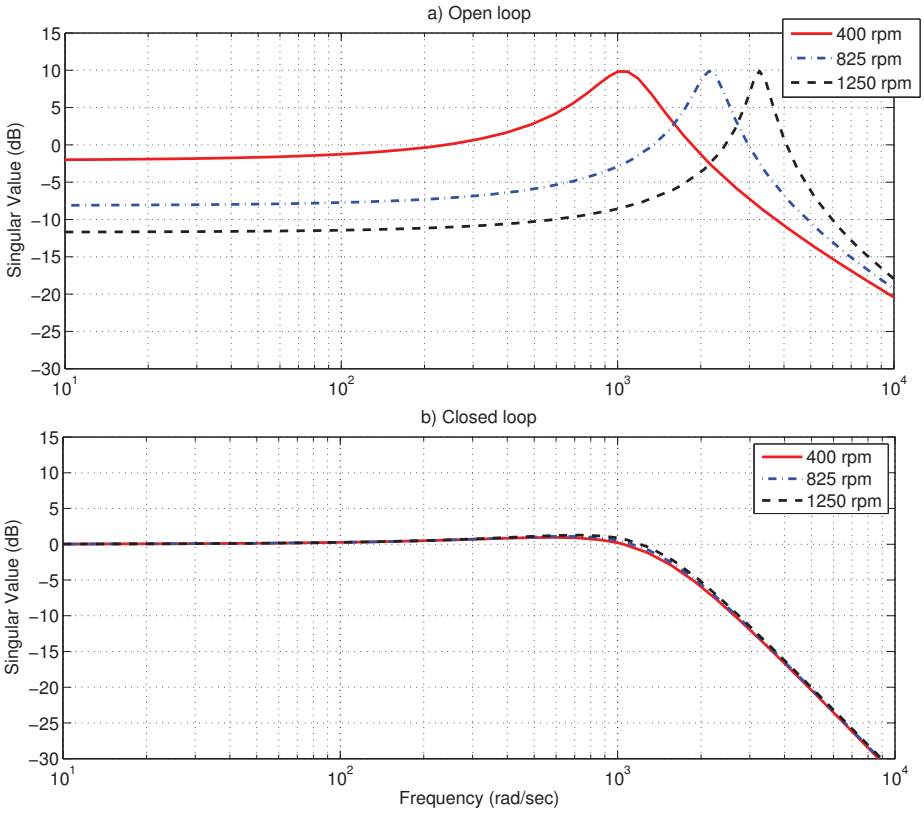

Figure 6.7: Maximum singular values of the transfer function corresponding to $\omega_g = \{400, 825, 1250 \text{ rpm}\}$ for the 5 MW PMSG wind turbine case.

control is not active since the rotational speed never reaches the rated value. The C_P value (black line) is kept close to its optimal value (grey line) in normal operation as shown in Fig. 6.8b. The generator speed depicted in Fig. 6.8c shows a range going from 900 rpm up to 1100 rpm, the inertia of the system acts as a low-pass filter that smooths the effects of the wind speed variations on the rotational speed. In Fig. 6.8d the electrical power is plotted, it is always below the rated value 5 MW since the wind turbine never reaches the rated value. The generator currents are plotted in Fig. 6.8e in black lines, they follow their reference signals (marked as grey lines) which

depend on the generator speed in the case of the q-axis setpoint and in the case of the d-axis setpoint is set to zero. The enlarged view corresponding to the dashed line box is provided in Fig. 6.8f where a slight deviation of the current respect to the setpoint can be observed. The load torque developed by the wind turbine is plotted in red line in Fig. 6.8g, the generator torque follows its reference signals which depends on the rotational speed according to (6.7). The difference between the load torque and the generator is due to the effect of the inertia of the system and results in the deviations observed in the C_P value. The generator voltages applied by the MSC are depicted in Fig. 6.8h, these voltages in the qd reference frame are the control action computed by the LPV controller. These simulations show the high variability of the rotational speed in a variable-speed wind turbine.

6.5 Experimental Results

The proposed control scheme was implemented in the experimental setup shown in Fig. 6.9 which is described in detail in **Chapter 3**. The setup emulated a wind energy conversion system where the rotor and gearbox are substituted by an induction motor, this motor developed the load torque that is applied to the generator through a high-speed shaft. The motor speed was controlled by a commercial motor drive connected to the grid. The electrical subsystem is composed by the PMSG, the fully-rated back-to-back converter and the transformer. The converter consisted of two IGBT-based Voltage Source Converter (VSC) connected through a DC-link as shown in Fig. 6.10.

Notice that the high-level speed controller was not implemented due to the fact that the available equipment is not capable of reproducing the aerodynamic behavior of the wind turbine. As a consequence, the scenario presented in the previous section cannot be evaluated experimentally. In order to provide a clear view of the control system behavior a different approach is used in the experimental tests. In this case, step changes are implemented as torque reference signals unlike the reference signals derived from the speed controller used in the simulation model that are smoothed by the inertia of the turbine. Taking into account that the time constant of the mechanical subsystem is generally much larger than the electrical time constant, this choice can be considered appropriate to evaluate the electrical aspects of the problem under analysis.

The low-level control blocks depicted in Fig. 6.10 represent the controllers obtained from Fig. 6.5 (MSC) and the control scheme sketched in Fig. 6.6 (GSC). They also contain an algorithm that samples the AC voltages v_{abc},

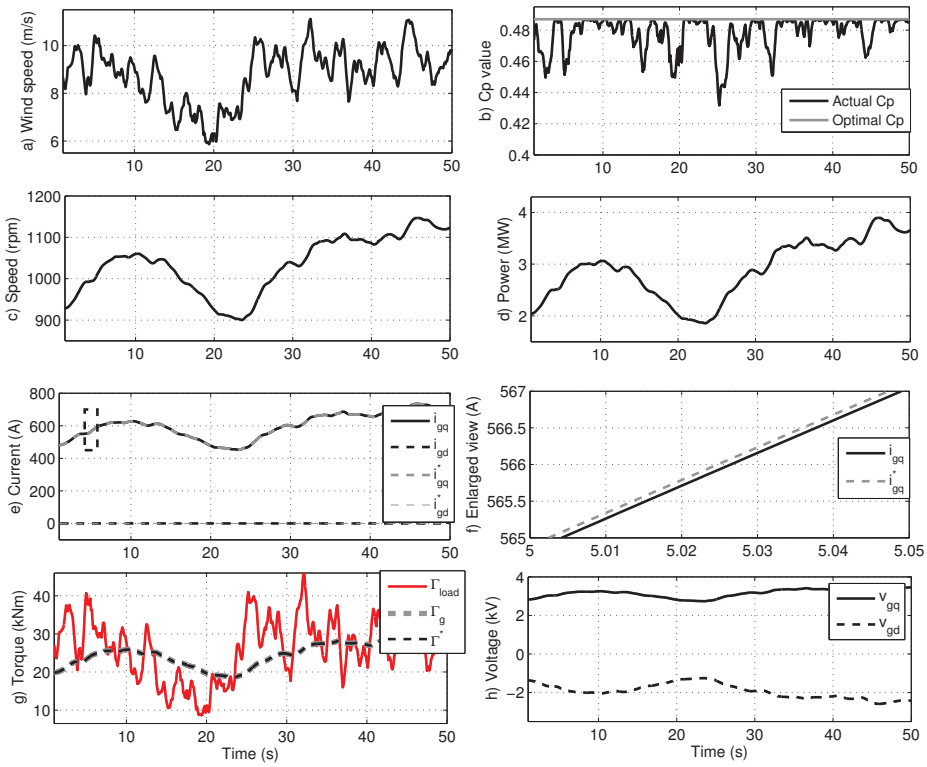

Figure 6.8: Response corresponding to a realistic wind speed profile for the 5 MW PMSG-based wind turbine. a) Wind speed profile, b) actual C_P value (black line) and optimal C_P (grey line), c) generator mechanical speed, d) electrical power delivered, e) generator currents (black lines) and their reference signals (grey lines) in the synchronous reference frame, f) enlarged view of the q-axis current and its reference signal, g) load torque developed by the turbine, generator torque and torque reference signal provided by the speed controller and h) generator qd voltages applied by the LPV controller.

the currents i_{ab}, the DC voltage E, and the generator speed ω_g at the switching frequency. The implemented discrete Phase-Locked Loop (PLL) delivers the phase angle θ at each sample time in order to perform the Park transfor-

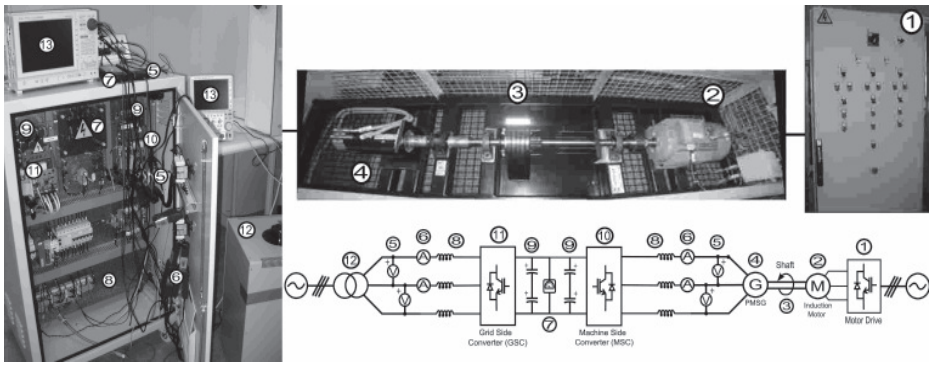

Figure 6.9: Experimental test bench: (1) motor drive, (2) induction motor, (3) axis with inertial discs, (4) permanent magnet synchronous generator, (5) ac voltage measurements, (6) ac current measurements, (7) dc voltage measurement, (8) line inductances (located behind), (9) capacitor bank, (10) machine side converter, (11) grid side converter, (12) transformer.

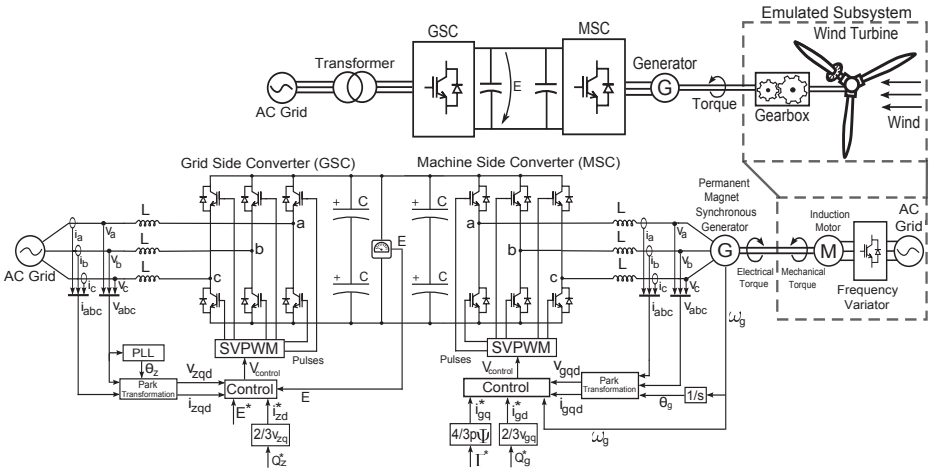

Figure 6.10: Schematic view of the experimental setup emulating a wind turbine based on PMSG.

mation and compute the control actions in a dq frame. The PLL has been designed following the closed-loop synchronization based methodology given in [82].

For the design of the LPV gain scheduling controller described in Section 6.3, the weighting functions were $W_{ec} = 0.4 \cdot I_{2\times2}$ and $W_{uc} = 0.1 \cdot I_{2\times2}$ and the pole placement region adopted was $\{s : |\mathrm{Im}(s)| < 1500 \text{ rad/s and } -2000 \text{ rad/s} < \mathrm{Re}(s) < 0\}$. It was assumed that the angular velocity ranges from $\omega_{min} = 62.8$ rad/s to $\omega_{max} = 502.6$ rad/s (200 rpm and 1600 rpm respectively in mechanical speed). The integrator in (6.15) was discretised with the Tustin transformation for a sample frequency of 12 kHz coincident with switching frequency of the Space-Vector Pulse Width Modulation (SVPWM) algorithm. This parameter selection yielded a closed loop system with a rise time of $t_r = 10$ ms.

Although the power level is considerably lower than in the simulation model, the previously described test bench permits to evaluate the control in similar speed conditions to those presented in simulation. Both systems have similar rated speeds being 1200 rpm for the multi-MW model obtained from the UpWind project [88] and 1500 rpm in the case of the test bench, they also present correlation in the torque/inertia ratio being 10.46 rad/s^2 and 12.29 rad/s^2 respectively. A test bench simulation using the speed profile shown in Fig 6.8c is plotted in Fig 6.11 in order to facilitate a comparison between both systems. The speed control (6.7) with $k_t = 4.25{\cdot}10^{-4}\ Nm(r/s)^{-2}$ is used to compute the torque reference signal.

6.5.1 Results

In order to provide fast electrical transients, torque reference signal Γ^* step changes were applied. Torque setpoints are directly translated into current setpoints i^*_{gq} according to (6.9) to facilitate the interpretation of the results. The performance of the proposed control scheme was evaluated in two scenarios. Firstly, the step response was analysed at three different rotational speeds, due to the inertia of the system the generator speed remains almost constant during these tests. In the second scenario a speed ramp was imposed to the system. In this parameter varying scenario the sequence of torque setpoint steps used in the first scenario was commanded as well. Although the focus of these tests is on the generator performance, electrical variables of the complete test bench were also captured in the first scenario. During the experiments the d-axis current setpoint i^*_{gd} is set to zero since field weakening strategies were not the purpose of these tests.

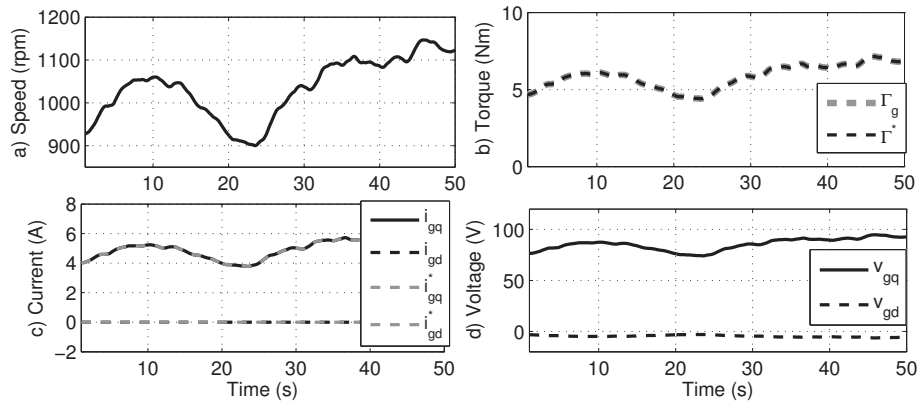

Figure 6.11: Response corresponding to the test bench model using the 5MW speed profile. a) generator mechanical speed, b) generator torque and torque reference signal provided by the speed controller, c) generator currents (black lines) and their reference signals (grey lines) in the synchronous reference frame, and d) generator qd voltages applied by the LPV controller.

Constant Speed Scenario

In this test, torque step reference signals were applied while the generator is rotating at a constant speed, the results are plotted in Fig. 6.12.

The speed control was done by the commercial motor drive acting on the induction motor emulating the wind rotor and it did not model the behavior of the wind rotor. The rotational speeds imposed by the motor were: 500, 1000 and 1500 rpm. Electrical transients are fast in comparison with mechanical changes, in consequence, variations in the mechanical speed are barely noticeable as can be checked in Fig. 6.12a. The sequence of current setpoints commanded during these tests is plotted in Fig. 6.12b in black solid line. The resulting q-axis currents at the three generator speeds are also shown in this plot. As can be observed, the same responses were obtained independently of the operating point of the system. The system performance at different speeds remains unaltered because the LPV controller is adapting itself to the operating conditions (using the rotational speed as scheduling variable) in order to provide the response shaped in the design stage. The control actions computed by the control system are the voltages in the synchronous reference frame, v_{gq} and v_{gd}, shown in Fig. 6.12c

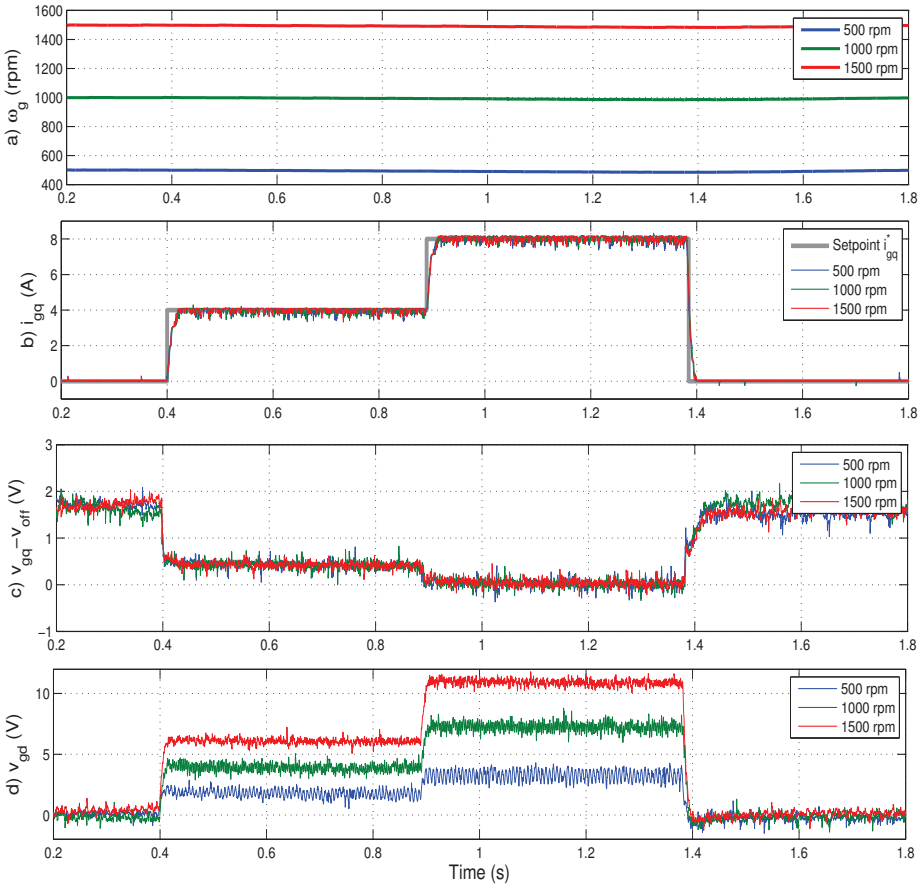

Figure 6.12: Experimental results corresponding to the constant speed scenario. a) Generator mechanical speed corresponding to the three tests (scheduling variable), b) current reference signal sequence and q-axis measured currents (LPV controller inputs), c) generator q-axis voltage (control action) with offset ($v_{gq} - v_{off}$) with v_{off}=40, 80 and 120 V corresponding to the generator speed ω_g=500, 1000 and 1500 rpm respectively and d) generator d-axis voltage (control action).

and 6.12d respectively. Similar control actions can be observed at the different operating points, the generator voltages increase or decrease according to the rotational speed and the current demanded but the evolution of these variables is barely changed in these three tests providing a uniform response. The voltages in the q-axis v_{gq} plotted in Fig. 6.12c have been offseted to facilitate their comparison, the offset voltage v_{off} used for each case is 40 V (500 rpm), 80 V (1000 rpm) and 120 V (1500 rpm) respectively.

The electrical variables involved in the operation of the GSC are offered in Fig. 6.13 for the 1500 rpm test.

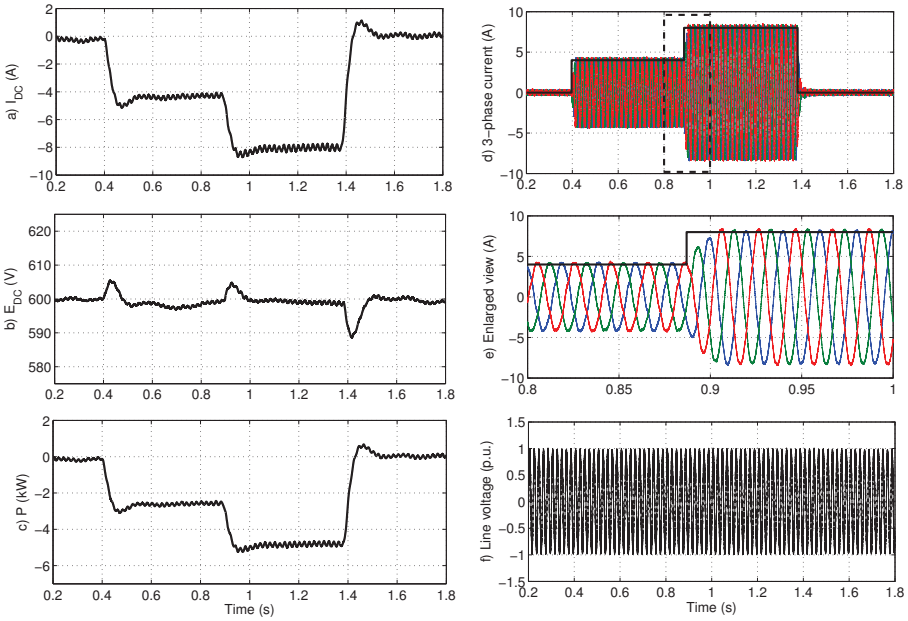

Figure 6.13: Experimental results corresponding to the constant speed scenario (1500 rpm test). Electrical variables regarding the GSC operation. a) DC current flowing through the capacitor bank, b) DC-link voltage level, c) electric power generated, d) 3-phase currents in the *abc* frame injected into the AC grid, e) enlarged view of the 3-phase currents and f) grid line voltage.

The current flowing through the DC-link is shown in Fig. 6.13a and its voltage in Fig. 6.13b. The transients observed in the DC variables corre-

spond to the sudden step changes in the operation of the generator but affected by the dynamic equation of the capacitor bank (6.12). The GSC evacuates the amount of power necessary to maintain the DC voltage constant. The electrical DC power plotted in Fig. 6.13c shows that it almost reached 5 kW operating close to its nominal value at the moment of maximum generation. The 3-phase currents injected into the AC grid are shown in Fig. 6.13d, the dashed box corresponds to the enlarged view of the second transient provided in Fig. 6.13e. As can be seen in these plots, the oversteps observed in the DC variables are not present in the AC currents. The control developed for the GSC aims to deliver the power generated as steady as possible, in this sense the setpoint sequence i^*_{gq} used for the generator (0-4-8-0 A) can be observed in the grid side in black solid line.

Speed Ramp Scenario

In this test it was intended to check the dynamic adaptation of the controller, the test was performed when the motor imposed an acceleration to the generator and, thus, its speed was constantly changing. The aim of this experiment was to check the effect of fast changing operating conditions when the setpoints are changed and transients occur. It is useful to test the controller with the higher acceleration available since this value bounds the regions where the control system operates correctly. Although is not a realistic scenario, testing the controller in these conditions permits us to verify the proper response in extreme conditions.

In Fig. 6.14a the measured generator speed is shown, the speed increased more than 150 rpm in 2 seconds during this test. This represents a strong variation in the operating conditions, wind turbines usually do not present this fast acceleration rate since they have a slow time constant. The current reference signals followed the same sequence used in the constant speed scenario as plotted in Fig. 6.12b in black solid line. Even in this scenario with a changing operating point the q-axis current i_{gq} tracked its reference signal correctly as can be observed in Fig. 6.14b. It is worth to remark also that the responses present similar characteristics to the previous scenario with constant rotational speed. The LPV controller provided an uniform response in spite of the rapid acceleration. The generator voltages plotted in Fig. 6.14c and 6.14d show the control actions resulting from the LPV controller. These voltages evolved with the operating point showing steady values and smooth transient reactions when the controller gains were constantly changing.

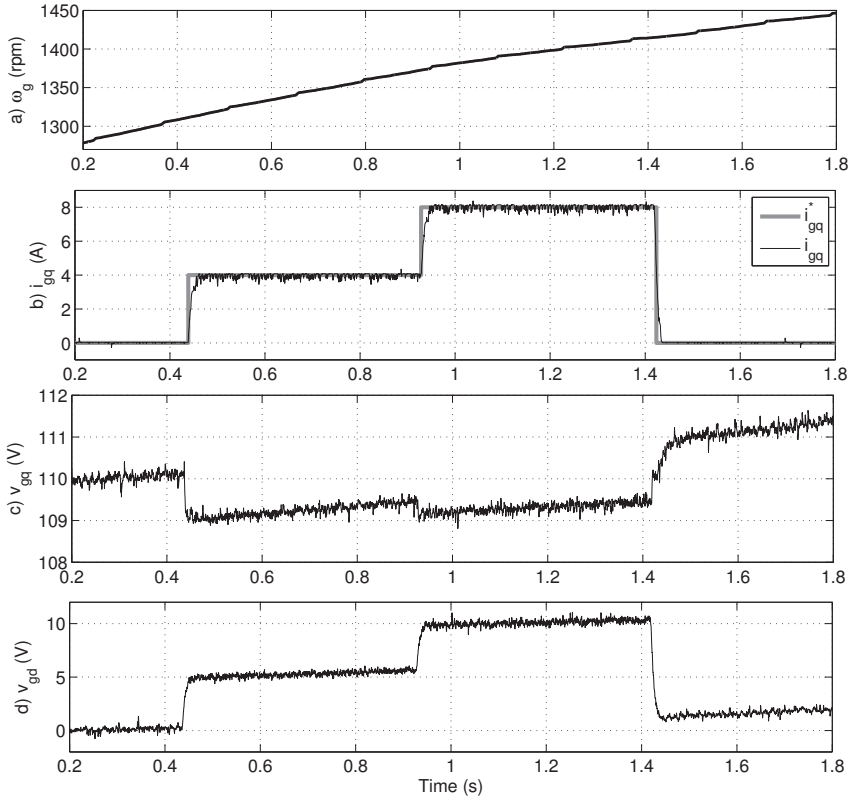

Figure 6.14: Experimental results corresponding to the speed ramp scenario. a) Generator mechanical speed corresponding to the imposed speed ramp, b) measured q-axis current and reference (LPV controller input), c) q-axis voltage (control action) and d) d-axis voltage (control action).

6.6 LPV and PI controller comparison

A comparison between the performance of a PI and LPV controllers is provided in this section. In these experiments the PI and the LPV controllers are tested in a fully-rated back-to-back converter connected to a PMSG using the test bench presented before. The PI constants have been computed using the Internal Model Control (IMC) method with the same time constant (τ) as the LPV controller, in this way the results can be easily analyzed. The IMC establishes,

$$K_p = \alpha_b \cdot L, \qquad K_i = \alpha_b \cdot R$$

where the bandwidth $\alpha_b = \frac{ln9}{\tau}$. The control structure used to implement the PI controller is shown in Fig. 6.15 where the decoupling terms are also included.

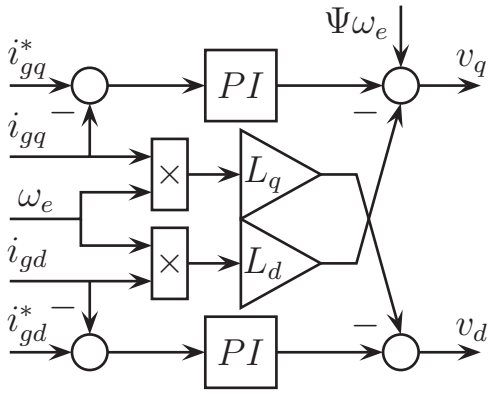

Figure 6.15: PI controller block diagram including decoupling terms

The frequency response of each control system is shown in Fig. 6.16 for the LPV and in Fig. 6.17 for the PI controller where this influence of the rotational speed can be clearly seen. The plant model corresponds to the test bench used in the experiments.

During these tests the control system follows a sequence of current set-points at three different rotational speeds. As expected, the LPV controller provides the same response in every situation while the PI controller presents a different behavior in different operating points. In order to check the differences in the transient response between LPV and the PI controller, the same test has been performed using both control systems, the results are

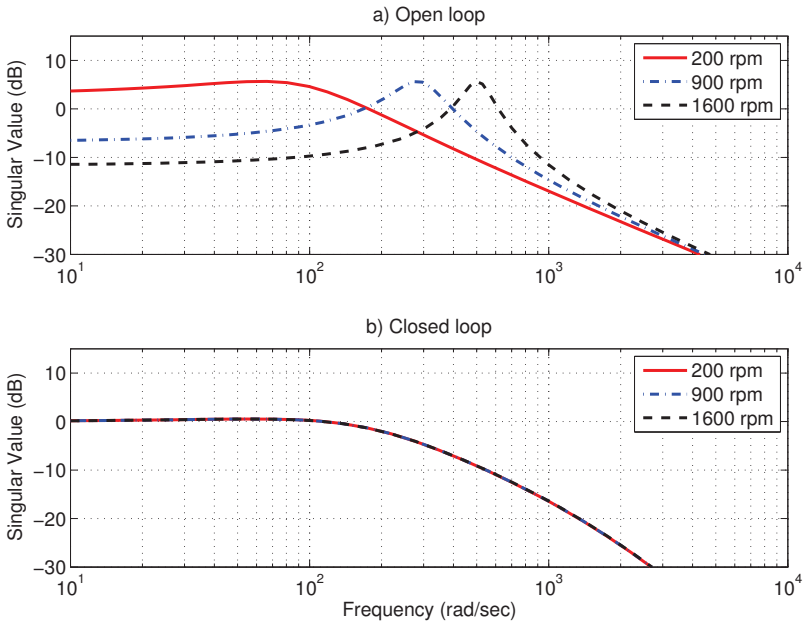

Figure 6.16: Singular values of the test bench platform model and the LPV controller

shown in Fig. 6.18. The changing transient response stated in the frequency domain analysis can be also observed during the tests. Depending on the rotational speed the PI controller presents different behaviors, however the LPV approach is not affected by the operating point and in all cases offers the same response. As can be stated in the plots referred to the PI controller, the currents have a different transition during the tests, in consequence, the generator torque will also present variations with respect to its reference signal. The voltage transitions are also highly influenced by the operating point in the case of the PI control system, the voltages show a slower or faster response to the demanded changes with dependence of the electrical frequency. None of these effects are observed when using the LPV-based control system. The PI variable response presented in Fig. 6.18 have influence in the DC-link behavior where stronger fluctuations in the DC voltage are observed when using the PI controller in contrast with the results obtained from the application of the LPV controller.

The resultant generator currents in the *abc* frame are shown in Fig. 6.19.

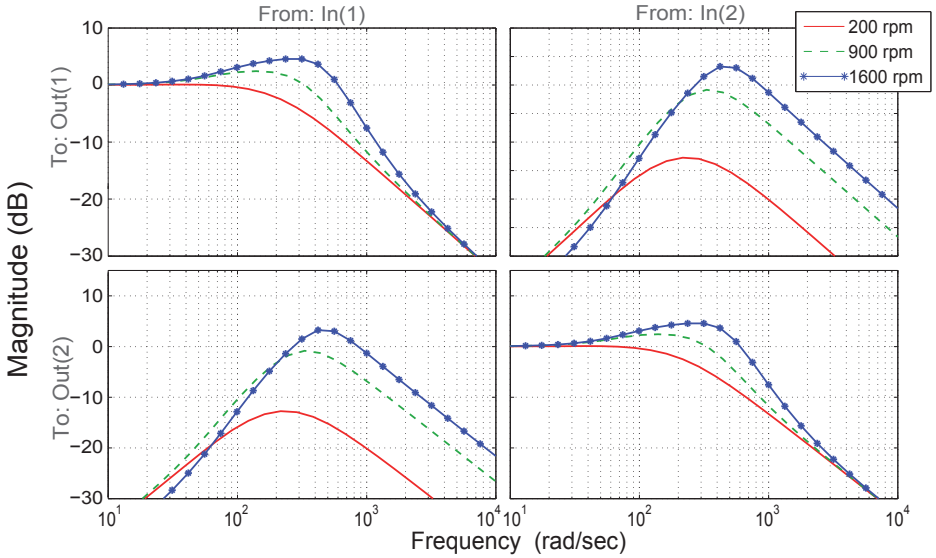

Figure 6.17: Bode diagram corresponding to the test bench platform model and the PI-based control system

The difference between using the PI-based control system and the LPV controller can be clearly seen in these plots as well.

Another interesting aspect to have in consideration is the complexity of the resulting controllers. One way to evaluate this complexity is to measure the computing time required by each controller. The switching frequency is the limitation to the amount of time available for the control system, the pulse sequence has to be updated before the next interruption starts in order to effectively follow the control signals computed. In this particular case the interruptions where at a frequency of 12 kHz (that is a period of 82 μs), coincident with the switching frequency. In the worst case execution time all the interruptions are executed sequentially and by priority. The time required by each task to be executed and the relative percentage with respect to the switching frequency are shown in Table 6.2 for the PI controller (MSC), the $\mathcal{H}_\infty$ controller (GSC) and the LPV controller (MSC). As can be stated the optimal controllers are more demanding in terms of CPU processing time with respect to the PI controller but this increment of computing time is not excessive or unaffordable for industrial processors.

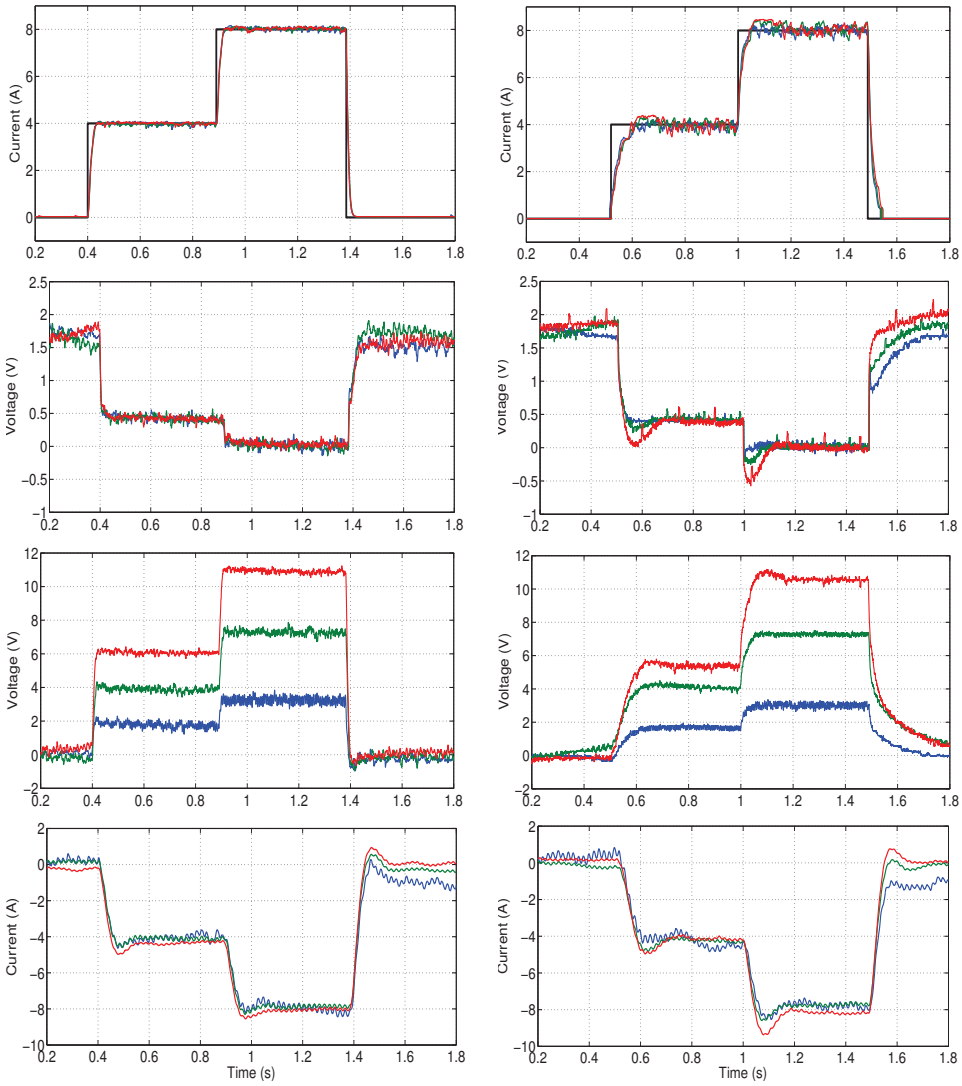

Figure 6.18: Experimental results comparison for three generator speeds: 500 rpm (blue line), 1000 rpm (green line) and 1500 rpm (red line). From top to bottom: q-axis current (the black line corresponds to the current setpoint i_q^*), q-axis voltage, d-axis voltage and DC current. Two types of controller: LPV (left column) and PI (right column)

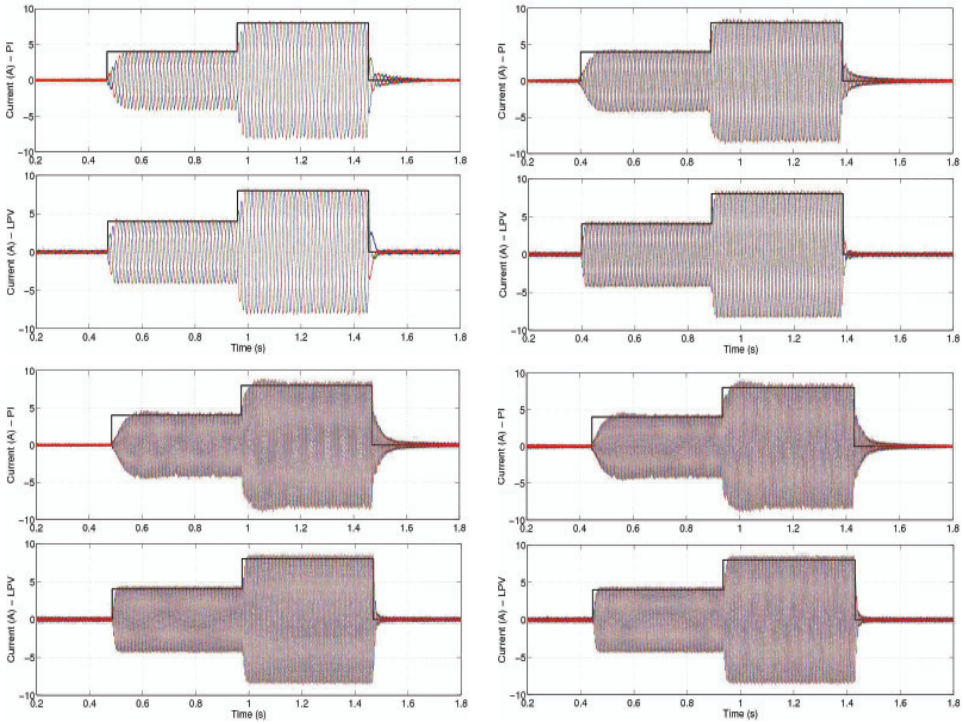

Figure 6.19: Generator current in the *abc* frame corresponding to the use of the LPV and the PI controller during the tests at 500 (top-left), 1000 (top-right), 1500 rpm (bottom-left) and during the ramp test (bottom-right). The solid black line marks the setpoints sequence.

Table 6.2: Computing time required by each task during one interruption

Task	time (μs)	Percentage
Supervisory	1	1.2 %
Sampling	12	14.6 %
SVPWM	19	23.2 %
PI controller	13.5	16.5 %
$\mathcal{H}_\infty$ controller	24	28.7 %
LPV controller	23	28 %

6.7 Conclusions

An LPV gain-scheduled control scheme for a PMSG was designed and tested experimentally. The complete proposed control system consists of an LPV gain-scheduled controller acting on the machine side of a back-to-back converter and $\mathcal{H}_\infty$ control acting on the grid side. This control scheme is capable of working properly in the wide speed range demanded by wind power applications. This approach can be used together with different high-level control strategies, which compute the torque reference signals. Unlike previous optimal control approaches, the proposed scheme produces low-order controllers simplifying the implementation in industrial computers. From implementation point of view, the controllers on both sides are similar to standard PI structures; in consequence, the implementation complexity and numerical stability are similar to classical schemes.

In particular, on the machine side, the LPV gain-scheduled control uses the rotational speed to adapt the control actions to the operating conditions as it is also done in PI schemes with decoupling terms. However, the LPV approach is able to exploit the signal coupling providing robustness and a more uniform response in different operating conditions. The experimental results show that these features allow the control system to achieve an accurate reference tracking when the operating conditions are constantly changing. Adaptability and robustness are characteristics provided by the proposed LPV controller without using complex control structures unlike other approaches, moreover, the proposed controller ensures stability in the entire range of application. The low-complexity control achieves satisfactory results in challenging conditions, such as step changes and fast accelerations, showing a smooth and uniform reaction in all the presented situations.

Appendix

The open loop system in the design setup in Fig. 6.5 can be expressed as

$$\begin{cases} \dot{x}_a = \bar{A}(\omega_g)x_a + \bar{B}_w w + \bar{B}_u u, \\ z = \bar{C}x_a + \bar{D}_u u, \end{cases} \tag{6.17}$$

where

$$\begin{aligned} x_a &= \begin{bmatrix} i_{gqd}^T & (\int (i_{gqd}^* - i_{gqd})dt)^T \end{bmatrix}, & w &= i_{gqd}^*, \\ z &= \begin{bmatrix} (W_e \int (i_{gqd}^* - i_{gqd})dt)^T & W_u u^T \end{bmatrix}, & u &= v_{lqd}, \\ \bar{A}(\omega_g) &= \begin{bmatrix} A(\omega_g) & 0 \\ -I_{2\times 2} & 0 \end{bmatrix}, & \bar{B}_w &= \begin{bmatrix} 0 \\ I_{2\times 2} \end{bmatrix}, \quad \bar{B}_u = \begin{bmatrix} B \\ 0 \end{bmatrix}, \\ \bar{C} &= \begin{bmatrix} 0 & I_{2\times 2} \\ 0 & 0 \end{bmatrix}, & \bar{D}_u &= \begin{bmatrix} 0 \\ I_{2\times 2} \end{bmatrix}, \end{aligned}$$

Then, the parameter dependant PI gains K_{sfi} and K_{sfp} that stabilises the closed loop system and guarantees (6.14) are computed by solving the following optimisation problem

$$\begin{aligned} &\text{minimise} \quad \gamma \\ &\text{subjet to} \\ &\qquad X > 0,\ \gamma > 0, \\ &\qquad \begin{bmatrix} (\bar{A}_j X + \bar{B}_u W_j) + (\bar{A}_j X + \bar{B}_u W_j)^T & \bar{B}_w & (\bar{C} + \bar{D}_u W_j)^T \\ \bar{B}_w^T & -\gamma I & 0 \\ \bar{C} + \bar{D}_u W_j & 0 & -\gamma I \end{bmatrix} < 0, \quad j = 1, 2, \\ &\qquad \Lambda \otimes X + \Upsilon \otimes (\bar{A}_j X + \bar{B}_u W_j) + \Upsilon^T \otimes (\bar{A}_j X + \bar{B}_u W_j)^T < 0, \quad j = 1, 2 \end{aligned}$$

where ">" and "<" denote positive and negative definite matrices, X is a constant matrix of dimension 4×4, Λ and Υ matrices defining the pole placement region [79], $\otimes$ the Kronecker product, $\bar{A}_1 = \bar{A}(\omega_{\min})$, $\bar{A}_2 = \bar{A}(\omega_{\max})$ and

$$K_{sf,j} = X^{-1} W_j, \quad j = 1, 2$$

This is a convex optimisation problem with linear matrix inequalities that can be solved efficiently with freely available software as Sedumi[89] and Yalmip[90].

7 Conclusions and Future Research

7.1 Conclusions

The scope of this thesis has been the application of optimal multi-variable controllers to a WECS, in addition, the validation of the system model has been performed following the official regulations and also a small-scale setup has been constructed in order to test the proposed control systems and evaluate its viability.

The access to data obtained from actual wind turbines during the field tests was a great opportunity to investigate the behavior of a model in the same conditions and compare the outcome. This situation is not usual and it provided detailed information about internal variables of the electrical system. Although the access to the control system was restricted a good approximation was developed showing a similar response in simulation. The validation process was focused on the grid fault situation, where strong transients are present and the behavior of the WECS is less predictable, nevertheless the simulation achieved a good matching level in all the tests. The model developed passed the validation process described in two grid codes, and, therefore it could be considered a valid model, at least according to the regulations taken into account. Later, using the a test bench to run experiments, the correctness of the available model was verified.

The development of the experimental test bench was challenging, many different issues had to be solved by using the available lab equipment. A start-up process had to be done since some of the equipment was new and

required several tests and calibrations in order to reach the desired performance. The aim of the test bench was to reproduce a realistic situation for a WECS and also provide enough flexibility to implement and modify the control strategies.

The modeling of the test bench was conducted following the approach developed during the validation process achieving a good approximation with high detail, as was confirmed during the experiments using the GSC. As a first step, before the generator was used, the control system for a VSC connected to the grid was developed. The work done with the GSC aimed to implement and test an optimal controller that ensures stability and provides certain degree of robustness since, in its design stage, it is considered the worst case of the disturbance signals. There is the impression that these type of controllers are not practical since, in general, they are complex and computationally expensive. In order to avoid this situation, the minimal expression of the controller was developed maintaining the benefits of its application. Moreover the design was proposed in a systematic procedure that provided a straightforward way to generate the controller while gives flexibility in choosing the desired performance.

A Linear Parameter-varying approach was used to control the generator through the MSC. The LPV controller was compared to a benchmark that is the generally used, i.e. the PI controller. The well-known way of computing the PI gains (IMC) was selected and the use of decoupling terms was also implemented to enhance its performance. The results show an improvement of the LPV controller performance with respect to the PI, the LPV approach presents an uniform response in all the tests an, moreover, the controller ensures stability in the entire range of application. The complexity of the LPV controller with respect to the PI is minimally increased and its design process was developed systematic and flexible. The proposed control system was tested in realistic simulations that include the mechanical behavior of the WECS, it was also evaluated in a test bench in an attempt to resemble a real situation. The strong transient used during the tests were useful to highlight the differences between both performances. Moreover, beyond the theoretical benefits observed in simulations using simplified and linear models, a physical implementation and test of both control systems was provided. In the laboratory, the non-linearities inherent to the equipment were put into test by using a discrete implementation of the control system in a DSP, these experiments confirmed the predicted results.

Previous studies [57, 58, 61, 62] reported that the use of $\mathcal{H}_\infty$ and LPV techniques yield complicated high-order controllers which are not oriented to be implemented in industrial equipment. It has been verified that it

is not required a complex controller to achieve some improvement in the system behavior. In addition, the results look promising and applicable to other technologies that use combinations of generators and converters. It is also worth to highlight that the uniform response that shows the LPV controller which may be useful to predict the response during transients, and can be also helpful to design alternative control strategies. Traditional control schemes can yield different responses during transients affecting the performance of the WECS, and may lead to undesirable responses. This can be an issue if the wind energy penetration is high in the power system.

7.2 Future Research

From this thesis, future research lines have arisen, which appear listed in the following:

- From the grid-side converter point of view it would be interesting to test the benefits of the proposed control system in combination of Line-Fault Ride-Through techniques. Equipment acting as a grid emulator and generating the disturbed conditions of the grid can be implemented in the laboratory to test this situation. In the same line, the analysis of frequency support schemes by modifying the torque stepoints can be tested, in this way it can be evaluated the potential benefit of having a more accurate control system in a situation when the torque has to be suddenly changed.

- In order to increase the reliability of the LPV controller a sensorless scheme can be developed and the stability of the LPV approach using this strategy can be tested using the available equipment.

- The application of the proposed control system to wave energy devices is an interesting topic to be explored. Some wave energy units present a strong pulsating nature and develop high torques in short periods of time. In this consideration, the use of controllers that adapt to the constantly changing situation while offer a predictable response may help to the development and implantation of these energy resources.

Bibliography

[1] Asociación Empresarial Eólica. Validación y certificación de los requisitos del PO 12.3 sobre la respuesta de las instalaciones eólicas ante huecos de tensión. Versión 6. *Procedimientos de verificación (in spanish)*, Julio 2009. XI, XIV, 2, 32, 39

[2] www.alstom.com. *Website*, December 2010. XIV, 32, 33

[3] Technical Guidelines for Power Generating Units TR4. Demands on Modelling and Validating Simulation models of the electrical Characteristics of Power Generating Units and Systems. April 2009. XIV, 2, 39, 40, 41

[4] Yazhou Lei, A. Mullane, G. Lightbody, and R. Yacamini. Modeling of the wind turbine with a doubly fed induction generator for grid integration studies. *IEEE Transactions on Energy Conversion*, 21(1):257–264, March 2006. 1

[5] T. Petru and T. Thiringer. Modeling of wind turbines for power system studies. *IEEE Transactions on Power Systems*, 17(4):1132– 1139, 2002. 1

[6] M. Kayikci and J.V. Milanovic. Assessing Transient Response of DFIG-Based Wind Plants - The Influence of Model Simplifications and Parameters. *Power Systems, IEEE Transactions on*, 23(2):545 –554, May 2008. 1

[7] Lingling Fan, R. Kavasseri, Zhixin Lee Miao, and Chanxia Zhu. Modeling of DFIG-Based Wind Farms for SSR Analysis. *Power Delivery, IEEE Transactions on*, 25(4):2073 –2082, Oct. 2010. 1

[8] He Yikang, Hu Jiabing, and Zhao Rende. Modeling and control of wind-turbine used DFIG under network fault conditions. In *Electrical Machines and Systems, 2005. ICEMS 2005. Proceedings of the Eighth International Conference on*, volume 2, pages 986 –991 Vol. 2, Sept. 2005. 1

[9] A. Petersson, T. Thiringer, L. Harnefors, and T. Petru. Modeling and experimental verification of grid interaction of a DFIG wind turbine. *Energy Conversion, IEEE Transactions on*, 20(4):878 – 886, Dec. 2005. 1

[10] S. Auddy, R.K. Varma, and M. Dang. Field Validation of a Doubly Fed Induction Generator (DFIG) Model. In *Electrical Power Conference, 2007. EPC 2007. IEEE Canada*, pages 484 –489, Oct. 2007. 1

[11] H. Li and Z. Chen. Overview of different wind generator systems and their comparisons. *Renewable Power Generation, IET*, 2(2):123 –138, June 2008. 1

[12] S.Z. Vijlee, A. Ouroua, L.N. Domaschk, and J.H. Beno. Directly-Coupled Gas Turbine Permanent Magnet Generator Sets for Prime Power Generation On Board Electric Ships. In *Electric Ship Technologies Symposium. (ESTS '07). IEEE*, pages 340 –347, May 2007. 1

[13] A. Binder and T. Schneider. Permanent magnet synchronous generators for regenerative energy conversion - a survey. In *European Conference on Power Electronics and Applications*, page 10 pp., 2005. 1

[14] M.A. Rahman, A.M. Osheiba, T.S. Radwan, and E.S. Abdin. Modelling and controller design of an isolated diesel engine permanent magnet synchronous generator. *IEEE Transactions on Energy Conversion*, 11(2):324 –330, June 1996. 1

[15] F. Diaz-Gonzalez, A. Sumper, O. Gomis-Bellmunt, and R. Villafafila-Robles. Modeling and Validation of a Flywheel Energy Storage Lab-Setup. In *IEEE PES Innovative Smart Grid Technologies (ISGT) Europe Conference*, Oct. 2012. 1

[16] A.S. Nagorny, N.V. Dravid, R.H. Jansen, and B.H. Kenny. Design aspects of a high speed permanent magnet synchronous motor / generator for flywheel applications. In *IEEE International Conference on Electric Machines and Drives*, pages 635 –641, May 2005. 1

[17] I. Schiemenz and M. Stiebler. Control of a permanent magnet synchronous generator used in a variable speed wind energy system. In *Electric Machines and Drives Conference (IEMDC 2001). IEEE International*, pages 872 –877, 2001. 1

[18] Global Wind Energy Council. Global Wind Energy Outlook 2012. In *GWEC*, Nov. 2012. 2

[19] H. Polinder, D. Bang, H. Li, and Z. Chen. Concept Report on Generator Topologies, Mechanical & Electromagnetic Optimization. Deliverable D1B2.b.1. *Project UpWind*, Dec. 2007. 2

[20] Ministerio de Industria Turismo y Comercio. PO 12.3 Requisitos de respuesta frente a huecos de tensión de las instalaciones eólicas. *Procedimientos de operación (in spanish)*, Octubre 2006. 2, 39

[21] FGW: Technische Richtlinien für Erzeugungseinheiten TR3. Bestimmung der Elektrischen Eigenschaften von Erzeugungseinheiten am Mittel-, Hoch- und Höchstspannungsnetz. January 2009. 2, 39, 40

[22] B. Singh, B.N. Singh, A. Chandra, K. Al-Haddad, A. Pandey, and D.P. Kothari. A review of three-phase improved power quality AC-DC converters. *IEEE Transactions on Industrial Electronics*, 51(3):641 – 660, June 2004. 2

[23] J.M. Carrasco, L.G. Franquelo, J.T. Bialasiewicz, E. Galvan, R.C.P. Guisado, Ma.A.M. Prats, J.I. Leon, and N. Moreno-Alfonso. Power-Electronic Systems for the Grid Integration of Renewable Energy Sources: A Survey. *IEEE Transactions on Industrial Electronics*, 53(4):1002 –1016, June 2006. 2

[24] José Luis Domínguez-García, Oriol Gomis-Bellmunt, Lluís Trilla-Romero, and Adrià Junyent-Ferré. Indirect vector control of a squirrel cage induction generator wind turbine. *Computers & Mathematics with Applications*, 64(2):102 – 114, 2012. 2

[25] M. Liserre, T. Sauter, and J.Y. Hung. Future Energy Systems: Integrating Renewable Energy Sources into the Smart Power Grid Through

Industrial Electronics. *IEEE Industrial Electronics Magazine*, 4(1):18 –37, March 2010. 2

[26] B.K. Bose. Power Electronics and Motor Drives Recent Progress and Perspective. *IEEE Transactions on Industrial Electronics*, 56(2):581 –588, Feb. 2009. 2

[27] F. Blaabjerg, R. Teodorescu, M. Liserre, and A.V. Timbus. Overview of Control and Grid Synchronization for Distributed Power Generation Systems. *IEEE Transactions on Industrial Electronics*, 53(5):1398 – 1409, Oct. 2006. 2

[28] José Luis Domínguez-García, Oriol Gomis-Bellmunt, Fernando D. Bianchi, and Andreas Sumper. Power oscillation damping supported by wind power: A review. *Renewable and Sustainable Energy Reviews*, 16(7):4994 – 5006, 2012. 2

[29] A. Ruiz-Àlvarez, A. Colet-Subirachs, F. Àlvarez-Cuevas Figuerola, O. Gomis-Bellmunt, and A. Sudrià-Andreu. Operation of a Utility Connected Microgrid Using an IEC 61850-Based Multi-Level Management System. *IEEE Transactions on Smart Grid*, 3(2):858 –865, June 2012. 2

[30] L. Trilla, O. Gomis-Bellmunt, A. Sudrià-Andreu, Jun Liang, and Tianjun Jing. Control of SCIG wind farm using a single VSC. In *Proceedings of the 2011-14th European Conference on Power Electronics and Applications (EPE 2011)*, pages 1 –9, Sept 2011. 2

[31] R.P.S. Chandrasena, A. Arulampalam, J.B. Ekanayake, and S.G. Abeyratne. Grid side converter controller of DFIG for wind power generation. In *International Conference on Industrial and Information Systems, 2007. ICIIS 2007.*, pages 141 –146, Aug. 2007. 2

[32] M.P. Kazmierkowski and L. Malesani. Current control techniques for three-phase voltage-source PWM converters: a survey. *IEEE Transactions on Industrial Electronics*, 45(5):691 –703, Oct 1998. 3

[33] W. Leonhard. *Control of electrical drives*. Springer Verlag, 1996, ISBN-9783540593805. 3

[34] Dong-Choon Lee, Seung-Ki Sul, and Min-Ho Park. Comparison of AC current regulators for IGBT inverter. In *Conference Record of the Power Conversion Conference, 1993.*, pages 206 –212, April 1993. 3

[35] D.G. Holmes and D.A. Martin. Implementation of a direct digital predictive current controller for single and three phase voltage source inverters. In *Conference Record of the 1996 IEEE Industry Applications Conference. Thirty-First IAS Annual Meeting.*, volume 2, pages 906 –913 vol.2, Oct 1996. 3

[36] R. Turner, S. Walton, and R. Duke. Robust High-Performance Inverter Control Using Discrete Direct-Design Pole Placement. *IEEE Transactions on Industrial Electronics*, 58(1):348 –357, Jan. 2011. 3

[37] C. Olalla, R. Leyva, A. El Aroudi, P. Garces, and I. Queinnec. LMI robust control design for boost PWM converters. *IET Power Electronics*, 3(1):75 –85, Jan. 2010. 3

[38] J.C. Basilio, J.A. Silva, L.G.B. Rolim, and M.V. Moreira. H∞ design of rotor flux-oriented current-controlled induction motor drives: speed control, noise attenuation and stability robustness. *Control Theory Applications, IET*, 4(11):2491 –2505, Nov. 2010. 3

[39] A. Barakat, S. Tnani, G. Champenois, and E. Mouni. Output voltage control of synchronous generator using diode and thyristor excitation structures combined with multivariable H∞ controllers. *IET Electric Power Applications*, 6(4):203 –213, April 2012. 3

[40] M. Njeh, S. Cauet, P. Coirault, and P. Martin. H∞ control strategy of motor torque ripple in hybrid electric vehicles: an experimental study. *Control Theory Applications, IET*, 5(1):131 –144, June 2011. 3

[41] S. Arulselvi, G. Uma, and M. Chidambaram. Design of PID controller for boost converter with RHS zero. In *Power Electronics and Motion Control Conference, 2004. IPEMC 2004. The 4th International*, volume 2, pages 532 –537 Vol.2, Aug. 2004. 3, 45

[42] H.F. Wang. Interactions and multivariable design of STATCOM AC and DC voltage control. *Electrical Power and Energy Systems*, 25:387 –394, May 2003. 3

[43] N. Nayak, S. K. Routray, and P. K. Rout. State feedback robust H∞ controller for transient stability enhancement of VSC-HVDC transimission systems. *Procedia Technology*, 4:652 –660, May 2012. 3

[44] M. Chinchilla, S. Arnaltes, and J.C. Burgos. Control of Permanent-Magnet Generators Applied to Variable-Speed Wind-Energy Systems

Connected to the Grid. *IEEE Transactions on Energy Conversion*, 21:130–135, 2006. 3

[45] A. D. Hansen and G. Michalke. Modelling and Control of Variable speed Multi-pole Permanent Magnet Synchronous Generator Wind Turbine. *Wind Energy*, 11(5):537 – 554, 2008. 3

[46] S.M. Muyeen, R. Takahashi, T. Murata, and J. Tamura. A variable speed wind turbine control strategy to meet wind farm grid code requirements. *IEEE Transactions on Power Systems*, 25(1):331–340, 2010. 3

[47] V. Akhmatov. Modeling and Ride-through Capability of Variable Speed Wind Turbines with Permanent Magnet Generators. *Wind Energy*, 9:313–326, 2006. 3

[48] J.F. Conroy and R. Watson. Low-voltage ride-through of a full converter wind turbine with permanent magnet generator. *IET Renewable Power Generation*, 1(3):182 –189, Sept. 2007. 3

[49] Panayiotis Moutis, Stavros A. Papathanassiou, and Nikos D. Hatziargyriou. Improved load-frequency control contribution of variable speed variable pitch wind generators. *Renewable Energy*, 48(0):514 – 523, 2012. 3

[50] M.G. Molina, A.G. Sanchez, and A.M.R. Lede. Dynamic modeling of wind farms with variable-speed direct-driven PMSG wind turbines. In *Transmission and Distribution Conference and Exposition: Latin America, (IEEE/PES)*, pages 816 – 823, Nov. 2010. 3, 4, 67

[51] A.M. Howlader, N. Urasaki, S. Chakraborty, A. Yona, T. Senjyu, and A.Y. Saber. Fuzzy controller based output power leveling enhancement for a permanent magnet synchronous generator. In *2011 IEEE International Conference on Fuzzy Systems (FUZZ)*, pages 656 –661, June 2011. 3, 4, 67

[52] P. Apkarian, P. Gahinet, and G.S. Becker. Self-scheduled H∞ control of linear parameter-varying systems: a design example. *Automatica*, 31(9):1251 – 1261, 1995. 4, 69, 73, 74

[53] Gregory Scott Becker and A. Packard. Robust performance of linear parametrically varying systems using parametrically-dependent linear feedback. *Systems & Control Letters*, 23(3):205–215, 1994. 4

[54] Chen Wang and G. Weiss. Self-Scheduled LPV Control of a Wind Driven Doubly-Fed Induction Generator. In *45th IEEE Conference on Decision and Control*, pages 1246 –1251, Dec. 2006. 4

[55] H.N. Tien, C.W. Scherer, and J.M.A. Scherpen. Robust performance of self-scheduled LPV control of doubly-fed induction generator in wind energy conversion systems. In *European Conference on Power Electronics and Applications*, pages 1 –10, Sept. 2007. 4

[56] E.B. Muhando, T. Senjyu, A. Uehara, and T. Funabashi. Gain-Scheduled H∞ Control for WECS via LMI Techniques and Parametrically Dependent Feedback Part II: Controller Design and Implementation. *Industrial Electronics, IEEE Transactions on*, 58(1):57 –65, Jan. 2011. 4

[57] J.D. Bendtsen and K. Trangbaek. Discrete-time LPV current control of an induction motor. In *42nd IEEE Conference on Decision and Control*, volume 6, pages 5903–5908, 2003. 4, 96

[58] D. Khamari, A. Makouf, and S. Drid. Control of induction motor using polytopic LPV models. In *International Conference on Communications, Computing and Control Applications (CCCA)*, pages 1–5, 2011. 4, 96

[59] F. Blanchini, D. Casagrande, S. Miani, and U. Viaro. An LPV control scheme for induction motors. In *IEEE 51st Annual Conference on Decision and Control (CDC)*, pages 7602–7607, 2012. 4

[60] S. Machmoum, P. Chervel, C. Darengosse, and M. Machmoum. A linear parameter variant H∞ controller design for a permanent magnet synchronous machine. In *European Conference on Power Electronics and Applications*, page 11 pp, 2005. 4

[61] L. Pohl and P. Blaha. Linear parameter varying approach to robust control of a permanent magnet synchronous motor. In *15th IEEE International Conference on Intelligent Engineering Systems (INES)*, pages 287 –291, June 2011. 4, 96

[62] Y. Altun and K. Gulez. Linear parameter varying control of permanent magnet synchronous motor via parameter-dependent lyapunov function for electrical vehicles. In *IEEE International Conference on Vehicular Electronics and Safety (ICVES)*, pages 340–345, 2012. 4, 96

[63] S. Heier. *Grid Integration of Wind Energy Conversion Systems*. John Wiley and Sons, 1998. 8, 26

[64] Undeland T.M. Robbins W.P. Mohan, N. *Power Electronics: Converters, Applications, and Design*. John Wiley and Sons, 2003. 12, 15

[65] Adrià Junyent-Ferré, Andreas Sumper, Oriol Gomis-Bellmunt, Marc Sala, and Montserrat Mata. Digital simulation of voltage dip characteristics of wind turbine systems. In *9th International Conference on Electrical Power Quality and Utilization*, 2007. 12, 30

[66] Cinergia. www.cinergia.coop. *Website*, december 2010. 19

[67] Z.Lubosny. *Wind Turbine Operation in Electric Power Systems*. Springer, 2003. 25

[68] E. Valsera-Naranjo, A. Sumper, O. Gomis-Bellmunt, A. Junyent-Ferré, and M. Martínez-Rojas. Pitch control system design to improve frequency response capability of fixed-speed wind turbine systems. *European Transactions on Electrical Power*, Dec. 2010. 26

[69] Adrià Junyent-Ferré. Modelització i control d'un sistema de generació elèctrica de turbina de vent (in catalan). Master's thesis, ETSEIB-UPC, 2007. 26, 30

[70] Adrià Junyent-Ferré, Oriol Gomis-Bellmunt, Andreas Sumper, Marc Sala, and Montserrat Mata. Modeling and control of the doubly fed induction generator wind turbine. *Simulation Modelling Practice and Theory*, 18(9):1365–1381, October 2010. 26, 30, 49

[71] R.H. Park. Two reaction theory of synchronous machines. *AIEE Transactions*, 48:716–730, 1929. 27, 48

[72] Paul C. Krause. *Analysis of Electric Machinery*. McGraw-Hill, 1986. 27

[73] Jamal A. Baroudi, Venkata Dinavahi, and Andrew M. Knight. A review of power converter topologies for wind generators. *Renewable Energy*, In Press, Corrected Proof, 2007. 28

[74] L. Trilla, O. Gomis-Bellmunt, A. Junyent-Ferre, M. Mata, J. Sanchez Navarro, and A. Sudria-Andreu. Modeling and Validation of DFIG 3-MW Wind Turbine Using Field Test Data of Balanced and Unbalanced Voltage Sags. *IEEE Transactions on Sustainable Energy*, 2(4):509–519, 2011. 30, 31

[75] Jens Fortmann, Stephan Engelhardt, Jörg Kretschmann, Christian Feltes, and Prof. I. Erlich. Validation of an RMS DFIG Simulation Model According to New German Model Validation Standard FGW TR4 at Balanced and Unbalanced Grid Faults. *Transmission Networks for Offshore Wind Farms*, October 2009. 40

[76] E.J. Bueno, A. Hernandez, F.J. Rodriguez, C. Giron, R. Mateos, and S. Cobreces. A DSP- and FPGA-Based Industrial Control With High-Speed Communication Interfaces for Grid Converters Applied to Distributed Power Generation Systems. *IEEE Transactions on Industrial Electronics*, 56(3):654 –669, March 2009. 45

[77] K. Zhou and J.C. Doyle. *Essentials of Robust Control*. Prentice Hall, 1998, ISBN-9780135258330. 48, 52

[78] F.D. Bianchi, A. Egea-Àlvarez, A. Junyent-Ferré, and O. Gomis-Bellmunt. Optimal control of voltage source converters under power system faults. *Control Engineering Practice*, 20(5):539 – 546, 2012. 51, 72, 76

[79] M. Chilali and P. Gahinet. H∞ design with pole placement constraints: an LMI approach. *IEEE Transactions on Automatic Control*, 41(3):358 –367, March 1996. 51, 75, 94

[80] B. Arbetter and D. Maksimovic. Feedforward pulse width modulators for switching power converters. *IEEE Transactions on Power Electronics*, 12(2):361 –368, March 1997. 51, 76

[81] P. Weston and I. Postlethwaite. Linear conditioning for systems containing saturating actuators. *Automatica*, 36(9):1347–1354, 2000. 53

[82] M. Karimi-Ghartemani and M.R. Iravani. A method for synchronization of power electronic converters in polluted and variable-frequency environments. *IEEE Transactions on Power Systems*, 19:1263– 1270, 2004. 56, 82

[83] D. Goodfellow and G. Smith. Control strategy for variable speed of a fixed-pitch wind turbine operating in a wide speed range. *Proceedings of 8th BWEA Conference, Cambridge*, pages 219–228, 1986. 70

[84] R. De Doncker, D. W. J. Pulle, and A. Veltman. *Power Systems: Advanced Electrical Drives: Analysis, Modeling, Control*. Springer, 2011, ISBN-9400701810. 71, 72

[85] L. Trilla, F.D. Bianchi, and O. Gomis-Bellmunt. Optimal Control of VSC for STATCOM Applications. In *Power Plant & Power System Control Symposium (PPPSC)*, Sept. 2012. 72, 76

[86] F.D. Bianchi, H. De Battista, and R.J. Mantz. *Wind Turbine Control Systems*. Springer-Verlag, 2007. 72

[87] J. Jonkman, S. Butterfield, W. Musial, and G. Scott. Definition of a 5-MW Reference Wind Turbine for Offshore System Development. *National Renewable Energy Laboratory. Technical Report*, Feb. 2009. 76

[88] H. Li, Z. Chen, and H. Polinder. Research report on numerical evaluation of various variable speed wind generator systems. Deliverable D1B2.b.3. *Project UpWind*, 2002-2006. 76, 82

[89] J. Sturm. Using SeDuMi 1.02, a Matlab toolbox for optimization over symmetric cones. *Optim. Method Softw.*, 11-12:625–653, 1999. 94

[90] J. Lfberg. Yalmip : A toolbox for modeling and optimization in MATLAB. In *Proceedings of the CACSD Conference*, Taipei, Taiwan, 2004. 94

A

List of Publications

In this chapter, the list of publications both journals and conferences papers, derived from the development of the thesis are presented.

A.1 Journal articles

[**J1**] L. Trilla, O. Gomis-Bellmunt, A. Junyent-Ferré, M. Mata, J. Sànchez-Navarro, A. Sudrià-Andreu. "Modeling and Validation of DFIG 3-MW Wind Turbine Using Field Test Data of Balanced and Unbalanced Voltage Sags". IEEE Transactions on Sustainable Energy, vol.2, no.4, pp.509-519, Oct. 2011. doi: 10.1109/TSTE.2011.2155685

[**J2**] L. Trilla, F. D. Bianchi, O. Gomis-Bellmunt. "Optimal control of a grid-connected converter: design and implementation". Renewable Energy Journal, January 2013 (under review)

[**J3**] L. Trilla, F. D. Bianchi, O. Gomis-Bellmunt. "Linear Parameter-Varying Control of Permanent Magnet Synchronous Generators for Wind Power Systems". IET Power Electronics, March 2013 (under second review)

A.2 Conference articles

[**C1**] L. Trilla, O. Gomis-Bellmunt, A. Junyent-Ferré, M. Mata, J. Sànchez-Navarro, A. Sudrià-Andreu. "DFIG-based WTGS modeling and val-

idation using field test data". In proceedings of the European Wind Energy Conference, EWEC 2011

[**C2**] L. Trilla, F. D. Bianchi, O. Gomis-Bellmunt. "Optimal Control of VSC for STATCOM Applications". Proceedings of the 8th Power Plant and Power System Control Symposium (PPPSC 2012), vol.8, no.1, pp.588-593, doi: 10.3182/20120902-4-FR-2032.00103

A.3 Other publications

Within this section other relevant publications not directly related to the thesis are introduced.

[**O1**] L. Trilla, O. Gomis-Bellmunt, A. Junyent-Ferré, A.E. Álvarez, A. Sudrià-Andreu. "Control of a squirrel cage induction generator wind farm connected to a single power converter". 45th International Universities Power Engineering Conference (UPEC), pp.1,6, Aug. 31-Sept. 3 2010. ISBN 978-1-4244-7667-1

[**O2**] L. Trilla, O. Gomis-Bellmunt, A. Junyent-Ferré, A. Sudrià-Andreu. "Analysis of total power extracted with common converter wind farm topology". XIX International Conference on Electrical Machines (ICEM), pp.1,6, 6-8 Sept. 2010. doi: 10.1109/ICELMACH.2010.5608072

[**O3**] L. Trilla, T. Thiringer. "Wave farm collection grid analysis and design". Techinal Report 2013:4 Chalmers public library website